INFORMATION TO USERS

This manuscript has been reproduced from the microfilm master. UMI films the text directly from the original or copy submitted. Thus, some thesis and dissertation copies are in typewriter face, while others may be from any type of computer printer.

The quality of this reproduction is dependent upon the quality of the copy submitted. Broken or indistinct print, colored or poor quality illustrations and photographs, print bleedthrough, substandard margins, and improper alignment can adversely affect reproduction.

In the unlikely event that the author did not send UMI a complete manuscript and there are missing pages, these will be noted. Also, if unauthorized copyright material had to be removed, a note will indicate the deletion.

Oversize materials (e.g., maps, drawings, charts) are reproduced by sectioning the original, beginning at the upper left-hand corner and continuing from left to right in equal sections with small overlaps. Each original is also photographed in one exposure and is included in reduced form at the back of the book.

Photographs included in the original manuscript have been reproduced xerographically in this copy. Higher quality 6" x 9" black and white photographic prints are available for any photographs or illustrations appearing in this copy for an additional charge. Contact UMI directly to order.

UMI

A Bell & Howell Information Company
300 North Zeeb Road, Ann Arbor MI 48106-1346 USA
313/761-4700 800/521-0600

LITHIUM INSERTION IN HARD CARBON ANODE MATERIALS FOR LI-ION BATTERIES

By

Edward Buiel

SUBMITTED IN PARTIAL FULFILLMENT OF THE
REQUIREMENTS FOR THE DEGREE OF
DOCTOR OF PHILOSOPHY
AT
DALHOUSIE UNIVERSITY
HALIFAX, NOVA SCOTIA
OCTOBER, 1998

© Copyright by Edward Buiel, 1998

National Library of Canada
Acquisitions and Bibliographic Services
395 Wellington Street
Ottawa ON K1A 0N4
Canada

Bibliothèque nationale du Canada
Acquisitions et services bibliographiques
395, rue Wellington
Ottawa ON K1A 0N4
Canada

Your file Votre référence

Our file Notre référence

The author has granted a non-exclusive licence allowing the National Library of Canada to reproduce, loan, distribute or sell copies of this thesis in microform, paper or electronic formats.

The author retains ownership of the copyright in this thesis. Neither the thesis nor substantial extracts from it may be printed or otherwise reproduced without the author's permission.

L'auteur a accordé une licence non exclusive permettant à la Bibliothèque nationale du Canada de reproduire, prêter, distribuer ou vendre des copies de cette thèse sous la forme de microfiche/film, de reproduction sur papier ou sur format électronique.

L'auteur conserve la propriété du droit d'auteur qui protège cette thèse. Ni la thèse ni des extraits substantiels de celle-ci ne doivent être imprimés ou autrement reproduits sans son autorisation.

0-612-36573-5

Canada

DALHOUSIE UNIVERSITY
DEPARTMENT OF
PHYSICS

The undersigned hereby certify that they have read and recommend to the Faculty of Graduate Studies for acceptance a thesis entitled **"Lithium Insertion in Hard Carbon Anode Materials for Li-ion Batteries"** by **Edward Buiel** in partial fulfillment of the requirements for the degree of **Doctor of Philosophy**.

Dated: October, 1998

External Examiner: _____
Dr. J.E. Fischer

Research Supervisor: _____
Dr. Jeff R. Dahn

Examing Committee: _____
Dr. Manfred H. Jericho

_____
Dr. Hans Jürgen Kreuzer

DALHOUSIE UNIVERSITY

FACULTY OF GRADUATE STUDIES

The undersigned hereby certify that they have read and recommend to the Faculty of Graduate Studies for acceptance a thesis entitled "Lithium Insertion in Hard Carbon Anode Materials For Li-ion Batteries"

by Edward Raymond Buiel

in partial fulfillment of the requirements for the degree of Doctor of Philosophy.

Dated: April 24, 1998

External Examiner

Research Supervisor

Examining Committee

DALHOUSIE UNIVERSITY

Date: **October, 1998**

Author: **Edward Buiel**

Title: **Lithium Insertion in Hard Carbon Anode Materials for Li-ion Batteries**

Department: **Physics**

Degree: **Ph.D.** Convocation: **October** Year: **1998**

Permission is herewith granted to Dalhousie University to circulate and to have copied for non-commercial purposes, at its discretion, the above title upon the request of individuals or institutions.

Signature of Author

THE AUTHOR RESERVES OTHER PUBLICATION RIGHTS, AND NEITHER THE THESIS NOR EXTENSIVE EXTRACTS FROM IT MAY BE PRINTED OR OTHERWISE REPRODUCED WITHOUT THE AUTHOR'S WRITTEN PERMISSION.

THE AUTHOR ATTESTS THAT PERMISSION HAS BEEN OBTAINED FOR THE USE OF ANY COPYRIGHTED MATERIAL APPEARING IN THIS THESIS (OTHER THAN BRIEF EXCERPTS REQUIRING ONLY PROPER ACKNOWLEDGEMENT IN SCHOLARLY WRITING) AND THAT ALL SUCH USE IS CLEARLY ACKNOWLEDGED.

Contents

List of Tables

List of Figures

Acknowledgements

My supervisor, Dr. Jeff Dahn, is thanked for his guidance, patience and brilliant editing that is reflected throughout this thesis. I am grateful to Andy George whose expertise and know-how greatly simplified the preparation of many of the high temperature samples presented in this thesis.

I would also like to that all my colleagues and professeurs at both Simon Fraser University and Dalhousie University that have helped me over the years. Without their constant encouragement and advice my thesis would have surely taken much longer and would have been much tougher to complete.

Abstract

In this thesis, lithium insertion in hard carbon prepared from sucrose is studied. Sucrose is particularly promising from a commercial stand point because it has a large reversible capacity (600mAh/g) and is very cheap. However, these materials suffer from two problems: large irreversible capacity and hysteresis in the voltage profile, which are the focus of this thesis.

Reducing the hysteresis in the voltage profile requires reducing the hydrogen content which can be achieved by heating hard carbon to higher temperatures. However, above a critical temperature, a loss in the reversible capacity occurs. In this thesis, this loss in capacity is correlated to micropore closure or what we call the formation of "embedded fullerenes." This correlation required a prototype CO_2 gas adsorption analyser to be built and the design of this system is explained. Furthermore, a model of the low voltage plateau based on lithium adsorption is explored and a model of micropore closure with heat treatment temperature and exposure time is also developed.

The irreversible capacity is correlated to the adsorption of air in the micropores of the hard carbon. Two techniques based on improved dewatering procedures and a novel surface treatment are described that effectively reduce the irreversible capacity in hard carbon. These techniques will prove instrumental in the development of better hard carbon anode materials in the future.

This thesis leads to a better understanding of the large reversible capacity, the loss in reversible capacity with increased heat treatment temperatures and the irreversible capacity in hard carbon.

Chapter 1

Introduction

From the beginning of the nineties, advanced rechargeable batteries such as nickel metal-hydride (NiMH) and lithium ion (Li-ion) have started to replace nickel-cadmium (NiCd) and small sealed lead battery types. These small secondary cells (i.e. rechargeable batteries) are primarily marketed towards portable consumer electronic equipment such as notebook computers and cellular telephones. The successful market debuts of NiMH cells in 1990 and Li-ion cells in 1991 ended a long period that showed little progress in secondary cell (i.e. rechargeable batteries) technology when compared to the rapid advances in the semiconductor and electronic technology sectors.

Rechargeable Li-ion batteries have higher energy density (see table 1) and cycle life when compared to NiMH cells which are already a significant improvement over NiCd technology. In 1995, significant quantities of Li-ion batteries began being produced world-wide and the cellular telephone and notebook computer industries began to shift from NiMH to Li-ion cells. Since then production capacity has been the most serious limiting factor in the spread of Li-ion technology to other sectors. The demand for these cells is also growing at an unprecedented rate in the secondary cell industry. New technologies still hold the potential for still higher performance which has sparked billions of dollars in investment from electronic manufacturers around the world. In particular, the active electrode materials are under heavy investigation to produce cells with higher energy densities. This thesis is focused on this kind of research and

Cell Type	Voltage	Capacity	Energy
NiMH	1.2 V	3.0 Ah	3.6 VAh
Li-ion	3.6 V	1.4 Ah	5.0 VAh

Table 1.1: Comparison of the specifications of 18650 type cells for NiMH and Li-ion technologies.

specifically to understand and solve the problems associated with the implementation of hard carbon as an anode material for commercially viable Li-ion batteries.

Non-graphitized carbon, specifically petroleum coke, became an interesting anode material for Li-ion batteries during the early stages of intense research. This was due to the inability to resolve fundamental safety problems[5] with using Li-metal as the anode. Most of these problems can be traced to the high reactivity of lithium deposits formed during cycling. Although high lithium cycling efficiencies of 98-99.5% could be achieved [6], in a number of electrolyte solutions [7, 8], the Li-metal formed on charge consisted predominantly of high surface area dendrite deposits which were found to be quite reactive with the electrolyte solution at elevated temperatures. To account for the associated capacity loss of 0.5-2% [6], 5-6 times the required amount of Li-metal had to be incorporated into the cell. As the cycle life increased, more and more highly reactive large surface area deposits would be formed. This caused a decrease in thermal stability with cycle life rendering them unsafe to conditions such as short circuit of the electrodes. Thus, rechargeable Li-cells (using Li-metal anodes) were stable during early cycles but could produce serious safety hazards when abused after a number of charge/discharge cycles.

Attempts to prevent this situation led researchers towards intercalation anodes such as carbon. Li-ion rechargeable batteries are based on the "rocking chair" concept that uses two lithium intercalation compounds for electrodes. Li-atoms are inserted and removed from an intercalation compound at an energy level called the chemical potential of the lithium atom in the compound.

In order to maximise the energy stored in the battery, we would like the cell to

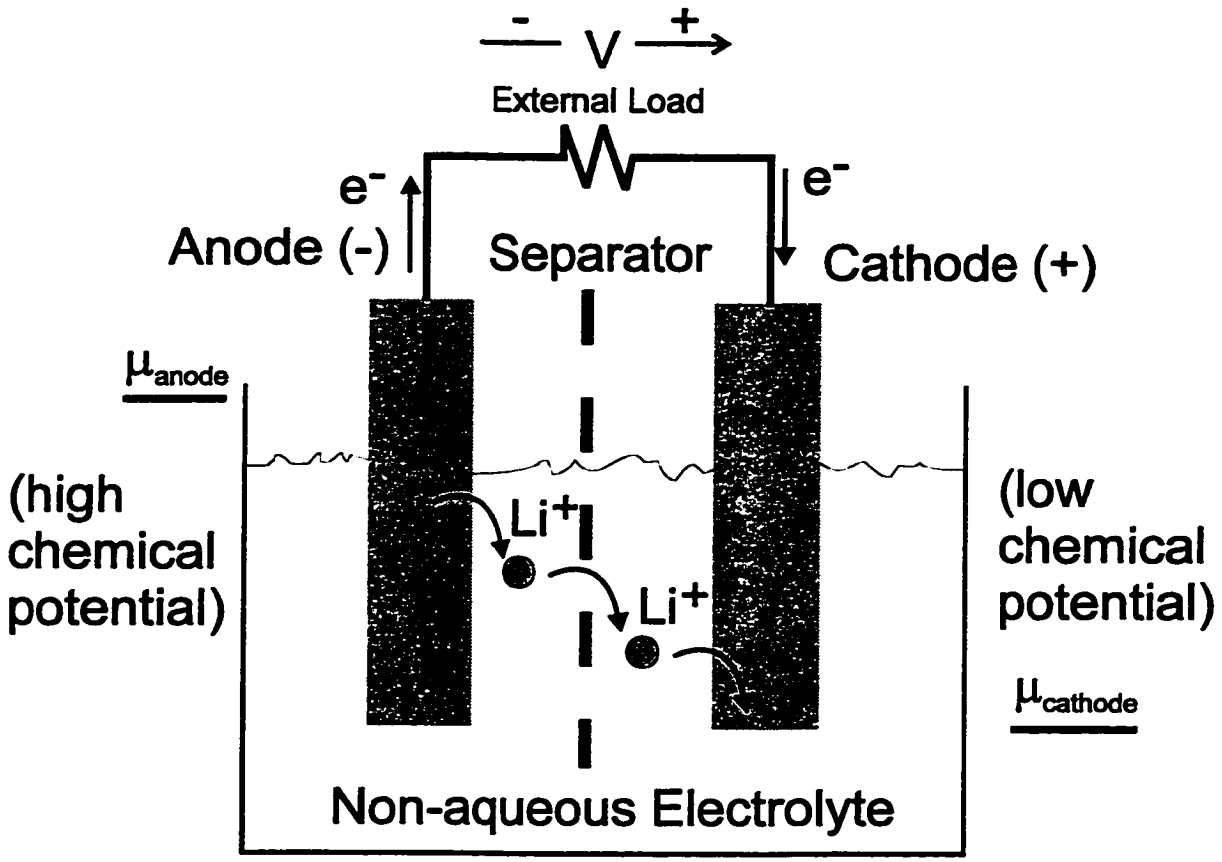

Figure 1.1: Schematic diagram of a cell discharging though an external load that could represent some electronic device or any resistive type device.

contain two very different energy levels for lithium atoms. The first energy level, the high energy state, is found in the anode and hence lithium atoms in the anode are said to have high chemical potential and low binding energy. The other energy level corresponds to the cathode, the low energy state or the low chemical potential state where Li-atoms have a high binding energy. The difference in chemical potential between the two electrodes is the amount of work that can be obtained from the cell if a Li-atom moves from the anode to the cathode. This is also the amount of energy required to charge the cell, i.e. move the Li-atom from the low energy state in the cathode to the anode.

Figure 1.1 shows pictorially a Li-ion battery during discharge. The Li-atoms originally bonded or stored in the anode with high chemical potential move as ions through the electrolyte, through the separator and become bonded within the cathode. In order to maintain charge neutrality an electron must travel through the external circuit where it can be used to drive an external load or circuit. If this overall process is energetically favourable, then an electronic current will be observed. The voltage (V) of the cell thus depends on the difference in chemical potential of Li-atoms in the two host materials.

$$V = -\frac{(\mu_{cathode} - \mu_{anode})}{e} \tag{1.1}$$

$\mu_{cathode}$ and μ_{anode} are the chemical potentials of Li-atoms in the cathode and anode materials respectively and e is the magnitude of the electron charge.

In order to produce a battery with a large potential we must maximize the difference in chemical potentials between the anode and cathode. In figure 1.2, the binding energy of Li-atoms in various intercalation compounds is shown. It is preferable to choose a cathode material with low chemical potential and hence high binding energy. The lithium transition metal oxides, $LiNiO_2$, $LiCoO_2$ and $LiMn_2O_4$ have shown the greatest promise for commercial cell applications because LiF is not an intercalation compound and $LiNiVO_4$ can only reversibly intercalate a small amount of Li-atoms.

Various types of carbon are shown in figure 1.2 to have binding energies near that of Li-metal and consequently are suitable choices to replace Li-metal. In fact there

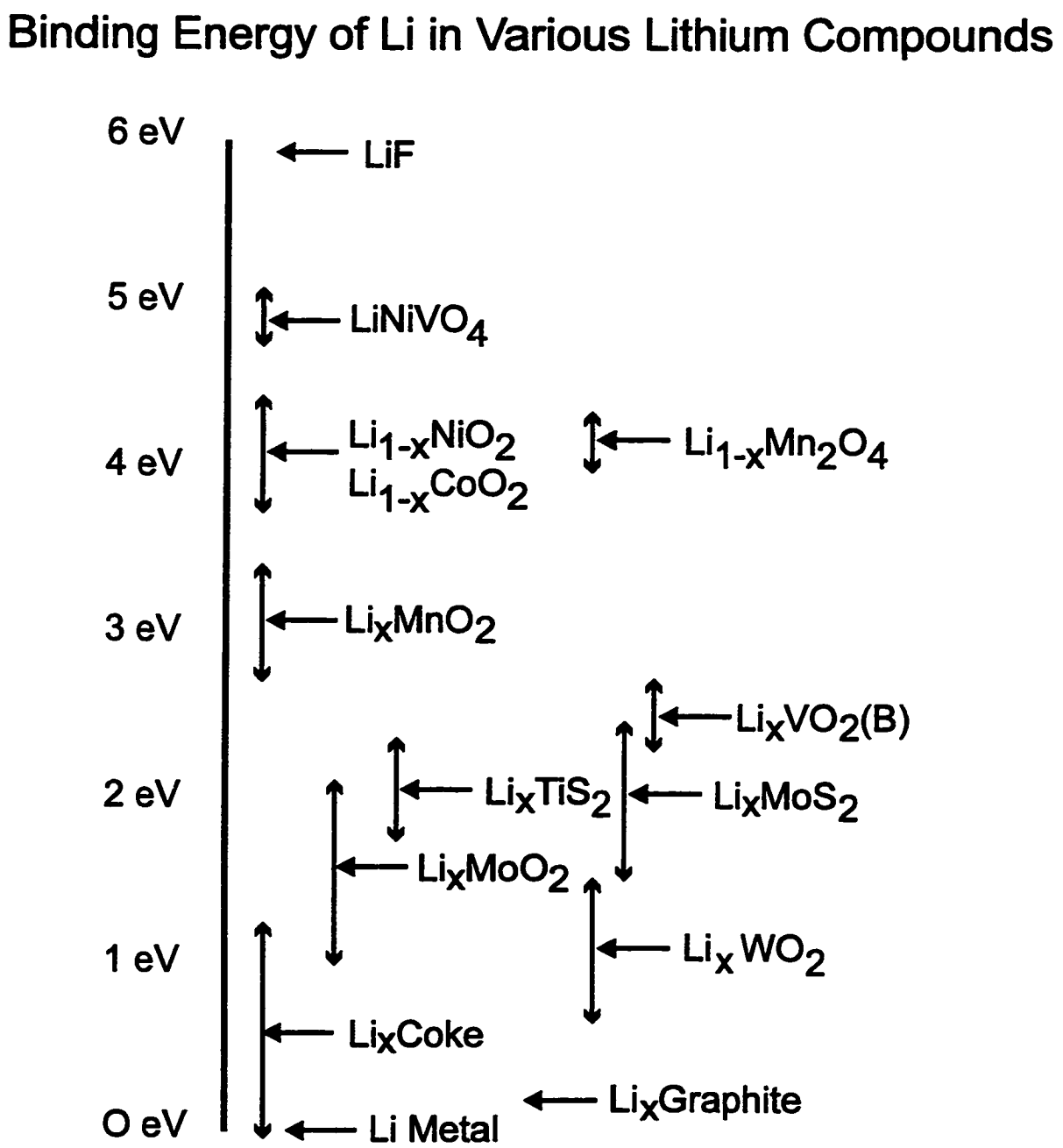

Figure 1.2: Binding energy of lithium in various lithium compounds.

are many different forms of carbon that show good capacity with low binding energy with respect to lithium metal. The advantage of carbon based anodes are significant:

1. The surface area of the electrode should remain constant during cycling to minimize changes in the safety characteristics of the cell.

2. The reaction rates between the anode and the electrolyte should be limited by the diffusion of lithium ions in the anode material. This implies that the reaction rates at high temperature should be much lower than at the metallic lithium anode.

3. Cells without excess anode capacity should be realized. This would reduce the potential for violent behaviour during worst-case scenario thermal runaway incidents.

4. The anodes do not melt under normal conditions of use or abuse. Rechargeable Li-cells can become quite dangerous if the melting point of Li is reached (180°C), due to the extreme reactivity of molten Li. Li-ion cells do not suffer from this problem.

Carbon materials can be classified in many different ways, disordered vs. graphitic, hard vs. soft, hydrogen containing vs. non-hydrogen containing and there are no doubt many other classifications as well. For Li-ion batteries, Dahn et al.[1] showed that there were three distinct classifications for carbon: the hydrogen-containing materials, single-layer hard carbons and graphitic materials as shown in figure 1.3. Lithium insertion in hydrogen containing materials was correlated to the hydrogen content by Zheng et. al. [9] and modeled analytically by Fischer and his colleagues [10, 11]. These materials exhibit large hysteresis between charge and discharge i.e. a higher voltage for removal of lithium from the carbon. For a real Li-ion battery, this correlates to a reduced cell potential (e.g. the lithium battery will charge to say 4 V but will discharge at only 3 V) and, as a result, these carbons are generally regarded as not suitable for practical lithium ion batteries. Mesocarbon micro-beads (MCMB),

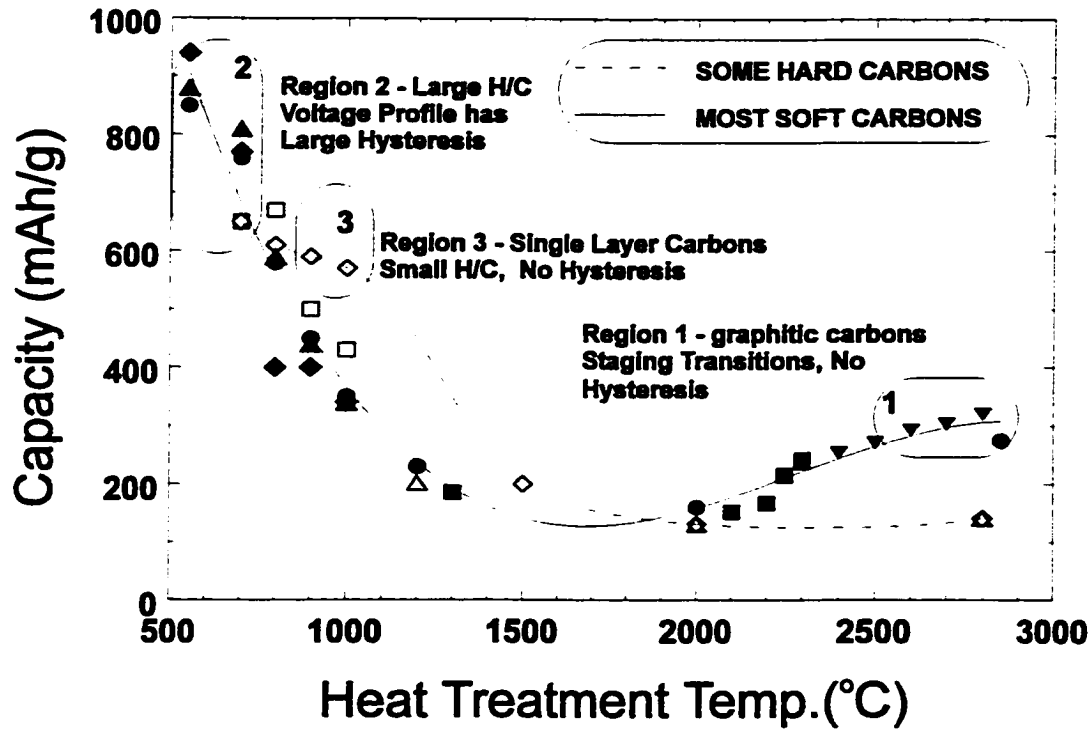

Figure 1.3: Plot of reversible capacity for lithium versus heat treatment temperature for a variety of carbon samples (open symbols, hard carbons; solid symbols, soft carbons). These data are for the second charge-discharge cycle of lithium-carbon test cells. The three regions of commercial relevance are shown. This graph has been taken from the work of Dahn et. al. [1]

an example of a graphitic material, shows good capacity at low voltage, no hysteresis and good cycling ability. For these reasons MCMB represents the current choice for battery manufacturers with few exceptions.

Hard carbon is the third distinct group of carbon materials that show promise for lithium ion batteries. These materials have a disordered structure very different from the neatly aligned graphene layers in graphite (note: a graphene layer is a single layer of carbon atoms arranged in an aromatic or honey-comb like fashion). This disordered structure naturally leads to an increase in capacity because, in a nutshell, there is more space to insert lithium ions when compared to graphite. The origin

of the capacity increase in hard carbon will be discussed in more detail throughout this thesis. In figure 1.4, a typical hard carbon voltage profile is compared to that of a graphitic material that typifies the anode materials found in commercial Li-ion batteries.

Hard carbons show larger reversible capacity but suffer from two major deficiencies: the large irreversible capacity and the hysteresis between charge and discharge in the voltage profile. These deficiencies are indicated in figure 1.4. The irreversible portion of the capacity represents the part that is lost after the first charge or discharge of a cell. Here Li-ions are irreversibly bound to the carbon electrode during the first insertion process and hence are no longer available to participate in the charge/discharge processes. The irreversible capacity represents a consumption of lithium from the cell and must be compensated by adding excess cathode material to the lithium ion cell which is both inefficient and degrades performance. The mechanism and methods for reducing the irreversible capacity in hard carbon is the focus of chapter 6.

The small hysteresis between charge and discharge is undesirable for the same reasons it is undesirable in the case of the hydrogen containing materials (i.e. the higher voltage for removal of lithium from the hard carbon represents a reduced cell potential for a real lithium ion battery). This hysteresis has been correlated to residual hydrogen content [12] and can be reduced by heating the active material to higher temperatures during pyrolysis. This, however, leads to another problem, capacity loss at high temperature, and the mechanism for this is a major focus of this thesis to which chapter 7 is devoted.

Lithium-ion cells are an exciting breakthrough in battery technology and transition metal-oxide/hard carbon is one of the more promising systems currently under development. These cells offer moderate rate capabilities [13], long cycle life [6], good temperature performance [14] and low self discharge rates [6]. Moreover, the system is safe and environmentally friendly. This thesis is primarily concerned with topics that are specific to hard carbon, the loss of reversible capacity with HTT, reducing

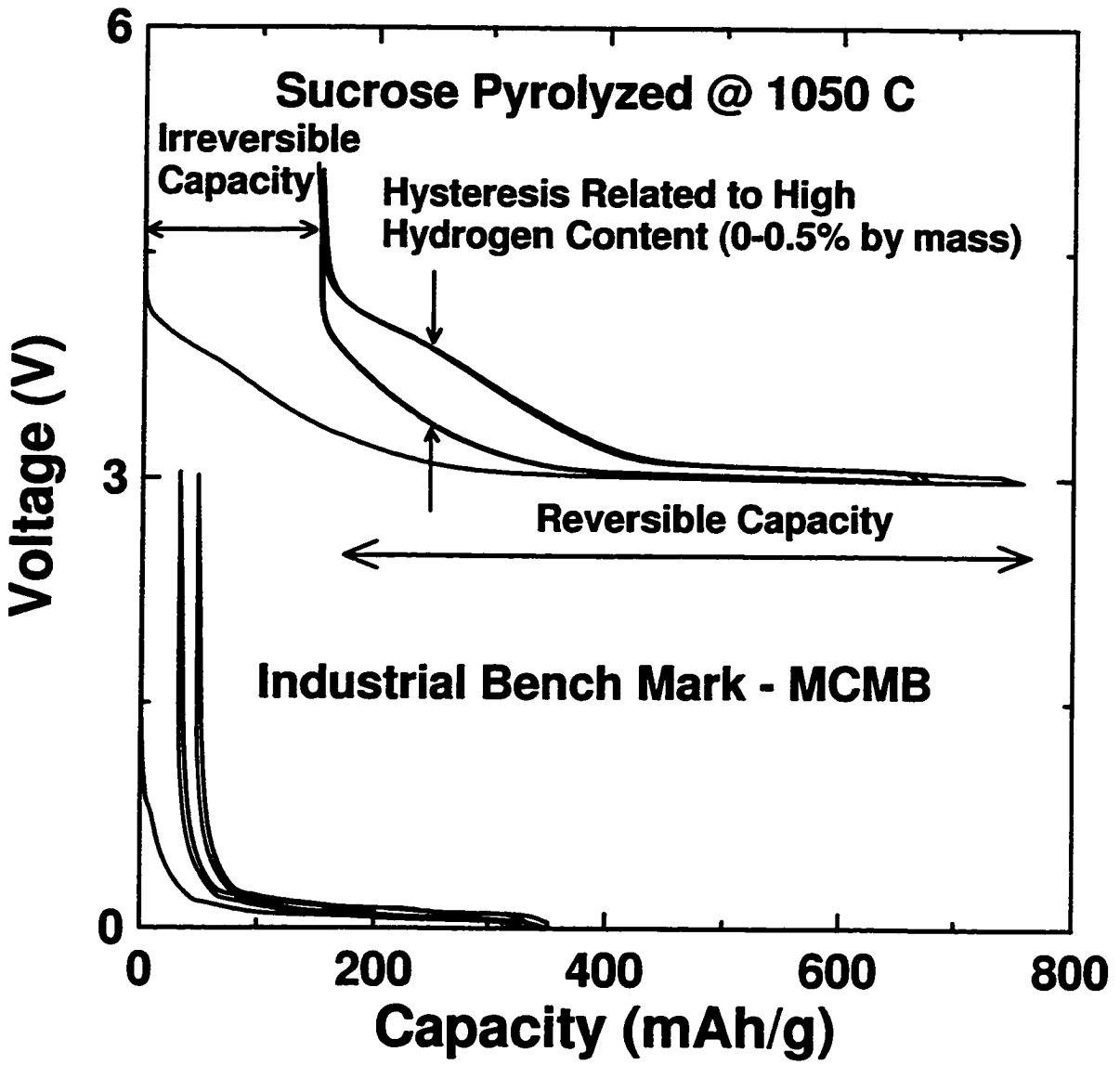

Figure 1.4: The voltage profiles of a typical hard carbon anode material and MCMB, a graphitic material. An electrochemical cell with a Li-metal negative and a carbon positive electrode was used to collect this data. The voltage plotted is the voltage of the carbon electrode measured with respect to the Li electrode.

the large irreversible capacity and developing a better understanding of the mechanisms that are responsible for the unique properties of hard carbon. In particular it is desirable to understand how these aspects relate to the structure of hard carbon and how that structure can be improved by new and improved synthesis conditions to yield materials with superior Li-ion insertion properties.

With any new active electrode material there are many issues that must be analysed before the benefits of a new material can be successfully assessed. This thesis makes no conclusions about the cycle life of hard carbon as such studies could easily double the scope of this thesis. However, previous studies[6, 14] have shown that non-graphitizable carbon has excellent cycling performance making these materials very attractive for commercial use. Petroleum coke, a disordered carbon material, was used in the first generation Li-ion battery [6] because of its excellent cycle life even though its capacity was about half that of graphitic material[14].

Chapter 2

Structure and History of Hard Carbon

Over the past 20 years, rechargeable lithium cells have been developed and demonstrated in prototype cells such as Li/TiS_2, Li/MoS_2, $Li/NbSe_3$ and Li/MnO_2 [15]. Large-volume practical batteries with metallic lithium anodes have not succeeded (yet) because of safety problems. The cells tend to fail when Li dendrites pierce the separator and short circuit the cell electrodes causing a thermal runaway situation which is enhanced by the reaction of high-area lithium powders formed during cycling. Li-metal electrodes also suffer from cascading loss of efficiency associated with the formation of isolated lithium powders, so-called dead lithium, and eventually results in the destruction of the useful lithium morphology [16, 17]. Possible alternatives to metallic lithium have also been studied, mainly alloys of compounds between lithium ($2s^1$) and the sp-elements (IIIB, IVB and VB) [18].

Carbon materials are essentially classified into two different categories depending on their structure: graphitizable carbon and non-graphitizable carbon. Franklin [2] in 1951, illustrated a model for these two different structures of graphite; as shown in figure 2.1. Compared to graphitizable materials, non-graphitizable carbon generally has low density, porous surface, small crystallites and relatively random orientation of crystallites.

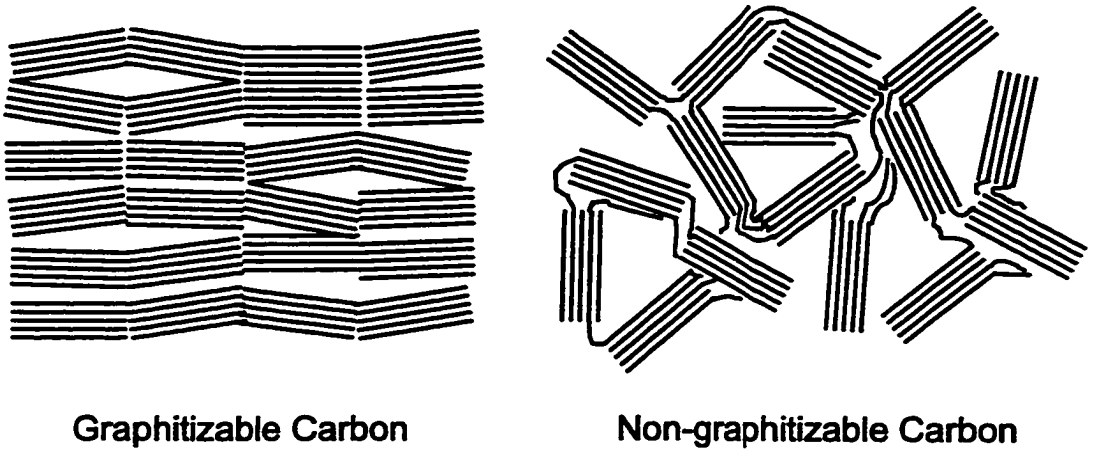

Figure 2.1: Structural models of carbon proposed by Franklin [2].

Li-ion batteries using carbon materials as an anode have attracted a great deal of attention from the scientific and industrial communities in the past five years. They are typically safer, have high energy density and lead to cells with high electromotive force [14, 6, 19]. These properties have stimulated a resurgence in the research of electrochemical intercalation of lithium in a wide range of carbon materials such as graphite[20, 21], carbon fiber[22], mesocarbon micro-beads[23], pitch coke[24] and pyrolytic carbon[25]. This chapter focuses on the progression of carbon materials from the first generation Li-ion batteries that used pitch cokes, to the second generation that use graphite and finally to the present topic of research: hard carbon.

2.1 Petroleum Coke

The first generation of Li-ion cells employed petroleum coke as the active electrode material for the anode. Coke, which is a typical graphitizable, disordered, carbon had been widely investigated in the early stage of research in anode materials [25]. Its structure can best be described as a poorly crystalline graphite having small crystallite size and random shifts or rotations between adjacent graphitic layers [6]. This type

of disorder, called *turbostratic* disorder, tends to pin adjacent layers together creating a stable material into which Li can intercalate and deintercalate. It is this stability that gives these materials their high degree of reversibility, long cycle life and their compatibility with a wide range of electrolyte solutions. However, the disorder also reduces the amount of lithium that can be intercalated to about half the value that can be achieved by highly crystalline graphite [26]. Petroleum coke has been found to have a reversible capacity of about 185 mAh/g and an irreversible capacity of about 45 mAh/g [6]. The voltage profile changes almost linearly with composition, varying by more than one volt between the fully discharged and charged states.

During the first discharge, carbon electrodes tend to show a plateau in the voltage profile at about 0.8 V which is absent on subsequent cycles. This plateau represents the electrochemical reduction of the electrolyte solution at the surface of the carbon. This reaction plays a vital role in the performance of carbon anodes. The end result of this reaction is the formation of a mechanically stable, electrically insulating, ionically conducting film that prevents any further decomposition of the electrolyte. This layer also allows the rapid transport of Li^+ ions to and from the electrode surface during the intercalation/deintercalation processes [27].

This layer formed on the surface of the carbon is similar to those formed on alkali metals immersed in nonaqueous electrolytes. Peled [28] proposed a model for the formation of this layer called the *Solid Electrolyte Interphase* (SEI). Thus, the surface films formed on anode materials are typically referred to as SEI layers. Unlike alkali metal electrodes, carbon is a noncorroding electrode and the SEI layer is only formed once during the first discharge and subsequent cycles can proceed at nearly 100% coulombic efficiency.

The formation of the SEI layer was found to irreversibly consume lithium even though its formation was essential to the cell. Fong et al. [21] showed that the SEI layer capacity for petroleum coke is directly proportional to its surface area; they reported a value of 7.0 ± 1.0 mAh/m^2. This result can be compared to the value of 7.7 mAh/m^2 reported by [6]. Thus, an additional criteria for carbon electrodes is

that they must exhibit low surface area.

Petroleum coke reversibly intercalates approximately 185 mAh/g which corresponds to a stoichiometry of $Li_{0.5}C_6$. Highly crystalline graphite has the potential to intercalate twice this capacity (Li-GIC $\rightarrow$ LiC_6). An obvious way to boost the capacity of the first generation Li-ion cells, is to replace petroleum coke with a graphitic material which has lead to the second generation of lithium ion batteries.

2.2 Graphitic Materials

The attainable capacity for lithium intercalation in graphite (Li-GIC) is generally accepted as 372 mAh/g. This is calculated from the composition of LiC_6 although Li is known to intercalate more under high temperature and extremely high pressure [29].

In order for any anode material to be successful in Li-ion batteries, it must lead to the formation of a stable SEI layer. In the early stages of Li-ion cell design, petroleum cokes were used for this reason even though graphitic materials were known to have higher capacity. At this time, graphitic materials tended to exfoliate during cycling which naturally increases the surface area of the carbon electrode and results in the constant decomposition of the electrolyte. Such an increase in irreversible capacity degrades cell performance, degrades cycle life and produces large surface area materials lowing thermal stability and leading to safety problems.

The full capacity of graphite with good cycle life was finally realised with the use of a graphitic materials formed from mesophase pitch called mesocarbon microbeads (MCMB) and the discovery that graphite could be made to cycle well with ethylene-carbonate (EC) based electrolytes. MCMB has been studied in great detail [23, 30] and for all intents and purposes the historical importance of this material is the realization of a Li-GIC with good cycle life. With the appearance of graphitic materials with larger capacity and good cycling marked the beginning of the second generation of Li-ion batteries.

This new generation of graphitic anode materials set the bench mark from which new anode materials were to be judged. In order to be useful for the next generation of Li-ion batteries, materials would have to have capacities greater than 372 mAh/g (Li_xC_6 with $x > 1$) and show good cycle life.

2.3 Hard Carbon

Once good Li-GIC materials were found, it was thought that disordered carbon materials (Li-CICs) could not produce higher lithium insertion capacities due to the large degree of turbostratic disorder. This made the first reports of non-graphitizable carbon prepared from polyfurfuryl alcohol (PFA-C) [31, 32, 33, 34, 35], with reversible capacity of ≈350 mAh/g and excellent cycle life, such a surprise in the Li-ion battery community. Accordingly Li-ion battery researchers showed a renewed interest in non-graphitizable carbons such as PFA-C.

Disordered carbon materials can be prepared by heating some carbon-containing samples in inert atmospheres to temperatures between 500 and 3000+°C; by a process commonly referred to as pyrolysis. Consequently, the appearance of PFA-C based disordered carbons began an intensive period where just about any carbon containing material was pyrolysed and analysed for its capacity for lithium insertion. The range of precursor materials that were reported ranged from epoxy resins, to carbohydrates, to almost every carbon-containing by-product of the petroleum industry, to coal, etc. [36, 37, 38, 9, 39, 40, 41, 42, 43].

These materials could be characterized into three distinct groups[1] as was explained in chapter 1. Of particular importance is the special classification of disordered carbons, the single layer hard carbons, that show capacities greater than 372 mAh/g. These materials show essentially the same initial capacity as petroleum coke during discharge but also feature a large low voltage plateau below 0.1 V (as shown in figure 1.4) with respect to Li-metal [40, 41, 42, 43].

There have been many attempts to model the large capacities shown in some

hard carbons i.e. >372 mAh/g or Li_xC_6 with x>1. Wang et al. [44] proposed that the increased capacity was a result of lithium species binding to the edges and surface of the small graphitic crystallites. Another more ambitious researcher [36] proposed that two lithium layers could be inserted between graphene sheets leading to a stoichiometry of Li_2C_6 or 744 mAh/g. However, Sawai et al. [13] showed that such a material could not be structured in a compact way because of the strong Li-Li repulsive interaction. To weaken the Li-Li interaction would require polarized molecules or sufficient distances, conceivably 10 Å[13] or more, between layers and thus it is unlikely that two lithium layers could be inserted between graphene layers.

Much of the problem with the new theories was the misinterpretation of the structure of these disordered carbons. They were based on the assumption that the crystallites were made of essentially parallel stacked graphene sheets and hence they tried to explain the increase in capacity in terms of edge and surface effects. However, once the wide-angle X-ray diffraction patterns were correctly analysed [45, 46, 43] and researchers realized that these materials with large capacity were predominantly composed of single-layer graphene sheets, new more realistic theories began to emerge.

An early discovery of single-layer hard carbons was made by Hirsch [45] in 1954 who analysed the average number of stacked layers in different coal materials. This was accomplished using the Patterson function [47] calculated by the application of Fourier integral analysis to the experimental X-ray diffraction pattern. His results suggested that apart from the singly occurring layers, for all the coals he studied, the most frequently occurring groups contain two or three layers (in that order) and had a thickness of ~7 to 10 Å.

Imoto et. al. [46] applied the technique of calculating the Patterson function to various non-graphitizable carbons such as heat-treated polyfurfuryl alcohol (PFA-C), petroleum coke and graphitizable carbons. Their work correlated an increase in lithium insertion capacity to a decrease in the number of parallel stacked graphene sheets in the samples. They showed that the PFA-C materials with capacities greater than 372mAh/g contained at least 45% single layers by weight and graphitizable

samples prepared from petroleum coke with capacity ~280 mAh/g had 25-30% single layers.

Liu et al. [43] developed a method for calculating the intensity of a group of graphene sheets containing an arbitrary number of layers. In the same paper, the "house of cards" model was developed to explain how capacities greater than LiC_6 could be achieved due to the relatively random orientation of graphene sheets. Liu et al. also showed that the micropores created in these disordered materials were of the order of 12 Å, which agreed with the analysis of Sawai et al. [13] who argued that the separation between graphene sheet needed to accommodate two layers of lithium atoms was of the order of 10 Å.

Li NMR and ESR studies by Takami et al. [48] showed a shift in ^{7}Li NMR spectra during lithium insertion in disordered carbons with condensed aromatic rings. This shift indicates that the lithium insertion in the low voltage plateau is distinct from that above 0.1 V. However, they did not speculate on the physical significance of the new site for lithium insertion.

In this thesis, an interpretation of lithium insertion along the low voltage plateau, consistent with the model proposed by Sonobe et. al. [40], will be given for hard carbon materials. It will be argued that during discharge, the capacity above 0.1 V is predominantly the intercalation between turbostratically disordered graphitic layers which is very similar to the capacity found in petroleum coke materials. Lithium insertion along the low voltage plateau will be correlated to the micropore structure for the first time, and may result in the formation of small metallic lithium particles inside the micropores. Of course for micropores with diameter of 12 Å this may be semantics since the adsorption of two layers in such a pore will basically fill the micropore. However, the second and higher layers will be inserted at near the Li-metal chemical potential due to the screening of the carbon substrate by the first layer of Li-atoms. This is what we refer to as the formation of small Li-metal particles inside the micropores.

2.3.1 Irreversible Capacity in Hard Carbon

The irreversible capacity problem has plagued the usefulness of hard carbon for Li-ion battery applications. Before this thesis, there has been a significant amount of work done by many research groups[49, 4] to determine the origin of this irreversible capacity. Of particular importance is the work done by Xing et al. [4] which showed that the large irreversible capacity in hard carbon was a result of the exposure of the electrodes to air before cell fabrication. They also showed that the large irreversible capacity was correlated to a plateau in the first discharge curve at about 0.8 V which has been previously correlated to the formation of the SEI layer [6]. These results were instrumental in determining methods for the reduction of the irreversible capacity presented in chapter 6.

Chapter 3

Li-ion Electrochemical cells

Hard carbon is prepared by the pyrolysis of organic precursors. Pyrolysis (Greek: *pyros*, a fire, + *lysis*, a loss) is the heating of something in the absence of air until it decomposes. The air-free environment is crucial otherwise the sample would simply burn until nothing remained. The following unbalanced reaction is given as an example that describes the pyrolysis of glucose to produce hard carbon (containing a small residual amount of hydrogen) and decomposition gases such as water and carbon dioxide:

$$C_6H_{12}O_6 \rightarrow HardCarbon(C_{100}H) + H_2O + CO_2 + CH_4 + H_2 + \ldots \quad (3.1)$$

In this chapter, the procedure used to make coin-type cells to test the electrochemical properties of active electrode materials is explained. This includes a description of the different precursor materials, the dewatering process for non-polymerized precursors, argon and vacuum pyrolysis methods, coin cell fabrication and electrochemical testing using constant current methods.

3.1 Choice of Precursor

Precursors that make good anode materials are pyrolysed carbohydrates such as fructose, glucose, sucrose, wood and coconut shells, as well as other pyrolysed organic

materials such as lignin, epoxy resins, etc [31, 32, 36, 37, 38, 9, 39, 40, 41, 42, 43]. In fact, almost all carbon-containing substances will produce active electrode materials with at least a limited amount of lithium insertion capacity. Of particular interest is the pyrolysis of carbohydrates such as sucrose, glucose and fructose that yield hard carbons with large reversible capacity. The optimum pyrolysis process requires temperatures above 900°C and produces essentially a pure carbon material with small hydrogen content (< 0.5 % by mass).

Hard carbon is the name given to the group of carbonaceous materials that exhibit highly disordered, non-graphitized structures after pyrolysis. These materials typically do not form a liquid phase during pyrolysis while soft carbons do and show more graphitic characteristics. Another important difference is that hard carbons tend to be formed from precursor materials that are more strongly cross-linked and hence resist both the formation of a liquid phase and graphitization during heating.

3.1.1 Dewatering of the Organic Precursor

Monosaccharides and disaccharides are distinct from polysaccharides in that they release a large amount of water when they are initially heated. The word saccharide comes from the Latin word *saccharum* meaning sugar. Monosaccharides are single sugar molecules such as fructose and glucose. Disaccharides consist of two monosaccharides; e.g. sucrose contains one fructose and one glucose molecule joined together by a glycosidic linkage. The formation of these linkages results in the polymerization of the saccharide molecules into larger molecular structures. This process is called, or at least what we call, dewatering (or condensation synthesis to organic chemists) because the by product of this process is the release of water and it occurs at temperatures between 130-140°C. For example, sucrose is formed by the condensation synthesis of fructose and glucose as shown in figure 3.1. Two hydroxide functional groups on neighbouring saccharides react to form the glycosidic linkage and release one water molecule. The remaining hydroxide functional groups will in turn react, if the process is allowed to continue, resulting in the formation of larger molecular solids

and the release of more water molecules until the substance is fully polymerized and no more glycosidic linkages can be formed.

It is the random cross-linking of saccharide molecules during the dewatering process that lays the framework for the disordered hard carbon that follows from pyrolysis. With out getting into the theory of X-ray diffraction, we can see from wide-angle X-ray scattering (WAXS) measurements on raw sucrose, dewatered sucrose and pyrolysed sucrose (see figure 3.2)that the well ordered microcrystalline structure of sucrose has been completely lost after dewatering. Although it is still significantly different from the pyrolysed material, the WAXS pattern of dewatered sucrose shows only the broad features that are indicative of a highly disordered material.

The dewatering process can be optimized to reduce the irreversible capacity in hard carbon. Whereas most hard carbons show irreversible capacities of about 150mAh/g or higher, precursors that experience dewatering can show irreversible capacities as low as 50 mAh/g. For this reason, monosaccharides and disaccharides are vastly superior to polymer precursors like wood, coconut shells, starch, cellulose and lignin that have always displayed large irreversible capacities. In the section devoted to this topic, the dewatering process and irreversible capacity are correlated in much more detail.

The dewatering process is carried out by heating the precursor in a muffle oven at a specified temperature (usually 180°C) in air. After 1-2 hours the precursor will melt, decompose and solidify. The solidified remains are then ground into powders suitable for pyrolysis. This process is distinct from pyrolysis because it is carried out in air (simply for convenience) and at much lower temperatures than pyrolysis. One might wonder what effects the direct pyrolysis of the precursor materials might have, however since the dewatering temperature is much lower than the ignition point for hard carbon (400°C), no significant improvements are observed. Furthermore, the liquid phase formed during dewatering makes it very difficult to contain the sample in the tube furnace and this is particularly difficult under vacuum pyrolysis conditions.

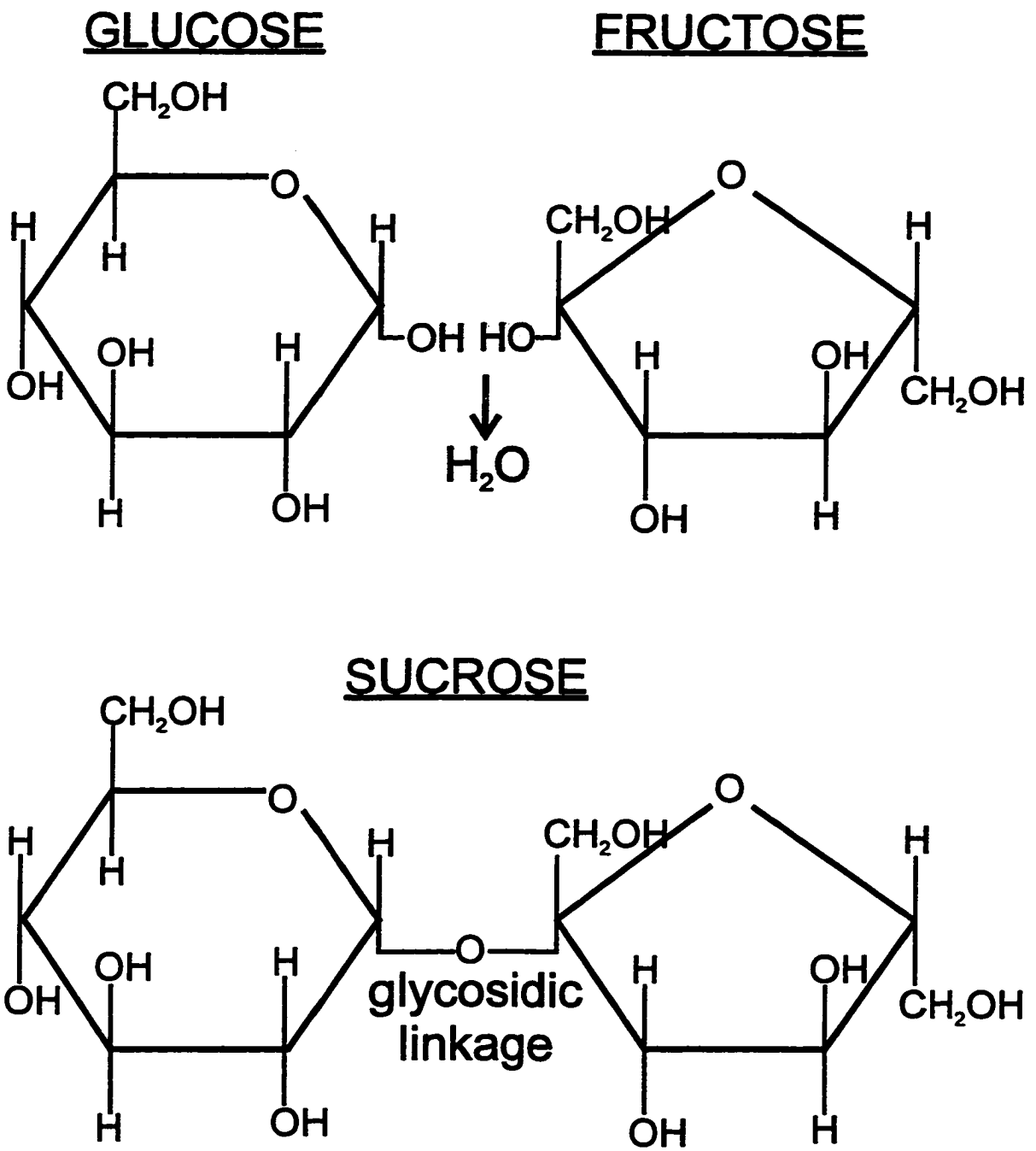

Figure 3.1: The condensation synthesis of sucrose from glucose and fructose. Notice that many H and OH sites are available for additional condensation reactions that would produce long chain polysaccharides such as starch.

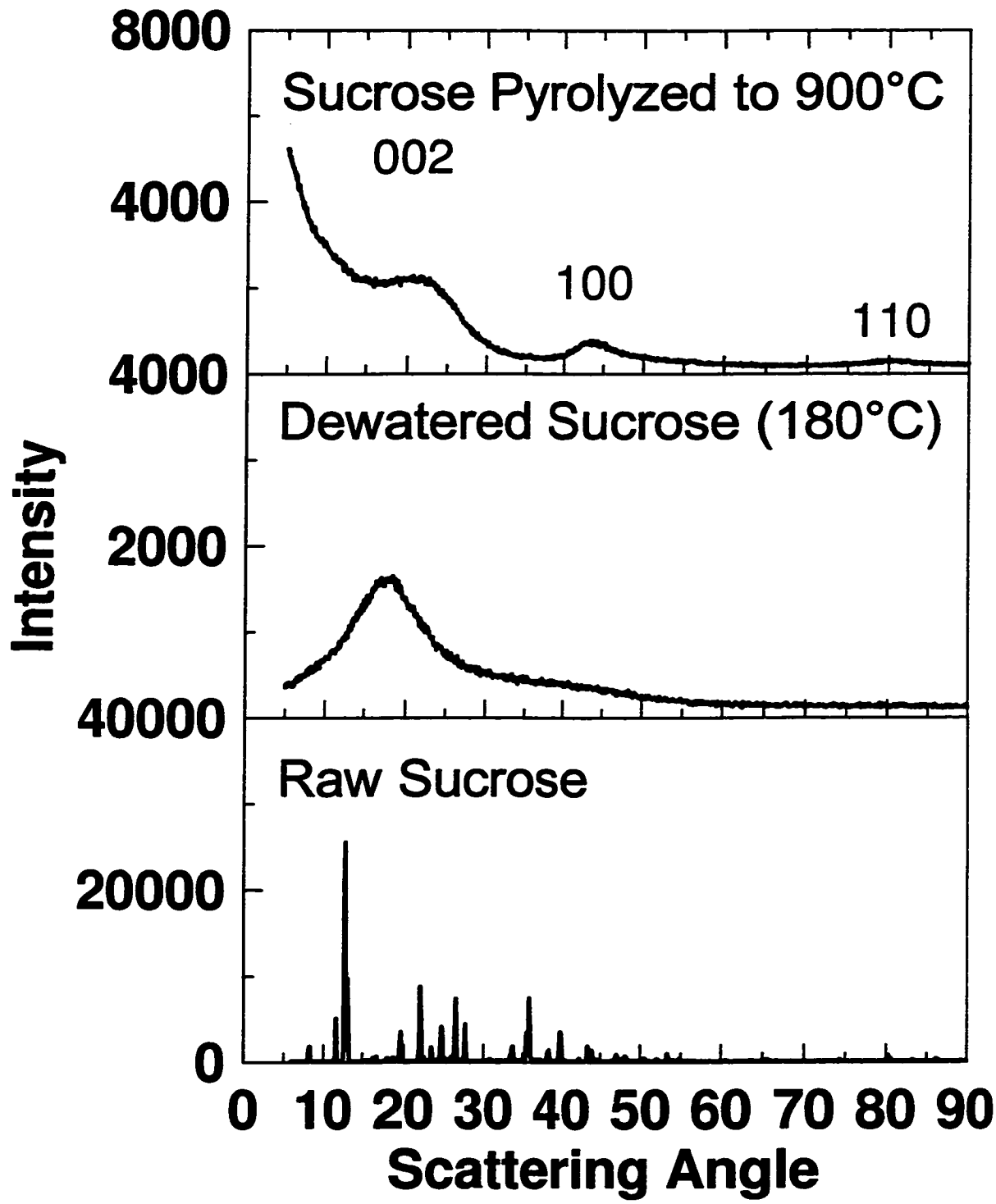

Figure 3.2: The WAXS patterns for raw sucrose, dewatered sucrose and pyrolysed sucrose.

Pyrolysis

The purpose of pyrolysis is to heat the sample and, by decomposition, produce an essentially pure carbon material. Unfortunately the sample can be burnt off by gases in the system that might include air leaking into the system or the decomposition gases produced by the sample itself. Two obvious decomposition gas are H_2O and CO_2. These are known activating agents that are used in the active carbon industry to partially burn-off hard carbon materials for filtering applications. Burn-off not only reduces the yield of the sample, which in itself is a minor problem, but it changes the surface chemistry of the sample that causes significant increases in the irreversible capacity and generally has dramatic ill effects of the voltage profile [42]. Hence it is imperative that these gases be removed from the sample as quickly as possible.

Two methods of ensuring that environment around the sample remains inert is to perform the pyrolysis of the sample in vacuum or in a flow of an inert gas. The vacuum pyrolysis system had to be constructed to ensure that the decomposition gases could not reach the pump or else it would eventually fail during operation. In figure 3.3 the apparatus for both methods of pyrolysis are shown and each will be discussed in the following sections.

The argon pyrolysis method uses flowing argon to remove any air from the sample tube and to draw the decomposition gases away from the sample. It is a simple system to set up and works well if there is sufficient flow of argon to remove the decomposition gases that may activate the sample. This generally requires that the flow of argon gas be no less than 200 ml/min (for a 2 in dia. quartz tube). Many of the samples studied were prepared using this technique.

Vacuum pyrolysis is likely the best way to ensure that neither air or the decomposition gases come in contact with the sample. It is, however, a much more complicated system that includes a vacuum pump, a cold trap to prevent exposing the pump to corrosive gases, an automated system to control the level of liquid nitrogen in the cold trap and the entire apparatus must be vacuum sealed to pressures < 10 mTorr. Xue et al [42] showed that even the smallest amount of burn-off to oxygen caused

large increases in the irreversible capacity and generally had dramatic negative effects on the electrochemical properties of the resulting materials. This vacuum pyrolysis system was developed as the optimum method to remove any such activating agents from the system and to understand how this would affect the quality of the resulting active electrode materials. Unfortunately no dramatic improvements in electrochemical properties where found and it was concluded that vacuum pyrolysis and argon flow pyrolysis were essentially equivalent if the argon flow rate was at least 200 ml/min.

Once the samples are in either the argon flow or vacuum pyrolysis furnaces, the method of pyrolysis is essentially the same. That is, the samples are both prepared in the same way, degassed the same length of time and pyrolysed with the same temperature program. The samples are prepared by grinding the dewatered precursor and placing six grams a nickel boat. The samples are then degassed at 100°C (in either a vacuum or flowing argon) for at least one hour prior to pyrolysis. Xing and Dahn[50] describe the optimum methods for pyrolysing sugar to make Li-ion battery materials. We follow their method closely. During pyrolysis the sample was first heated at 50°C/min. to 200°C, then at 1°C/min. to 450°C and finally at 10°C/min. to a final pyrolysis temperature where the sample remained for 1 hour. Essentially the furnace temperature must not ramp up too quickly causing the sample to release more gas than can be removed by the system. The samples were then cooled to room temperature at 50°C/min. and removed from the tube furnace. The samples were ground in an automatic grinder for ten minutes to produce a powder suitable for electrochemical testing.

3.2 Electrode Preparation

Making the electrodes involves mixing the sample with small amounts of carbon black, a binder material and an organic solvent for the binder that is subsequently spread out over a copper current collector to form the electrode. The carbon black additive is used to increase the conductivity of the electrode. The binding agent is PVDF

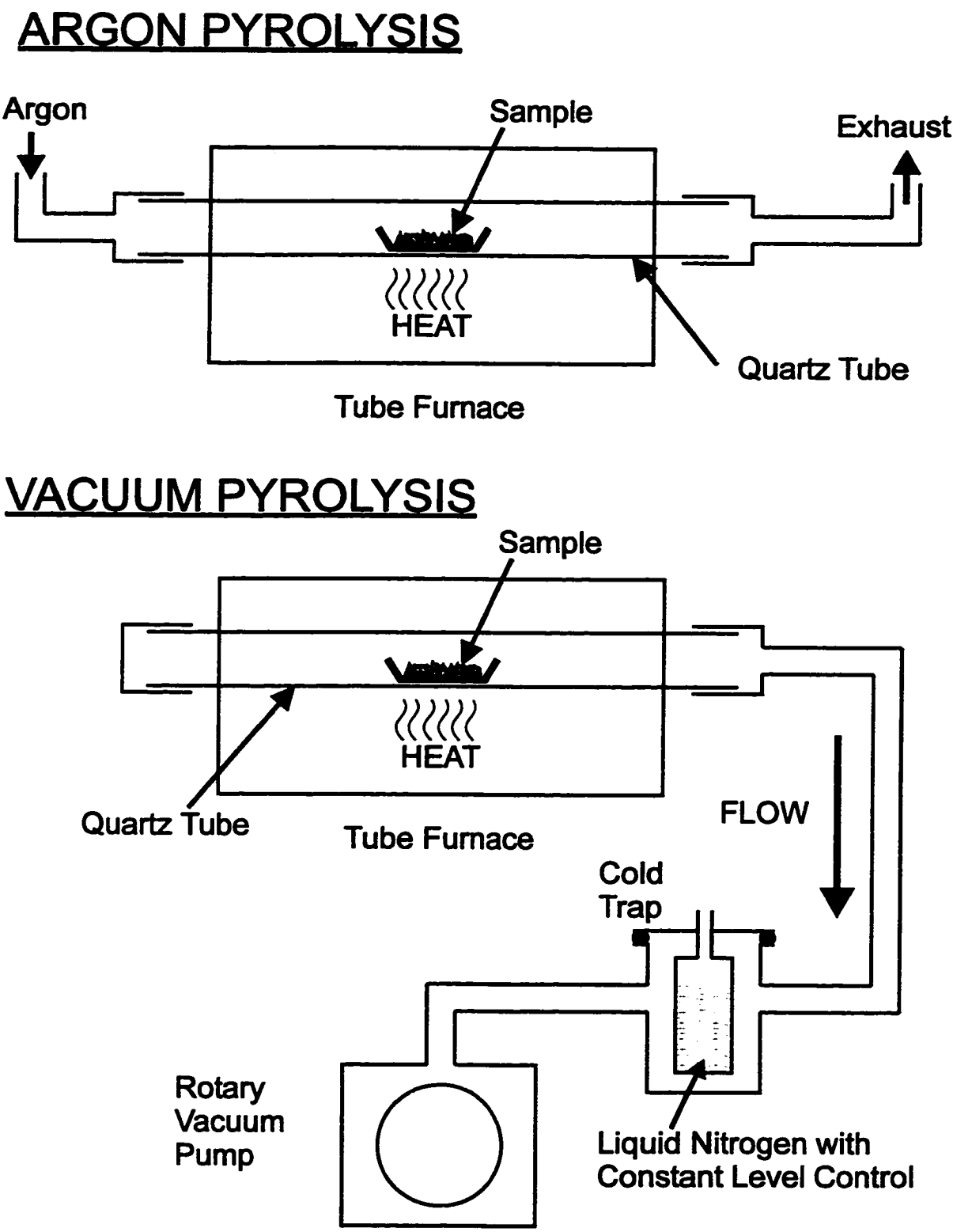

Figure 3.3: Schematic diagram of the argon flow and vacuum pyrolysis systems used to prepare the hard carbon samples.

dissolved in NMP. NMP is also added to thin the slurry so that it can be spread evenly onto the electrode.

The electrodes were prepared by mixing the ground samples with 5% Super S (maintains electrical conductivity during cycling) and 5% PVDF (binder) by weight. The slurries were then thinned with NMP and spread onto copper electrodes. These electrodes were dried at 110°C for at least 2 hours and then cut into electrodes suitable for making coin cells.

3.3 Cell Construction

Cells consist of the prepared electrode as the cathode, lithium metal as the anode, a Celgard separator, electrolyte and cell hardware. The detailed schematic diagram of the cell is shown in figure 3.4. The electrolyte used was 1M $LiPF_6$ in a 1:2 volume ratio of ethylene carbonate (EC) and diethyl carbonate (DEC). A microporous film separator (Celgard 2400), wetted with electrolyte, was sandwiched between the carbonaceous cathode and a Li metal foil anode. The spacer and spring are used to provide cell stack-pressure that essentially keeps all parts of the cell in electrical contact. These cells are constructed in an argon filled glove box.

3.4 Electrochemical Testing

Electrochemical testing of active electrode materials is done using lithium metal as the anode in order to isolate the chemical potential of the material under study. This is possible since Li-metal has a constant chemical potential. The voltage of a real cell, $V = \frac{-(\mu_{cathode} - \mu_{anode})}{e}$, depends on the chemical potential of both electrodes and thus if two intercalation compounds were used, one could not determine which features in the voltage profile correspond to which electrode.

In a real lithium ion cell, hard carbon would be used as the anode, however, in our test cells vs. lithium metal, the hard carbon is the cathode. The discharge

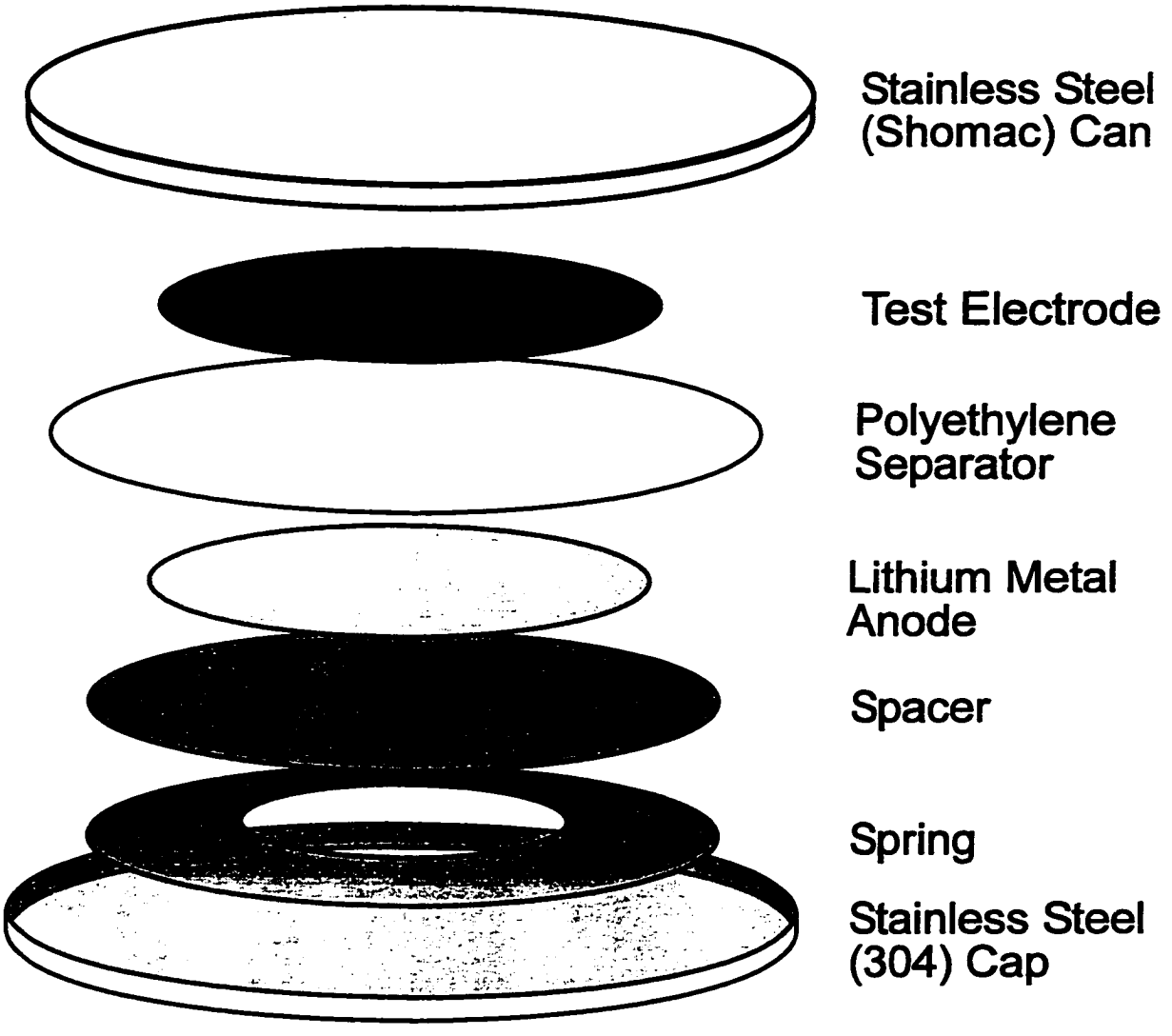

Figure 3.4: Schematic diagram of the 2325 coin cell hardware used for electrochemical testing of electrode materials.

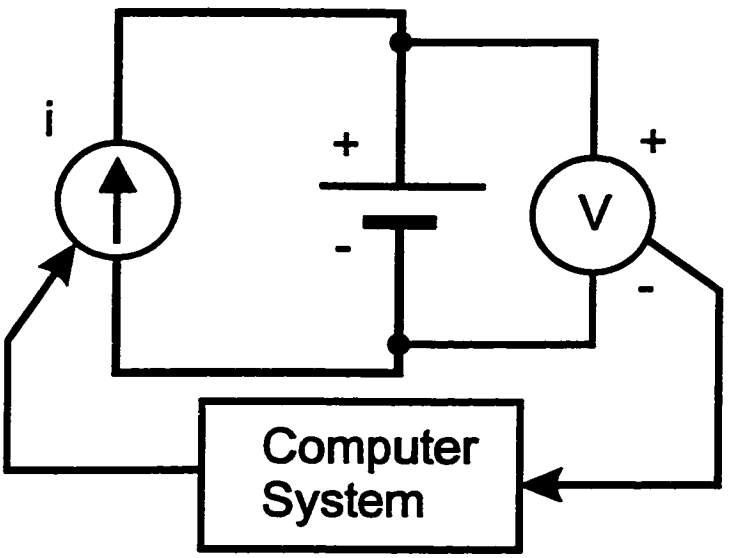

Figure 3.5: Schematic diagram of a simplified charger system. The cell is connected to a constant current source that is controlled by the computer system depending on the voltage of the cell. The voltage is recorded for constant current discharge and charge as a function of time.

cycle for this half cell corresponds to the insertion of lithium into the hard carbon material. This is opposite to the real cell situation where the discharge process would correspond to the transfer of lithium from the hard carbon to the transition metal oxide cathode. This is a subtlety that can become very confusing.

The test cells are cycled under constant current conditions based on LiC_6 as a bench mark capacity. We use LiC_6 as a reference because it represents the theoretical maximum capacity for graphite which is used heavily by industry. Materials with higher capacity than LiC_6, say $Li_{1.5}C_6$ for hard carbon, are very interesting from a commercial stand point. A Moli Energy charge-discharge system was used to measure the electrochemical behaviour of the cells and a simplified schematic diagram of the system is shown in figure 3.5.

Since the capacity of a new material is unknown before the electrochemical testing is started, a charge/discharge current is based on the bench mark capacity of LiC_6.

That is, we choose a rate that would insert one Li for every six carbon atoms in a time x. This rate is given the distinction C/x. For consistency a C/20 rate (fills the test electrode with one Li for every six carbon atoms in 20 hours) is always used which is slow enough to give near-equilibrium results while yielding a useful amount of data in a reasonable amount of time. Obviously the capacity will not necessarily be LiC_6 and in most cases it is larger and so the test electrode continues to charge past the twenty hour mark. It continues until the electrode reaches full capacity and lithium metal begins to plate on the surface of the electrode at which time the current is reversed, the cell is recharged to 3V and the discharge process is repeated. The methods used to distinguish plating and stripping of Li from insertion of Li into carbon are described next. This method was described by Liu et. al. [43] and we follow their methods closely.

Hard carbon has significant capacity for lithium insertion near the chemical potential of lithium metal. In order to determine the total capacity of a hard carbon electrode, lithium is inserted into the test electrode until lithium plating occurs. This corresponds to the point where the chemical potential of lithium insertion equals that of lithium metal and it becomes energetically favourable to plate lithium on the surface of the electrode. The equilibrium cell potential is zero volts, however, because current is flowing through the cell, a voltage slightly below zero is measured due to the non-zero internal impedance of the cell.

The point at which Li-metal begins to plate on the surface is easily observed in the voltage profile because it corresponds to an increase in cell potential. This is caused by a sudden decrease in the cell impedance resulting from the elimination of lithium diffusion into the electrode. The different stages of cycling a hard carbon test electrode with respect to Li-metal is shown in figure 3.6. This cell has been allowed to plate/strip lithium metal for longer periods of time than would normally be necessary in order to emphasize the different phases of a discharge/charge cycle. Notice the large increase in cell potential that indicates the onset of lithium plating. The plating/stripping region of the voltage profiles are removed manually for all of

the voltage profiles that are reported in this thesis.

The current calculation proceeds as follows: for LiC_6 the total number of lithium atoms, per unit mass of carbon, is calculated as follows:

$$\#\ \text{Li-atoms} = \frac{1}{6} \times \frac{1mol}{12.011g} \times 6.02 \times 10^{23} \frac{atoms}{mol} = 836 \times 10^{19} \frac{\text{Li-atoms}}{\text{g}} \tag{3.2}$$

The valence of a Li-ion is +1 and so we can convert the number of lithium ions to a specific capacity by multiplying by the charge e on an electron and dividing by 3600 seconds.

$$\text{specific capacity} = 836 \frac{\text{Li-atoms}}{\text{g}} \times e(1.602 \times 10^{-19}) \times \frac{1h}{3600s} = 372 \frac{mAh}{g} \tag{3.3}$$

This result represents the specific capacity for graphite (Li-GIC) and is used to calculate the test currents for the active electrodes in the test cell. More specifically, we divide this result by the time we choose to charge the cell and multiply by the mass of the active electrode material on the electrode. For example a C/20 rate corresponds to charging a cell to 372 mAh/g in 20 hours. Hence we would calculate the current (I) as follows:

$$I = \frac{372mAh/g \times \text{active mass}}{20h}$$

The constant current cyclers have current stability to $\pm 1\%$. The cells were housed in thermostats at $30 \pm 0.1^{o}C$.

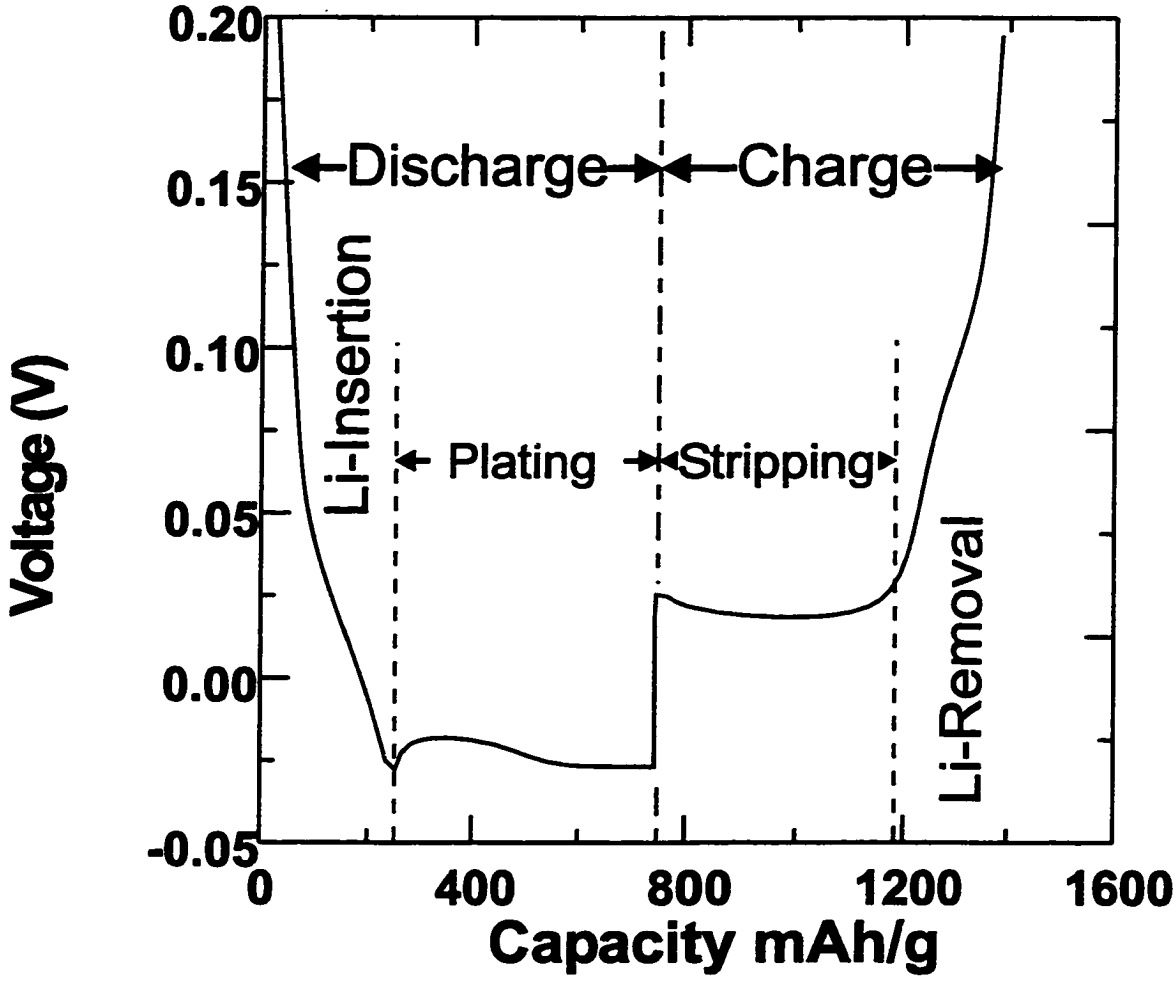

Figure 3.6: The low voltage region of a typical hard carbon voltage/capacity curve has been expanded to show the processes that occur during cycling. The onset of plating/end of stripping has been indicated by the dashed vertical lines. The vertical center line corresponds to the switch from discharge to charge.

Chapter 4

Experimental Techniques and Characterization of Hard Carbon

Hard carbon is a unique material with unique characteristics. It has a highly disordered structure with predominantly single layer graphene sheets arranged in a pseudo-random fashion. This structure can be thought of as a "house of cards" [43] where single, double or triple layers of graphene sheets represent the cards. The space created in the voids between cards can be thought of as micropores.

Powder X-ray diffraction, called wide angle X-ray scattering here (WAXS), small angle X-ray scattering and BET surface area measurements are very effective in describing the surface and bulk properties of hard carbon [42]. The use of these techniques with emphasis on the analysis of the structure of hard carbon is presented in this chapter. The last remaining tool, CO_2 gas adsorption, has been developed specifically to analyse the micropore structure in hard carbon and a detailed explanation of this technique is given in chapter 5.

4.1 Wide Angle X-ray Diffraction

WAXS is a very useful tool for determining the structures of materials that show periodic behaviour. For crystalline materials, this is typically the periodic arrangement of atoms to form the crystalline lattice. For hard carbon, a material made of predominantly single layers of graphene sheets, we are primarily interested in using WAXS measurements to determine the number of graphene sheets (on average) that are stacked in parallel.

Typical interatomic distances in solids are on the order of an angstrom (10^{-8}cm). An electromagnetic probe of the microscopic structure of a solid must therefore have a wavelength that is close to this length. The corresponding photon energy is of the order

$$\hbar\omega = \frac{hc}{\lambda} = \frac{hc}{10^{-8}\text{cm}} \approx 12.3 \times 10^3\text{eV}. \tag{4.1}$$

These energies are characteristic X-ray energies and a typical source is the Cu K_α transition that produces an X-ray with λ=1.54Å. In this section, various theories of X-ray diffraction are outlined and a method of determining the fractions of single, double and triple layers in hard carbon is explained. For a more detailed description of the theory behind these techniques the reader is referred to solid state physics textbooks such as Ashcroft and Mermin [51] or Kittel [52].

4.1.1 Bragg Formulation of X-Ray Diffraction by a Crystal

In 1913 W.H. and W.L. Bragg found that crystalline substances gave remarkably characteristic patterns of reflected X-radiation that are very different from those produced by liquids. W.L. Bragg was able to explain this by regarding the crystal as parallel planes of ions, spaced a distance d apart. The conditions for a sharp peak in the intensity of the scattered radiation were: (1) the reflected X-rays should be specularly reflected and (2) that the reflected rays from successive planes should interfere constructively. Specularly reflected waves from atomic planes are shown in figure 4.1. The path difference between the two rays is $2d\sin\theta$ and, in order for these

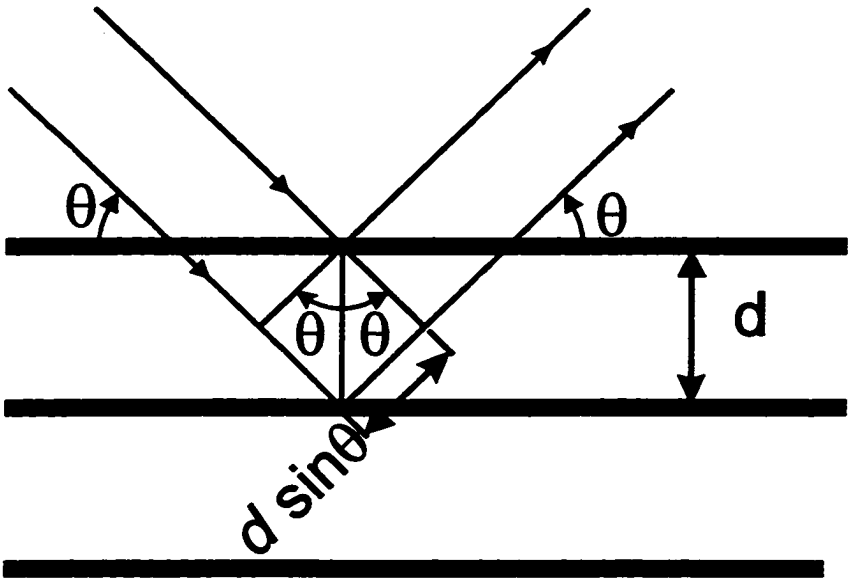

Figure 4.1: Bragg reflection from a particular family of reference planes, separated by a distance d. Incident and reflected rays are shown for two neighbouring planes.

rays to interfere constructively, the path difference must equal an integral multiple of the wave length. This leads directly to the celebrated condition for Bragg reflections to occur:

$$n\lambda = 2d\sin\theta. \tag{4.2}$$

The integer n is known as the order of the corresponding reflection. Not only are there higher-order reflections but the crystal can be sectioned into many different planes, each of which will produce further reflections.

4.1.2 Von Laue Formulation of X-Ray Diffraction by a Crystal

The von Laue approach differs from the Bragg formalization in that no particular lattices planes are sectioned out from the crystal and no assumption of specular reflection is imposed. The crystal is comprised of identical scattering centers (atoms or ions) placed at positions R of a Bravais lattice, each of which can radiate the incident radiation in all directions. Sharp peaks are observed only in directions and at wavelengths for which the rays scattered from all lattice points interfere constructively.

To find the condition for constructive interference, consider two scattering centers, separated by a distance d at the positions R *and* 0 as shown in figure 4.2. Let X-rays with wave vector $\mathbf{k} = 2\pi\hat{\mathbf{n}}/\lambda$ be incident from far away, along a direction $\hat{\mathbf{n}}$. Assuming these X-rays are elastically scattered, X-rays in the direction $\hat{\mathbf{n}}'$ will have a wave vector $\mathbf{k}' = 2\pi\hat{\mathbf{n}}'/\lambda$.

Peaks in the scattered wave intensity will be observed if the difference in path length between the two rays is an integral multiple of the wave length. From figure 4.2, the path length difference (pld) can be calculated from the projections of the two wave vectors onto the incident and scattered wave vector directions, i.e.

$$\text{pld} = \mathbf{d} \cdot (\hat{\mathbf{n}} - \hat{\mathbf{n}}') \tag{4.3}$$

The condition for complete constructive interference is:

$$m\lambda = \mathbf{d} \cdot (\hat{\mathbf{n}} - \hat{\mathbf{n}}'), \tag{4.4}$$

for integral m. Multiplying both sides by $2\pi/\lambda$ yields

$$2\pi m = \mathbf{d} \cdot (\mathbf{k} - \mathbf{k}'). \tag{4.5}$$

Next, we consider not just two scattering centers but an array of scatters corresponding to the positions of atoms in a Bravais lattice. A Bravais lattice is an infinitely repetitive arrangement of points in space that fulfils the condition that the environment of each point is identical to that of every other point. There are fourteen

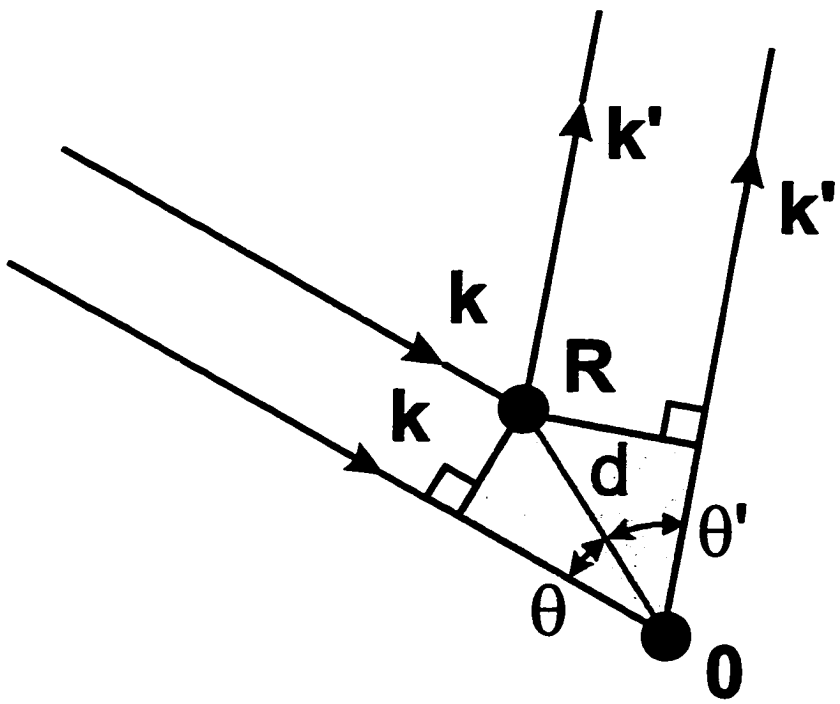

Figure 4.2: Illustrating the path difference between two X-ray scattering centers separated by a distance d at R and O.

such arrangements. Points (or essentially atoms) on the Bravais lattice are separated by Bravais lattice vectors $\mathbf{R}$. The condition for all the scattered rays to interfere constructively is that equation 4.5 must hold for all values of $\mathbf{d}$ corresponding to Bravais lattice vectors:

$$2\pi m = \mathbf{R} \cdot (\mathbf{k} - \mathbf{k}'). \tag{4.6}$$

Taking the exponential of both sides of equation 4.6 gives a more convenient condition for constructive interference,

$$e^{i(\mathbf{k}-\mathbf{k}')\cdot\mathbf{R}} = 1, \text{ for all Bravais lattice vectors } \mathbf{R}. \tag{4.7}$$

This condition parallels the construction of the reciprocal lattice. Such a lattice is constructed from the set of points that constitute the Bravais lattice and a plane wave $e^{i\mathbf{k}\cdot\mathbf{r}}$. This plane wave, for general $\mathbf{k}$, will not have the periodicity of the Bravais lattice, but for certain special choices it will. This brings about the definition of the reciprocal lattice, i.e. *the set of plane waves with wave vector* $\mathbf{K}$ *that have the periodicity of a given Bravais lattice is known as the reciprocal lattice.* Analytically, the construction of plane waves from the reciprocal lattice vectors can not be affected by translations by Bravais lattice vectors because the environments of each of these points is identical, i.e.

$$e^{i\mathbf{K}\cdot(\mathbf{r}+\mathbf{R})} = e^{i\mathbf{K}\cdot\mathbf{r}}. \tag{4.8}$$

This result must hold for any choice of $\mathbf{r}$ in the Bravais lattice. Factoring out the common exponential term leads to a convenient definition of the reciprocal lattice vectors $\mathbf{K}$ for a given Bravais lattice:

$$e^{i\mathbf{K}\cdot\mathbf{R}} = 1. \tag{4.9}$$

Now it can be seen that the condition for constructive interference given by equation 4.7 is equivalent to the construction of the reciprocal lattice provided the change in wave vector between the incident and scattered wave is a vector with in the reciprocal lattice, $\mathbf{K} = \mathbf{k}' - \mathbf{k}$. This is known as the Laue condition for constructive

interference. Although it will not be shown here, the Laue condition and Bragg condition are equivalent. Bragg's assumption of spectral reflection is equivalent to the assumption by von Laue that the rays scattered from individual ions within each lattice plane interfere constructively. Thus both the Bragg and the von Laue approaches are based on the same physical assumptions and their precise equivalence is to be expected [51].

4.1.3 Calculating the Scattered X-ray Intensity

The Bragg and von Laue descriptions of X-ray scattering have been confined to materials with well defined crystal structures that show characteristic intensity peaks in their measured X-ray diffraction patterns. These two description have lead to the equivalent predictions of the peak positions but can not be used to calculate the arbitrary intensity as a function of the scattering wave vector or scattering angle.

Calculating the structure factor $S_{\mathbf{K}}$ for a general scattering vector $\mathbf{K}$, allows for such a calculation. It is not confined to calculating intensities for constructive interference or Bragg reflections but calculates the intensity for arbitrary scattering direction by summing the amplitude and phase of all the scattered waves. This is illustrated in figure 4.3 which is essentially a simplified version of figure 4.2 where the geometry of the problem has been simplified.

The scattered amplitude from an amorphous material is essentially the sum of the amplitude and phase of the scattered waves from all the atoms in the material with respect to some arbitrary origin. Each different atom will coherently scatter X-rays described in terms of the atomic scattering factor f. This scattering factor is the ratio of the amplitude of the radiation scattered by the atom to the amplitude of radiation that a single electron would scatter under the same conditions according to classical theory. In the nonrelativistic approximation the scattering factor is given by

$$f(\mathbf{q}) = \int \psi_f^*(\mathbf{r}) * e^{i\mathbf{q}\cdot\mathbf{r}} \psi_i(\mathbf{r}) dv \tag{4.10}$$

where ψ is the total wave function of the atom, the subscripts i and f refer to the

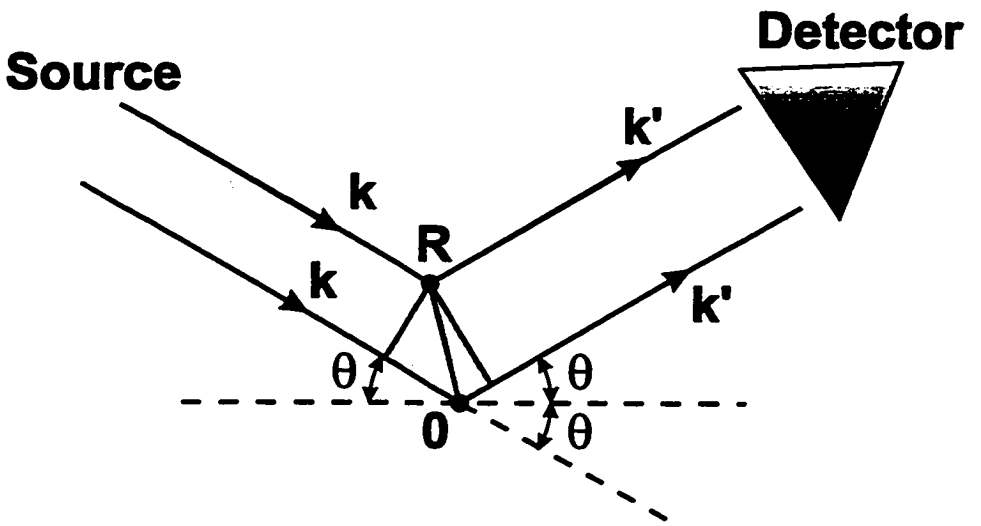

Figure 4.3: Illustrating the path difference between two X-rays scattered from the origin and an atom at position **R** with respect to the origin. In this case the geometry of the incident and scattered waves have been specified to be more consistent with most experimental apparatus.

initial and final states and $\mathbf{q} = \mathbf{k}' - \mathbf{k}$.

The atomic form factor for carbon has been calculated using relativistic Hartree-Fock wave functions as explained in [3]. The atomic form factor for carbon is thus given by the analytical expression

$$f(\mathbf{q}/4\pi) = \sum_{i=1}^{4} a_i e^{-b_i(q/4\pi)^2} + c \tag{4.11}$$

where $a_1 = 2.31000$, $b_1 = 20.8439$ Å^2, $a_2 = 1.02000$, $b_2 = 10.2075$ Å^2, $a_3 = 1.58860$, $b_3 = 0.568700$ Å^2, $a_4 = .865000$, $b_4 = 51.6512$ Å^2 and $c = 0.215600$. The atomic form factor has been plotted versus scattering angle assuming X-rays of wavelength 1.54 Å in figure 4.4.

The scattered wave is calculated by summing the amplitudes and phase differences of scattered waves,

$$S(\mathbf{q}) = \sum_{i=1}^{N} f_i(\mathbf{q}) e^{-i\mathbf{q}\cdot\mathbf{R}_i}. \tag{4.12}$$

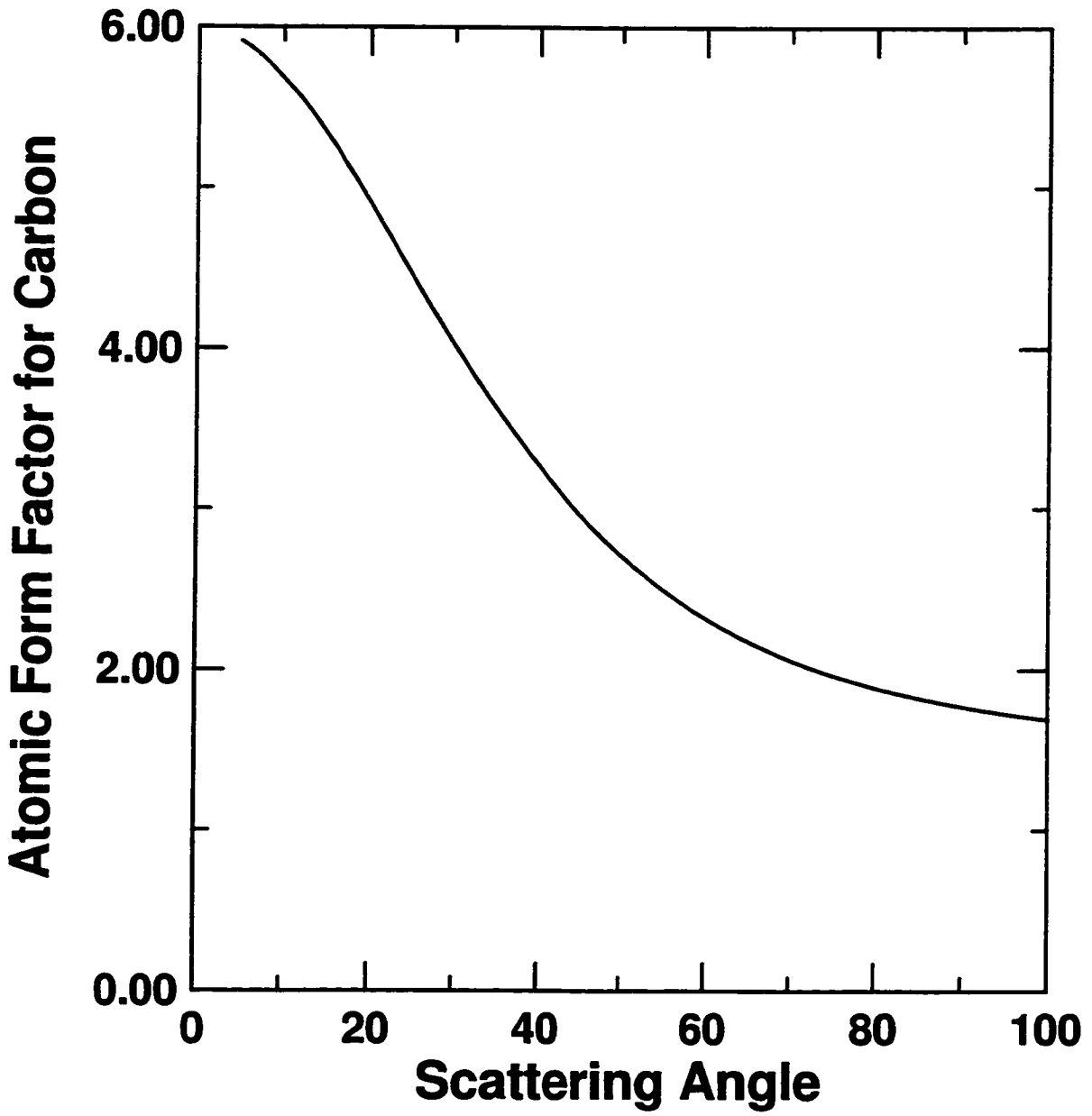

Figure 4.4: The calculated atomic form factor for carbon based on relativistic Hartree-Fock wave functions [3].

where the sum is carried out over all atoms, $f_i(\mathbf{q})$ is the atomic form factor and $\mathbf{R_i}$ represents the position of the atom. This equation can be used to calculate the scattered X-ray intensity if the position and type of the atoms that make up the material are known. The measured intensity is related to the amplitude of the scattered wave $S(\mathbf{q})$ by the relation

$$I = S(\mathbf{q})^* S(\mathbf{q}). \tag{4.13}$$

This method will be used to calculate the intensity of scattered X-radiation from randomly arranged graphene sheets and the average micropore size in the small-angle X-ray arrangement.

4.1.4 The Ewald Construction

The simple geometric construction of Ewald helps to visualize the requirements for constructive interference to occur. The Ewald sphere is drawn in reciprocal or k-space as shown in figure 4.5. Constructive interference will occur for some value of $\mathbf{k}'$ provided that the sphere intersects one of the reciprocal lattice points, hence satisfying the Laue condition.

In general, a sphere in k-space will not intersect any of the reciprocal lattice points for a general incident wave vector. The Ewald construction shows the difficulty in measuring the Bragg peaks of a material. The Powder or Debye-Scherrer method uses samples that are either polycrystalline or ground into fine powders. This ensures that all possible orientations of the crystal are available and capable of diffracting X-rays because the grains or particles are enormous on the atomic scale.

4.1.5 Sample Preparation and Experimental Technique for WAXS

Carbon samples used for powder X-ray diffraction were obtained by grinding the as-made pyrolysed samples. The powder X-ray diffraction patterns were measured using

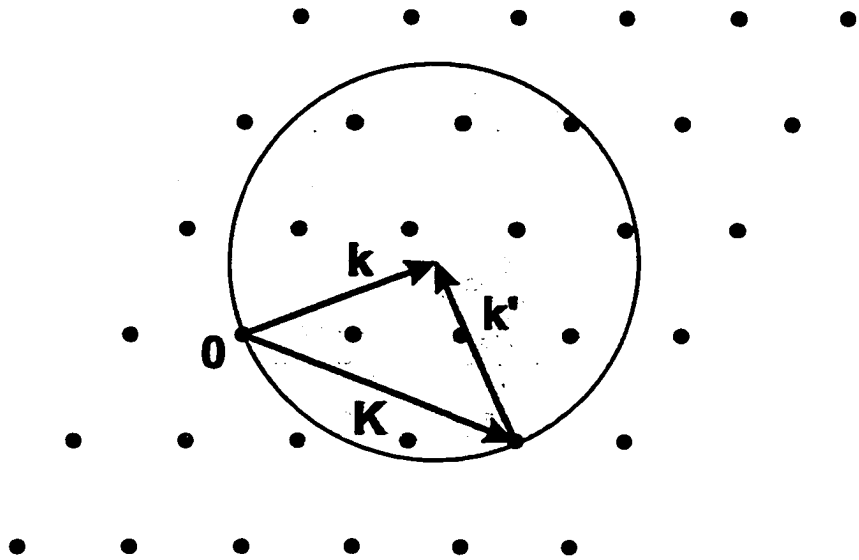

Figure 4.5: The Ewald construction. Given the incident wave vector **k**, a sphere of radius k is drawn about the point **k**. Diffractions peaks will occur for some value of **k'** provided that the sphere intersects one of the reciprocal lattice points **K**.

a Siemens D5000 powder diffractometer equipped with a copper target X-ray tube and a diffracted beam monochromater. The D5000 operates in the Bragg-Brentano geometry as shown in figure 4.6. The samples were packed into a rectangular well 25 mm × 20 mm × 2 mm deep made of stainless steel that acted as the sample holder. The long dimension of the well is aligned with the plane of the incident and scattered beams to help ensure the beam remains on the sample and does not come in contact with the stainless steel at low scattering angle. The sample remains fixed during the measurement and the detector and source arms move simultaneously in opposite angular directions. The divergence and anti-scatter slits used in almost all instances were 0.5°. The receiving slit was set at 0.6 mm and these selections result in an instrumental resolution of about ±0.15° in the scattering angle 2θ. All the measurements were made between 10° and 100° in scattering angle.

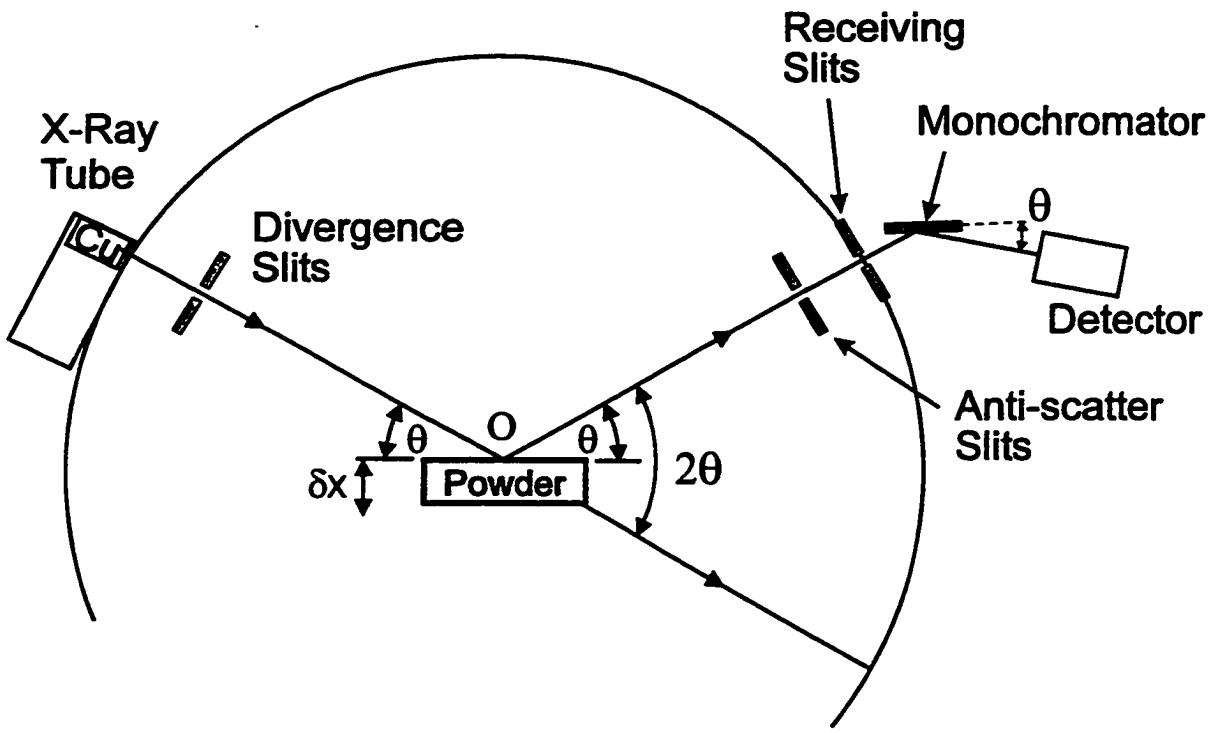

Figure 4.6: Schematic diagram depicting the operational geometry of the powder X-ray diffraction apparatus used to measure the diffraction patterns of the studied carbonaceous materials.

4.1.6 Graphite Structure

There are two different graphite structures, 2H and 3R, that differ in the stacking of graphene layers; both are hexagonal. The less common graphite structure exhibits rhombohedral stacking (3R) that has an ...ABCABC... stacking pattern. The B layers are shifted as in the (2H) structure and the C layers are shifted by the same amount, in the same direction, with respect to the B layers. Each of these shifts represents a displacement of 1/3 the (110) unit cell distance, thus giving rise to the ABC stacking arrangement.

Most natural forms of graphite show the layered 2H structure having a space group $P6_3/mmc$ (hexagonal; $a = 2.456$ Åand $c = 6.696$ Å) in which all carbon atoms are equivalently located in the 4(f) sites [13]. The bonding between graphene layers (3.35 Å of layer separation) is feeble compared to that of carbon-carbon bond (1.42 Å). The unit cell of the 2H structure is shown in figure 4.7. The stacking sequence of the 2H structure is ...ABABAB... where the adjacent layers are shifted 1/3 of the distance along the (110) direction. This positions a carbon atom directly above the center of the aromatic ring in the layer below.

The most common choice for the Bravais lattice vectors are:

$$\begin{aligned} \mathbf{a}_1 &= \frac{\sqrt{3}}{2}a\hat{\mathbf{x}} + \frac{1}{2}a\hat{\mathbf{y}}, \\ \mathbf{a}_2 &= -\frac{\sqrt{3}}{2}a\hat{\mathbf{x}} + \frac{1}{2}a\hat{\mathbf{y}}, \\ \mathbf{a}_3 &= c\hat{\mathbf{z}}, \end{aligned} \tag{4.14}$$

where a=2.456 Å and c is 6.696 Å[13]. The spacing between planes is surprisingly almost 2.4 times the C-C in-plane distance. This description of graphite does not form a primitive Bravais lattice, i.e. one where all the atoms are touched by Bravais lattice vectors. In order to include the positions of the remaining atoms in the unit cell, a basis for those atoms must be constructed. It is common to reference their location with respect to the origin of the Bravais lattice vectors. The basis for graphite

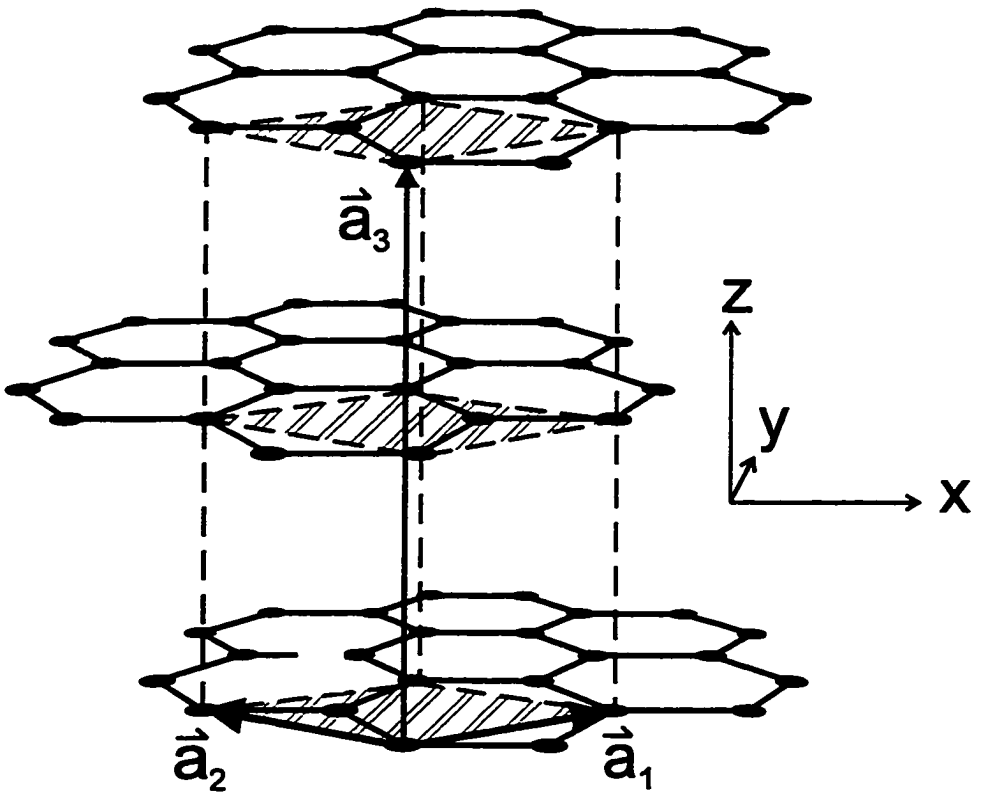

Figure 4.7: 2H structure of graphite showing the unit cell and unit cell vectors.

contains four atoms, one at the origin and three others:

$$
\begin{aligned}
(0,0,0) &= \text{origin}, && (4.15)\\
(\tfrac{1}{3},\tfrac{2}{3},0) &= \tfrac{2}{3}\mathbf{a}_1 + \tfrac{1}{3}\mathbf{a}_2, && (4.16)\\
(0,0,\tfrac{1}{2}) &= \tfrac{1}{2}\mathbf{a}_3, && (4.17)\\
(\tfrac{2}{3},\tfrac{1}{3},\tfrac{1}{2}) &= \tfrac{2}{3}\mathbf{a}_1 + \tfrac{2}{3}\mathbf{a}_2 + \tfrac{1}{2}\mathbf{a}_3. && (4.18)\\
& && (4.19)
\end{aligned}
$$

The reciprocal lattice of a real-space hexagonal lattice is another hexagonal lattice. The reciprocal lattice vectors for the real-space graphite lattice defined by 4.14 are:

$$
\begin{aligned}
\mathbf{b}_1 &= \frac{4\pi}{\sqrt{3}a}(\frac{1}{2}\hat{\mathbf{x}} + \frac{\sqrt{3}}{2}\hat{\mathbf{y}}),\\
\mathbf{b}_2 &= \frac{4\pi}{\sqrt{3}a}(-\frac{1}{2}\hat{\mathbf{x}} + \frac{\sqrt{3}}{2}\hat{\mathbf{y}}),\\
\mathbf{b}_3 &= \frac{2\pi}{c}(\hat{\mathbf{z}}). && (4.20)
\end{aligned}
$$

4.1.7 The Geometric Structure Factor for Graphite

The von Laue description of X-ray diffraction from a crystal structure was based on the criteria that the scattered waves from the primitive cell interfere constructively. If the crystal structure contains an n-atom basis then the each primitive cell must by further analysed into a set of identical scatterers positioned at $\mathbf{d_1}, ..., \mathbf{d_2}$ within the cell. The intensity of radiation in a given reciprocal lattice vector direction will depend upon the amount to which the basis atoms interfere with one another. The net ray scattered by the entire primitive cell is the sum of the individual rays scattered from each of the basis atoms. If the Bravais lattice was primitive, the basis would contain only the origin and the structure factor $S_{\mathbf{K}}$ would be 1. However, graphite has a four atom basis and the contribution for each atom must be considered, i.e.

$$S_{\mathbf{K}} = \sum_{j=i}^{n} e^{i\mathbf{K}\cdot\mathbf{d}_j}, \qquad (4.21)$$

where $\mathbf{K}$ represents all possible reciprocal lattice vectors defined by $h\mathbf{b}_1 + k\mathbf{b}_2 + l\mathbf{b}_3$ and $\mathbf{d}_j$ are the basis vectors as defined in 4.15. The sum can be calculated to produce the following result for $S_{\mathbf{K}}$:

$$S_{\mathbf{K}} = 1 + e^{i\pi l} + e^{i\frac{2\pi}{3}(h+2k)} + e^{i\pi(\frac{2}{3}(2h+k)+l)}, \tag{4.22}$$

The values of $S_{\mathbf{K}}$ and the corresponding scattering angle (2θ) for a few selected (hkl) type refections are tabulated below:

h k l (type)	$S^*_{\mathbf{K}}S_{\mathbf{K}}$	2θ
002	2 × 16	26.5°
100	6 × 1	42.4°
101	12 × 3	44.6°
102	12 × 1	50.8°
110	6 × 16	77.7°

Table 4.1: Calculated values of the structure factor $S_{\mathbf{K}}$ and the calculated scattering angle of the given hkl type reflections.

4.1.8 Structure of Hard Carbon

Hard carbon is the name given to carbonaceous materials that exhibit a random orientation between graphene sheets. The lack of long range ordering between graphene sheets appears in the measured WAXs data showing only broad features. Determining the atomic positions in terms of basis and unit cells loses all meaning when considering such disordered materials. In fact, what little short range order exists in the material is due to the arrangement of small numbers of graphene sheets.

Understanding the measured WAXS curves begins by constructing the material graphene sheet by graphene sheet. Essentially we are trying to determine the average number of graphene sheets stacked parallel to each other. By combining different ratios of the X-ray diffraction patterns calculated from single, double, triple and

higher numbers of parallel layers, we can try to fit the observed X-ray diffraction patterns and hence develop an idea of how the material is structured.

First, however, the powder diffraction intensity for various graphene sheet arrangements must be calculated. Since we are only interested in the interactions of graphene planes with others, we are primarily interested in the 002 Bragg reflection in the direction normal to the plane of the graphene sheet. This calculation was performed by Hang Shi in his Ph.D. thesis [53] where he calculated the powder intensity I for M parallel stacked graphene sheets (with infinite lateral extent),

$$I(q) = f^2(q)\frac{1}{q^2}\left[1 + 2Re\left(\sum_{n=1}^{M-1}\frac{(M-n)}{M}e^{inqd_{002}}\right)\right]. \tag{4.23}$$

where q is the scattering vector and f(q) is the atomic form factor and d_{002} is the spacing between adjacent layers in the hard carbon. The term $1/q^2$ is the result of powder averaging and the term in square brackets is the weighted sum of phase factors for the graphene sheets. For our purposes we only need the contributions from single, double and triple layers of graphene sheets, for reasons that will become more apparent later, and from equation 4.23 those results are:

$$\text{1 layer} \Rightarrow \frac{f(q)^2}{q^2} \tag{4.24}$$

$$\text{2 layers} \Rightarrow \frac{f(q)^2(1+\cos qd)}{q^2} \tag{4.25}$$

$$\text{3 layers} \Rightarrow \frac{f(q)^2(1+\frac{4}{3}\cos qd+\frac{2}{3}\cos 2qd)}{q^2} \tag{4.26}$$

The first result for a single layer is fairly obvious; there is no phase factor because there is no interference for only one layer. The second equation, is easy to reconstruct if we consider two parallel planes stacked on top of each other, separated by a distance d_{002} as shown in figure 4.8.

Using equation (4.12), the structure factor can be calculated. Since **q** and $\mathbf{d}_{002}$ are aligned in the same direction, only the distance of atoms normal to the plane of

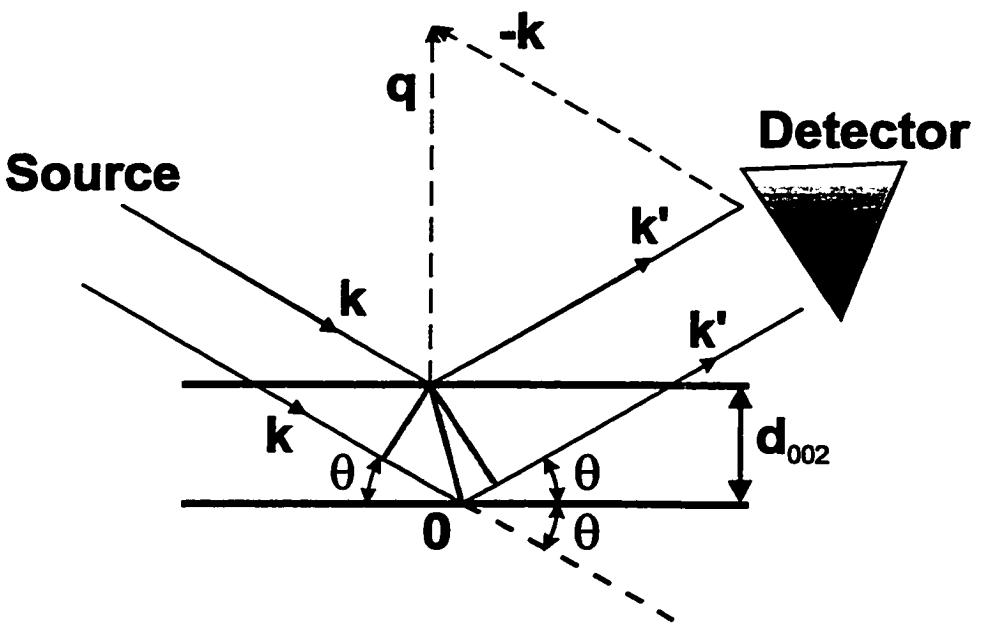

Figure 4.8: Two graphene layers separated by a distance d_{002}. The normal to the graphene planes is aligned with the scattering vector q so that only the atomic positions along this direction are important.

the graphene sheet are important. Thus,

$$\begin{aligned} S(q) &= f(q) * (1 + e^{iqd}), && (4.27)\\ I(q) &= S^*S = f(q)^2 * (1 + e^{iqd})(1 + e^{-iqd}), && (4.28)\\ &= f(q)^2(2 + e^{iqd} + e^{-iqd}), && (4.29)\\ &= 2f(q)^2(1 + \cos qd). && (4.30) \end{aligned}$$

The result from Hang Shi is calculated per graphene layer and thus we must divide our result by 2 layers. The effects of powder averaging that leads to the leading $1/q^2$ term in all of Hang Shi's results must also be included and thus we get

$$\frac{f(q)^2(1 + \cos qd)}{q^2}, \tag{4.31}$$

which is precisely equivalent to the result of Hang Shi. Similarly, we can include an extra term for the third layer,

$$\begin{aligned} S(q) &= f(q) * (1 + e^{iqd} + e^{2iqd}), && (4.32)\\ I(q) &= S^*S = f(q)^2 * (1 + e^{iqd} + e^{2iqd})(1 + e^{-iqd} + e^{-2iqd}), && (4.33)\\ &= f(q)^2(3 + 4\cos qd + 2\cos 2qd). && (4.34) \end{aligned}$$

Again we must divide by the number of layers and add the $1/q^2$ term to compensate for powder averaging which gives

$$\frac{f(q)^2(1 + \frac{4}{3}\cos qd + \frac{2}{3}\cos 2qd)}{q^2}. \tag{4.35}$$

This is also equivalent to the result of Hang Shi.

4.1.9 Fitting of the Data

To fit the WAXS curve we assume the measured scattering pattern can be approximated by a linear superposition of the intensities calculated for the 002 peak for single, double and triple layers. The main difficulty with this theory is that we do not include interferences between randomly oriented groups of layers. This is more

d_{002} (Å)	single (%)	double (%)	triple (%)
3.4	40	59	1
3.5	40	52	8
3.6	41	43	15
3.7	43	34	22
3.8	45	29	27

Table 4.2: The fractions of single, double and triple layers determined by the fitting algorithm that best fits the measure WAXS pattern for sucrose pyrolysed to 1050°C.

likely to contribute to small-angle deviation, as randomly aligned layers will be further than d_{002} apart, and for this reason we do not attempt to fit WAXS data to scattering angles lower than 15^o.

Figure 4.9 shows the calculated intensity for single, double and triple layers. In the fourth panel we have combined 50% single, 30% double and 20% triple layers and this ratio seems to resemble the measured data shown in the last panel quite well.

The next step is to fit the data using a linear superposition of these intensities calculated for single, double and triple layers together with a background constant. The fitting procedure minimizes the deviation between the calculated and measured intensity using a χ^2 fitting algorithm. The fitting procedure determines the best values for the fractions of single, double and triple layers to fit the measured WAXS pattern for sucrose pyrolysed to 1050°C. The fitting function also contains a fitting parameter for the background. The purpose of this exercise is to understand how changes in the d_{002} spacing effect the goodness of fit. The results are shown in figure 4.10 and the corresponding fractions of single, double and triple layers is tabulated in table 4.2. By inspection, the best fit occurs between 3.6 and 3.7 Å, however, due to the rather simple nature of this fitting procedure, more precise estimates for d_{002} are unjustified.

In figure 4.11, the dependence of the peak shape and position has been calculated for different combinations of layers. As the number of stacked layers increases the 002

peak becomes more pronounced. In fact, the 002 peak intensity is a direct measure of the number aligned graphene sheets in the c-axis direction [43]. It seems obvious that we should define an empirical parameter "R" as the 002 peak height to background ratio to exploit this relation (see figure 4.11, panel 3 for a graphical description). Higher R values are indicative of more stacked layers. Using this parameter we will compare the degree of "layer stacking" in different hard carbons in later chapters.

4.2 Small Angle X-ray Scattering

Small angle X-ray scattering measurements are used to determine the length scale for electron density fluctuations in materials. In hard carbon, these fluctuations are the result of voids created in the space between mis-aligned graphene layers and these voids are called nanopores because they are only 5-10 Å in radius.

4.2.1 Theory of SAXS

Let us consider a micropore embedded in a carbonaceous material. Equation (4.12) allows for the calculation of the intensity scattered from such an object. The micropores can be modeled as a change in electron density with respect to a constant background. Assuming an isotropic form factor for the background and converting the sum in equation 4.12 to an integral, we get the following equation for small-angle scattering [54]:

$$S(\mathbf{q}) = \int d^3\mathbf{r}\rho(\mathbf{r})e^{-i\mathbf{q}\cdot\mathbf{r}}, \tag{4.36}$$

where $\mathbf{q}$ is the scattering vector and ρ is the electron density.

In order to simplify the geometry of the problem, we will consider the micropores to be spherically symmetric and we will align the scattering vector $\mathbf{q}$ along the $\hat{\mathbf{z}}$ axis as shown in figure 4.12. The micropore has a 'hard' radius R_0 and the electron density change between the micropore and the background is ρ_0. This greatly simplifies the

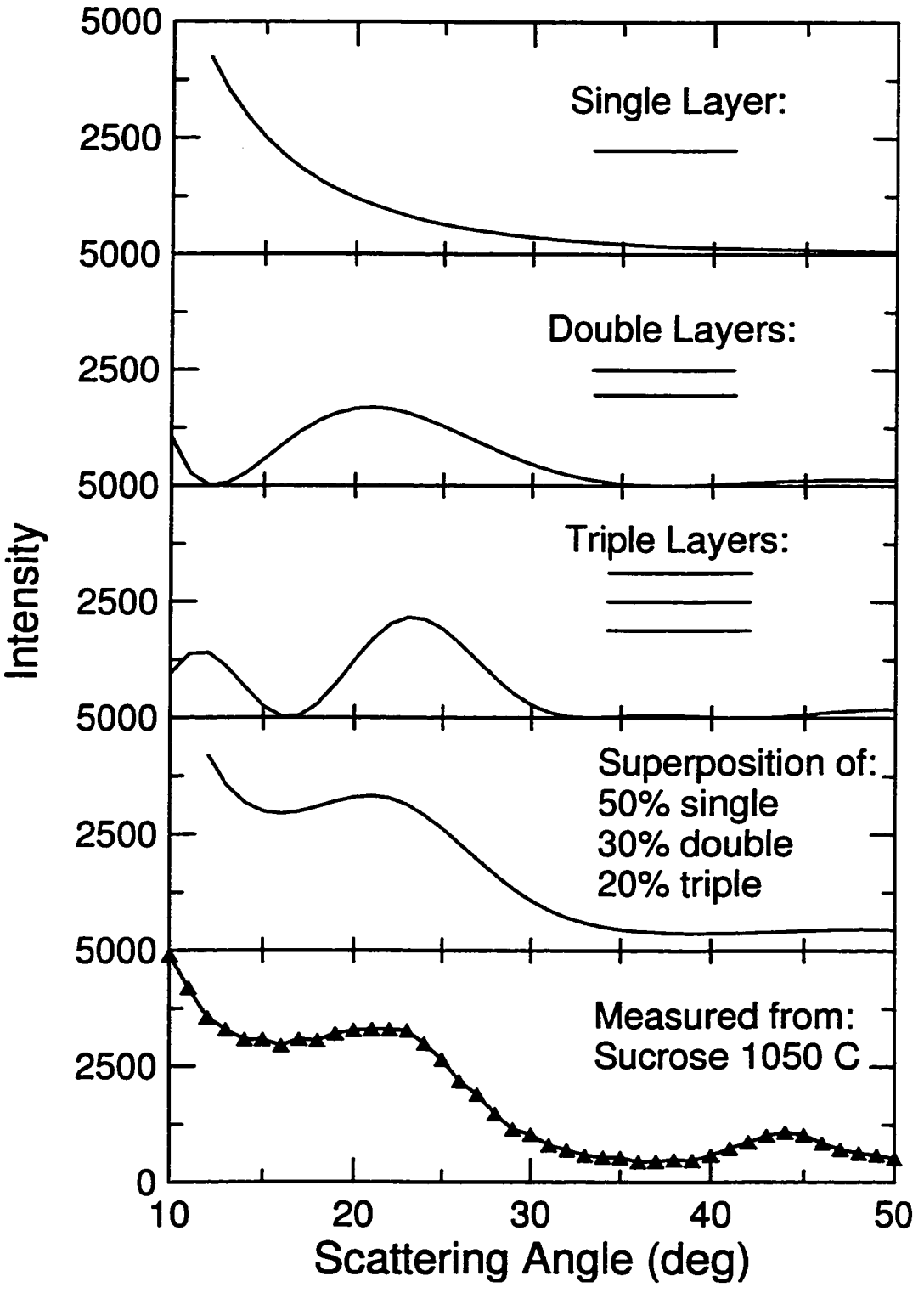

Figure 4.9: Calculated scattered X-ray intensity for single, double and triple layers. A superposition of 50% single, 30% double and 20% triple layers produces an X-ray diffraction pattern that closely resembles the measured intensity for hard carbon prepared by pyrolysis of sucrose to 1050°C.

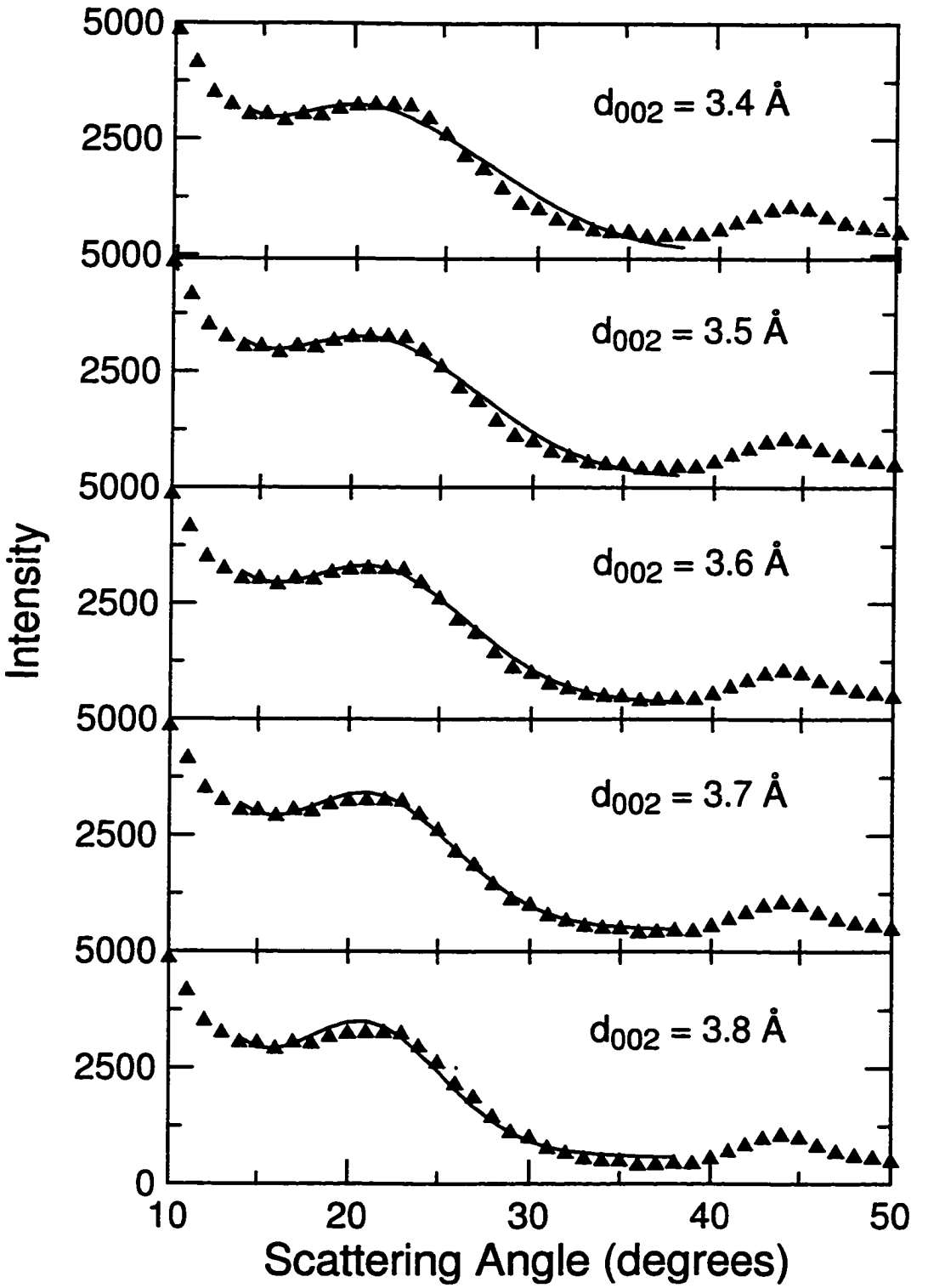

Figure 4.10: The calculated scattered X-ray intensity for various values of the d_{002} spacing. The calculated curves are superimposed on the measured pattern for sucrose pyrolysed to 1050°C.

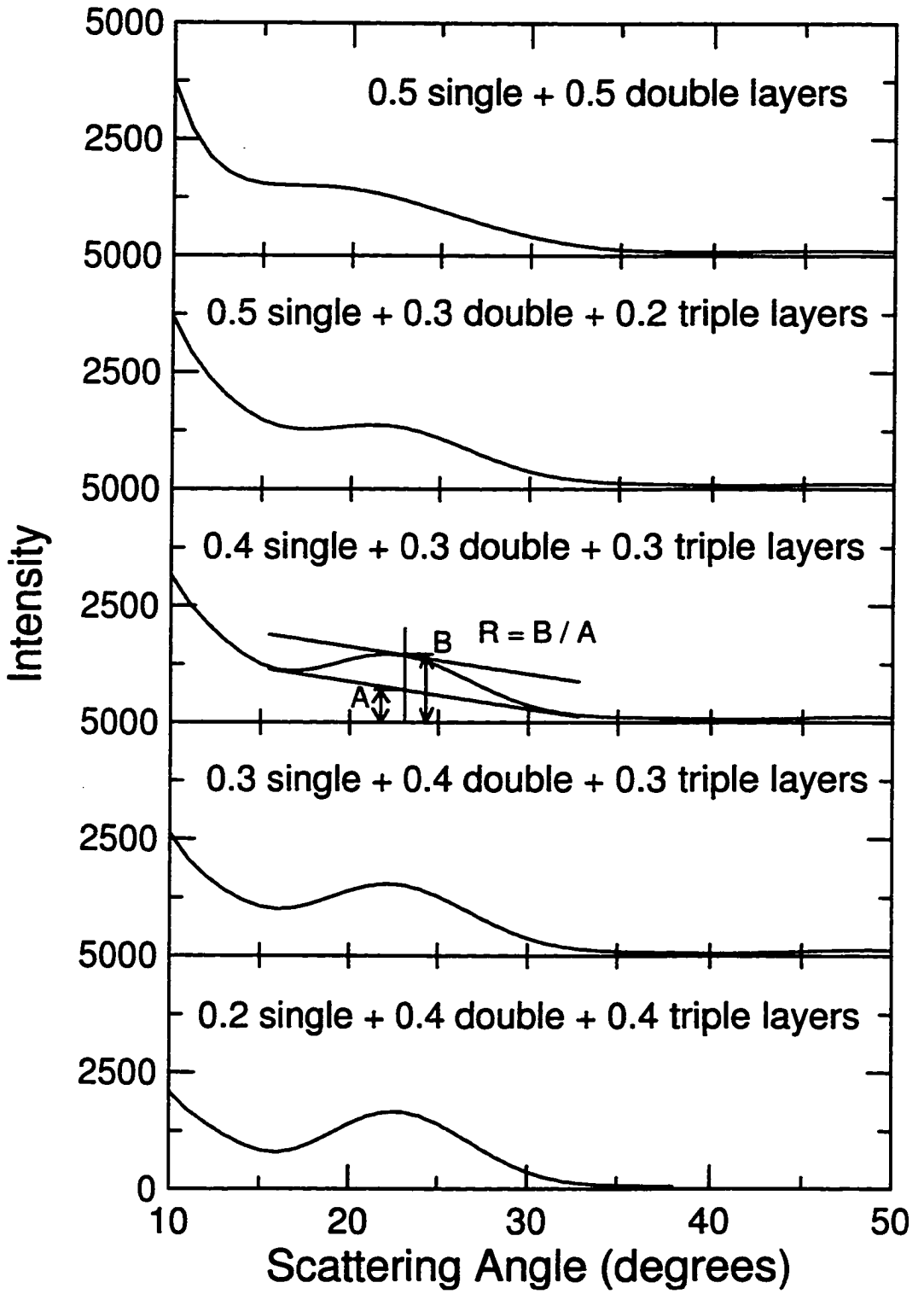

Figure 4.11: Dependence of the empirical parameter R on the ratio of single, double and triple layers used to calculate the intensity of scattered X-rays. The d_{002} spacing is fixed at 3.6Å.

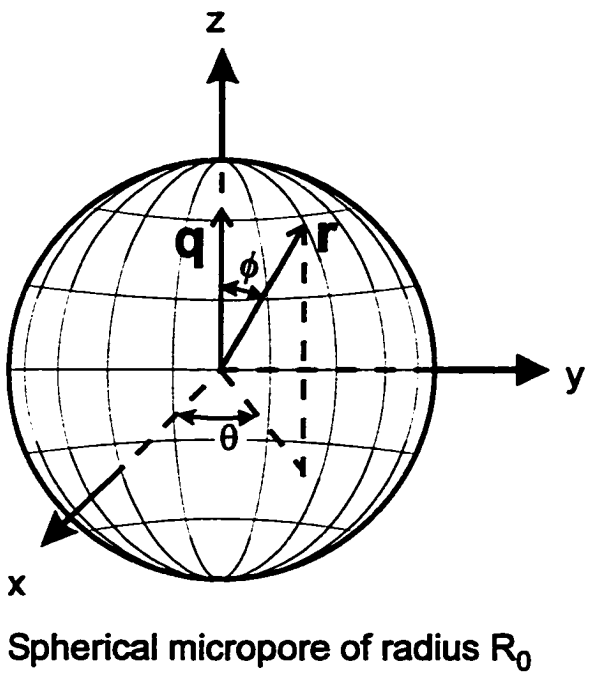

Figure 4.12: Model of a spherical micropore of radius R_0. The scattering vector $\mathbf{q}$ has been aligned with the $\hat{\mathbf{z}}$ axis for convenience.

problem and leads to the following equation for the amplitude of the scattered wave:

$$S(\mathbf{q}) = \int d^3\mathbf{r}\rho_0 e^{-iqr\cos\phi}. \tag{4.37}$$

$$= 2\pi\rho_0 \int_0^{R_0} r^2 dr \int_0^{\pi} \sin\phi d\phi e^{iqr\cos\phi} \tag{4.38}$$

$$= 2\pi\rho_0 \int_0^{R_0} r^2 dr \int_{-1}^{1} d\cos\phi e^{iqr\cos\phi} \tag{4.39}$$

$$= 2\pi\rho_0 \int_0^{R_0} r^2 dr \Big(\frac{e^{iqr} - e^{-iqr}}{iqr}\Big) \tag{4.40}$$

$$= 4\pi\rho_0 \int_0^{R_0} r dr \frac{sin(qr)}{r} \tag{4.41}$$

$$= 3V\rho_0 \Big(\frac{\sin(qR_0) - qR_0\cos(qR_0)}{(qR_0)^3}\Big) \tag{4.42}$$

where V is the volume of the spherical micropore. The measured intensity is calculated from this result:

$$I(q) = S(q)^* S(q) = 9(\rho_0 V)^2 \Big(\frac{\sin(qR_0) - qR_0\cos(qR_0)}{(qR_0)^3}\Big)^2. \tag{4.43}$$

This result was first calculated by Raleigh in 1911[55].

In the limit of $qR_0 << 1$, the intensity can be approximated by the Guinier equation [56]. The Taylor expansion to terms of $O(qR_0)^2$ of equation 4.43 is equivalent to the Taylor expansion of the Guinier equation:

$$I(q) = (\rho_0 V)^2 e^{-q^2 R_g^2/3} \tag{4.44}$$

provided $R_g = \sqrt{\frac{3}{5}}R_0$. In fact, R_g is defined as the radius of gyration for electrons which is precisely equivalent to $\sqrt{\frac{3}{5}}R_0$ for a micropore of spherical geometry.

In the limit where $qR_0 >> 1$, the contribution of the sin term in equation 4.43 can be neglected and a rapidly varying cos approximation can be used to approximate the intensity,

$$I(q) \approx \frac{2\pi S\rho^2}{q^4}, \tag{4.45}$$

where S is the surface area of the interface between the solids and the pores. This is the well known Porod's law [57].

Debye et al. [58] improved the model of a two-phase system by assuming the electron density at the interface did not change abruptly. They showed that the electron density ρr should be replaced by the autocorrelation function $\gamma(r) = e^{-r/a}$, where a is the Debye correlation length. They further showed that such a substitution leads to the following result for the measured intensity of X-rays:

$$I(q) = \frac{2\pi S\rho^2}{(\frac{1}{a^2} + q^2)^2}. \tag{4.46}$$

A comparison of the Taylor expansion of this result and the Guinier equation shows that a can be related to R_g by the relation $R_g = \sqrt{6}a$. The noted distinction in this derivation is that R_0 and R_g were defined for single pores whereas a applies to a random two-phase system in which the pores are of course not uniform in both size and shape.

The measured SAXS curves were fitted to the following equation as explained in the paper by Gibaud et al. [59] and later by Zheng et al[60] for hard carbons prepared from coal,

$$I(q) = \frac{A}{q^4} + \frac{B}{(\frac{6}{R_g^2} + q^2)^2} + C \tag{4.47}$$

where A, B, and C are constants, q is the scattering vector and R_g is the radius of gyration for electrons. This equation may contain the contribution from a single pore size distribution defined by the Debye correlation length a and corrects for Porod behaviour at low q and a constant background term C.

4.2.2 Sample Preparation and Experimental Methods

The SAXS data was collected using the same Siemens D5000 diffractometer used to measure the WAXS patterns. The diffractometer is generally used in the reflection geometry, however for SAXS measurements the samples are mounted vertically in the X-ray transmission mode. The samples were filled into a rectangular frame with

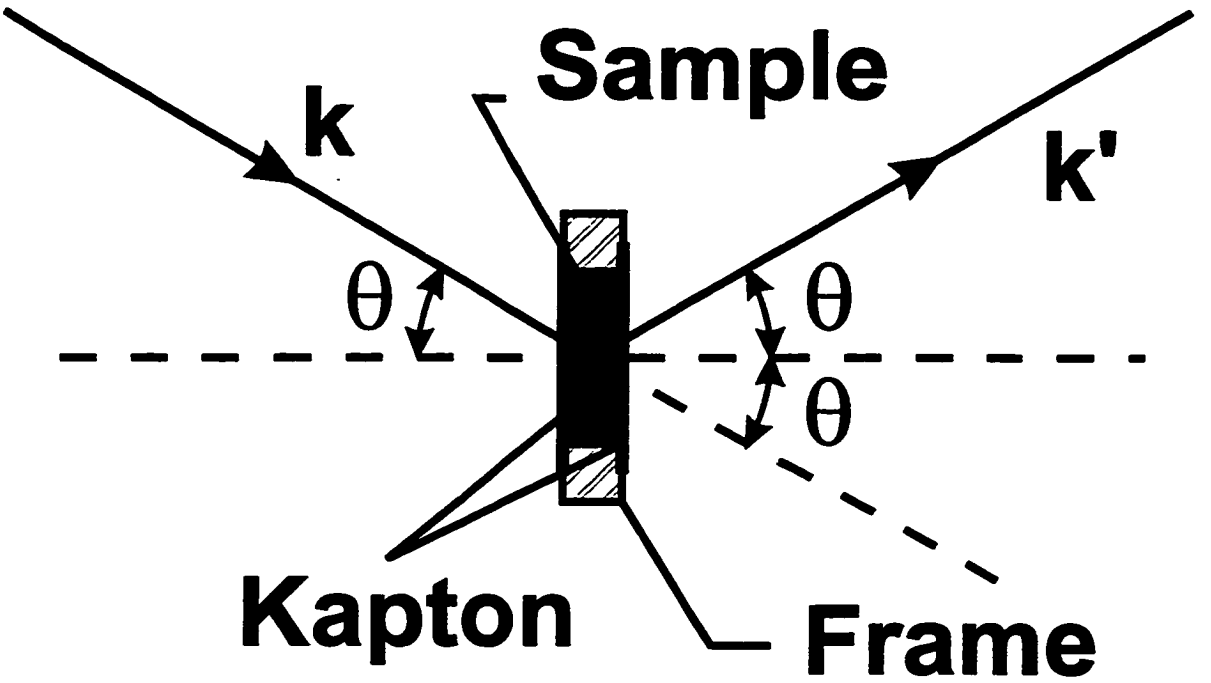

Figure 4.13: Schematic diagram of the sample holder used to hold materials in the vertical plane for transmission SAXS experiments. The direction of the incident and scattered waves are shown.

kapton (fluorinated polyamide) on both sides of the well to allow the sample to be mounted vertically as shown in figure 4.13. The incident and antiscatter slits were both 0.1^o and the receiving slit was 0.1 mm. The empty frame with kapton windows showed negligible intensity when compared with the intensity produced when filled with a sample. The background effect of the kapton was therefore neglected in the analysis of the measured data. The mass of the sample and the attenuation of the beam were recorded so that the measured intensity could be corrected for beam attenuation as explained in [60].

4.2.3 Verification of SAXS Results

In figure 4.14, a typical SAXS curve for a sucrose sample pyrolysed to 1050°C is compared to that of a common graphitic material. The first term in equation 2 is Porod's Law and that states the intensity should fall off like $1/q^4$ for small q values. Both samples contain this contribution. The second term in equation 2 contains the length scale for electron density fluctuations R_g that are caused by the nanopores. The graphitic sample shown in figure 5 does not contain nanopores and the resulting fit contains only the Porod's Law contribution (B = 0) as one might expect. Since both samples have the same chemistry, any differences between their measured SAXS profiles must result from the nanopores in the hard carbon. Including the second term in (4.47) when fitting the SAXS data for the hard carbon indicates $R_g = 7.8$ Å. Assuming a spherical nanopore geometry, this corresponds to a nanopore radius of about 10 Å. By observation, the fits for both the graphitic and hard carbon materials are quite good. This technique of measuring the average nanopore diameter will by used to compare the nanopores in different hard carbons pyrolysed to different heat treatment temperatures.

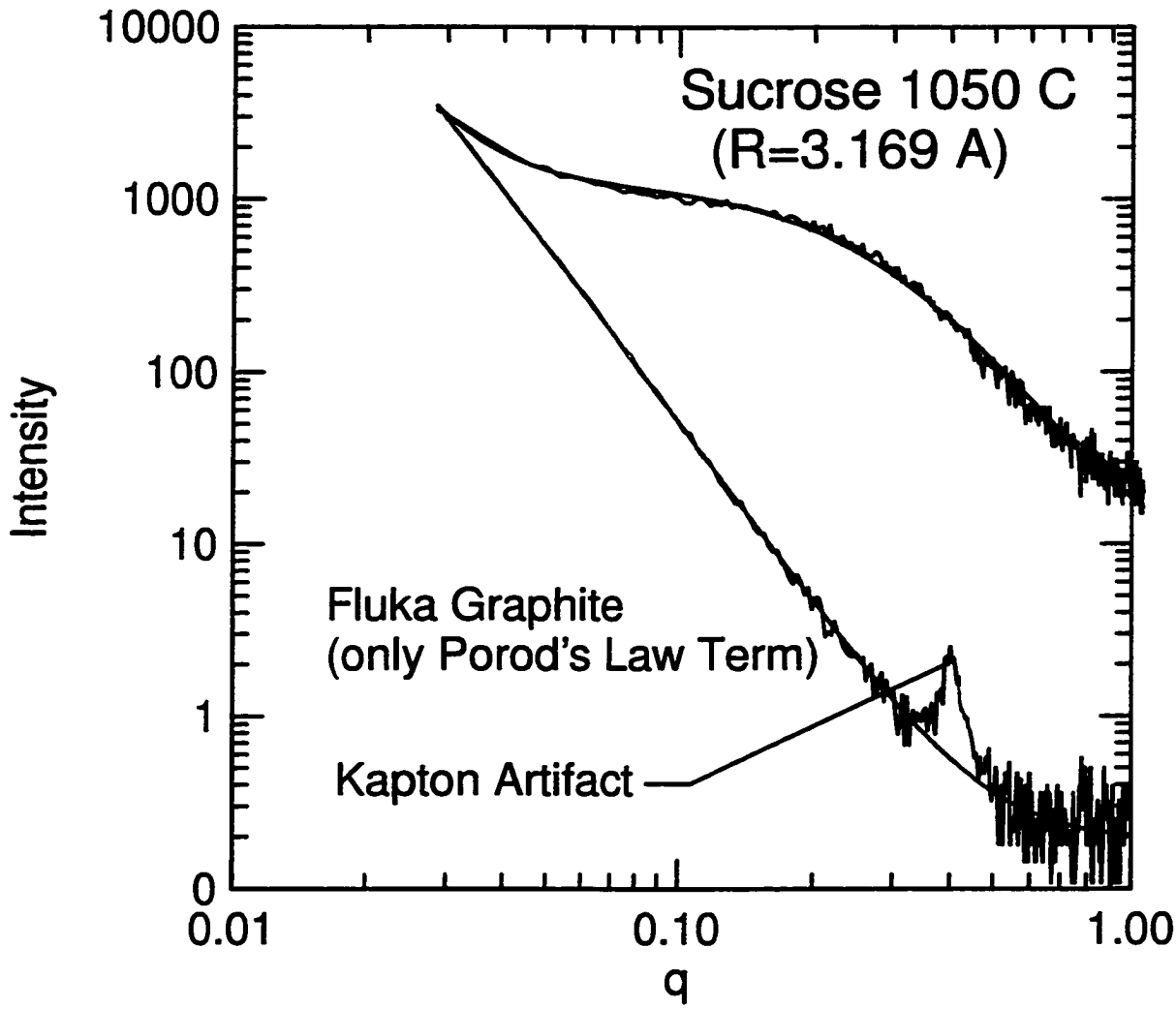

Figure 4.14: Comparison of the measured and calculated SAXS curves for hard carbon prepared for sucrose pyrolysed at 1050°C and Fluka graphite; a sample with no microporous structure but similar chemistry.

4.3 BET Surface Area Measurements

Single-point BET surface area measurements were made using a Micromeritics Flowsorb II 2300 surface area analyser. A gas mixture of 30% N_2 to 70% He (molar ratio) was used with impurity levels reduced using an in-line cold trap. About 150 mg of sample was placed in a glass sample holder and degassed at 200°C for at least two hours prior to the BET measurements. The adsorption of N_2 on the surface of the carbon sample required 2 to 3 hours to achieve equilibrium. Desorption was initiated by immersion of the sample in water at room temperature. The reported BET surface areas are all measured by desorption and are reproducible within ± 5%.

4.3.1 Theory of single point gas adsorption

One form of the well-known BET equation [61] that describes the adsorption of a gas on a solid is

$$\frac{V}{V_M} = \frac{C\frac{P}{P_0}}{\left(1+(C-1)\frac{P}{P_0}\right)\left(1-\frac{P}{P_0}\right)} \tag{4.48}$$

where V is the volume (at STP) of gas adsorbed at pressure P, P_0 the saturation pressure (also the vapour pressure of the liquefied gas at the adsorbing temperature), V_M is the volume of gas (STP) required to form a monolayer on the surface of the sample and C is a constant related to the energy of adsorption.

The constant C is usually a relatively large number, i.e., $C >> 1$ for which equation 4.48 reduces to:

$$\frac{V}{V_M} = \frac{\frac{P}{P_0}}{\left(\frac{1}{C}+\frac{P}{P_0}\right)\left(1-\frac{P}{P_0}\right)}. \tag{4.49}$$

The partial pressure of the adsorbent is usually ≈ 0.30 and thus assuming $\frac{P}{P_0} >> \frac{1}{C}$, equation 4.49 can be further reduced to:

$$V_M = V(1-\frac{P}{P_0}). \tag{4.50}$$

The surface area S of the sample giving a monolayer adsorbed gas volume V_M can then be calculated from:

$$S = \frac{V_M N_A A_m}{M} \tag{4.51}$$

where N_A is Avagadro's number, A_m is the area covered by one adsorbed molecule (i.e. 16.2×10^{-20} [62] m^2 for nitrogen at -195°C) and M is the molar volume of the gas at STP. Substituting equation 4.50 into 4.51 yields

$$S = \frac{V(1 - \frac{P}{P_0})N_A A_m}{M}. \tag{4.52}$$

For practical purposes, the volume of gas adsorbed, V, in equation 4.52 will be at room temperature and requires an additional factor of $\frac{273.2K}{Rm.Temp.}$. The gas mixture is 30% N_2/70% He and hence the partial pressure of N_2 is 0.30 since the adsorption occurs at atmospheric pressure (= saturation pressure). Thus assuming that adsorption takes place at standard pressure and the saturation pressure of the gas is atmospheric pressure, then equation 4.52 can be reduced to

$$S = V\left(\frac{273.2}{295.2}\right)\left(\frac{6.023 \times 10^{23} \cdot 16.2 \times 10^{-20}\mathrm{m}^2}{22.414 \times 10^3\mathrm{ml}}\right)(1 - 0.3) \tag{4.53}$$

$$= 2.82\frac{\mathrm{m}^2}{\mathrm{ml}}V. \tag{4.54}$$

For calibration purposes, a syringe injection of 1 ml of N_2 gas is calibrated to a surface area of 2.84 m^2.

4.3.2 Experimental

A schematic diagram of the surface area analyser is shown in figure 4.15. The matched thermal conductivity cells measure the difference in concentration of N_2 in the gas flow before and after the sample. Assuming a constant flow rate, this difference is integrated to determine the volume of N_2 being adsorbed or desorbed from the sample. The septum is used to introduce a fixed amount of N_2 gas which is used to calibrate the apparatus. The filter prevents sample particles from contaminating the system

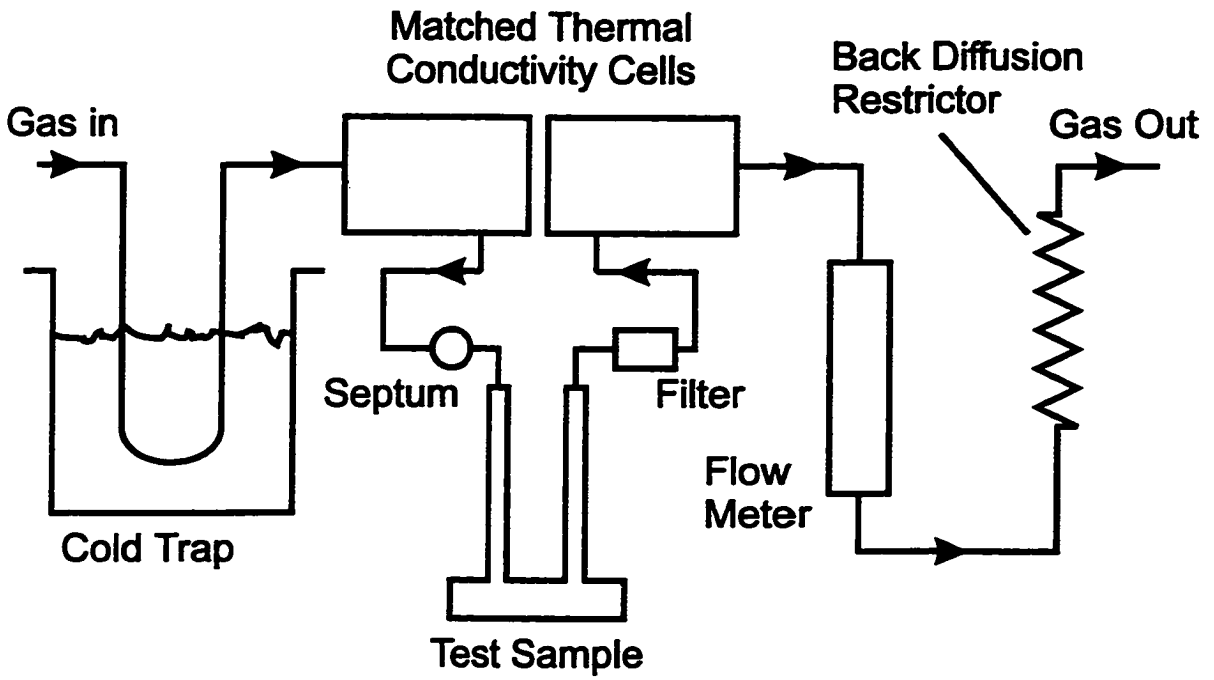

Figure 4.15: Schematic diagram of the Micromeritics Flowsorb II 2300 surface area analyser .

and the cold trap acts to reduce any impurities that might be present in the gas mixture. The flow meter is used to ensure a desired flow rate and the back diffusion restrictor acts to reduces changes in the flow rate due to changes in back pressure.

Chapter 5

CO_2 Gas Adsorption Experiments

The large capacity at low voltage (sometimes called the low voltage plateau) is what makes hard carbon a desirable anode material. Although the exact mechanism is not fully understood, the microporous structure is intimately connected to this large capacity and CO_2 gas adsorption experiments will show that when the micropores close, this capacity is lost. This chapter focuses on the theory of gas adsorption and the construction of a gas adsorption analyser designed specifically for hard carbon. The correlation of micropores and the low voltage plateau is discussed in chapter 6.

5.1 Gas Adsorption Theory

Before the apparatus is described, the BET and Langmuir models of gas adsorption will be explained. Hard carbon materials are microporous and do not exhibit smooth, uninhibited surfaces and a simple single layer adsorption model, the Langmuir equation, seems to explain the observed results quite well. The classical derivation of the celebrated BET equation [61] for multi-layer adsorption will be derived and then simplified to the Langmuir model. The later is shown to be consistent with a statistical mechanics model of independent adsorption sites and a single binding energy and gives more meaning to the constants found in the classical derivation.

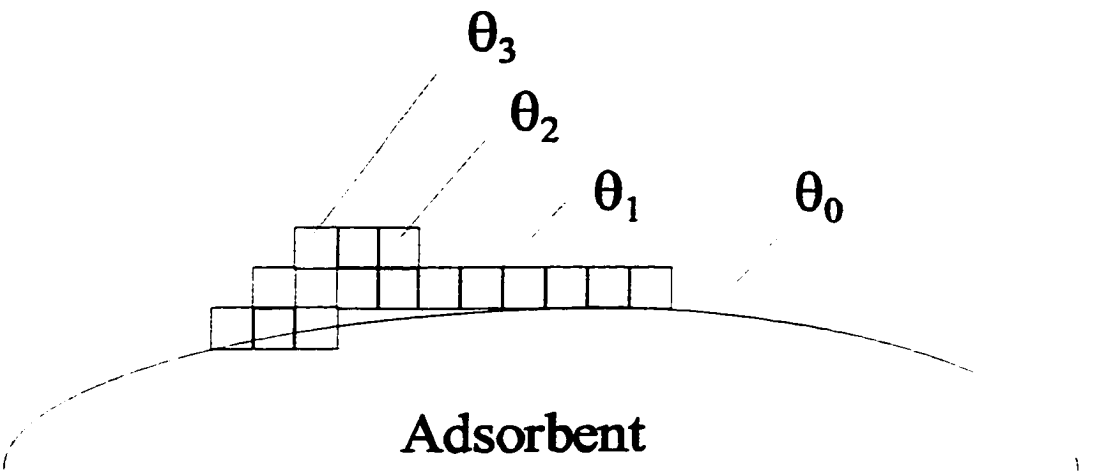

Figure 5.1: The adsorption sites form an array of layers where θ_i is the fraction of the surface covered by exactly i layers.

5.1.1 The BET Equation

The BET treatment of gas adsorption models the surface as an array of layered adsorption sites. The fraction of the surface occupied by N molecules is given by θ_N where θ_0 gives the fraction of bare sites, θ_1 the fraction of sites covered with one and only one molecule, θ_2 by two and only two and so on (see figure 5.1.) The number of molecules(N) adsorbed onto the surface is thus related to the total number of surface sites N_s by the equation

$$N = (\theta_1 + 2\theta_2 + 3\theta_3 + \ldots + i\theta_i + \ldots)N_s. \tag{5.1}$$

The sum of the surface coverage fractions must be normalized

$$\sum_i^{\infty} \theta_i = 1. \tag{5.2}$$

A dynamic balance between the rate of adsorption and desorption leads to a recursion relation in the variables θ_i. Langmuir[63] was the first to develop a one layer model where the rate of condensation on the bare sites was equal to the rate of evaporation of the occupied sites in dynamic equilibrium. The BET[61] equation generalizes

the Langmuir model by allowing multiple-layer adsorption where gas molecules adsorbed onto the surface may serve as adsorption sites for others. Brunauer, Emmett and Teller distinguished the adsorption dynamics for the first layer (adsorbate onto adsorbent) from the second and higher layers (adsorbate onto adsorbate) but assumed that these layers shared the same adsorption and desorption dynamics.

The number of molecules arriving per second from the gas phase, per unit area of freely exposed surface, is given by the kinetic theory of gases[64] as

$$\frac{p}{\sqrt{2\pi M k_B T}}$$

where p is the pressure, M the mass and T the temperature of the gas surrounding the sample. If θ_0 is the fraction of bare sites on the surface then the rate of condensation n_1 in the first layer will be

$$\frac{dn_1}{dt} = \frac{pa_1\theta_0}{\sqrt{2\pi M k_B T}}$$

the factor a_1 (the "condensation coefficient") is introduced to allow for the possibility of a molecule incident on the surface not being adsorbed. In generalizing this result, the rate of adsorption into any layer, say the i^{th} layer, is proportional to the pressure of the gas (p) and the number of available sites θ_{i-1}

$$\frac{dn_i}{dt} = \alpha_i p\theta_{i-1} \tag{5.3}$$

where α_i, for all intents and purposes, is simply a constant that has units of $(pressure)^{-1}(time)^{-1}$ and is equal to

$$\alpha_i = \frac{Na_i}{\sqrt{2\pi M k_B T}}.$$

Next we must consider the rate of desorption from the first layer. Let ν_1 be the frequency of oscillation of adsorbed molecules in a direction normal to the surface; then the probability that a molecule will evaporate when it reaches the apex of vibration will be governed by Boltzmann statistics. The number of desorption events for an occupied site on the first layer will be

$$\nu_1 e^{-E_1/k_B T}$$

where E_1 is the energy of activation of desorption and k_B is Boltzmann's constant. Since the number of adsorption sites in the first layer is $\theta_1 N_s$ (remember N_s is the number of molecules that would adsorb in a complete monolayer), the rate of desorption from the first layer is

$$\frac{dn_1'}{dt} = N_s \theta_1 \nu_1 e^{-E_1/k_B T}.$$

Again we can collect the constants into a single constant β_i and generalize the rate of desorption to any given layer, that is

$$\frac{dn_i'}{dt} = \beta_i \theta_i \tag{5.4}$$

where β_i is

$$\beta_i = N_s \nu_i e^{-E_i/k_B T}.$$

Balancing the rate of adsorption/desorption, equations 5.3 and 5.4, for any given layer gives

$$\theta_i = \left(\frac{\alpha_i}{\beta_i} p\right) \theta_{i-1}. \tag{5.5}$$

The BET equation assumes that the first layer of adsorption (of gas molecules onto the substrate) is distinct from all other layers (gas molecules onto adsorbed gas molecules). These higher layers are also assumed to be equivalent, i.e. the first layer effectively screens out any interaction of the surface with higher layers. This is equivalent to letting

$$\frac{\alpha_2}{\beta_2} = \frac{\alpha_3}{\beta_3} = \frac{\alpha_4}{\beta_4} = \frac{\alpha_5}{\beta_5} = \ldots$$

Therefore, for the first layer we get

$$\theta_1 = \left(\frac{\alpha_1}{\beta_1} p\right) \theta_0 \tag{5.6}$$

for the second layer we get

$$\theta_2 = \left(\frac{\alpha_2}{\beta_2} p\right) \theta_1$$

for the third layer we get

$$\theta_3 = \left(\frac{\alpha_2}{\beta_2}p\right)\theta_2$$

and since we can substitute in the previous result for θ_2 we also get

$$\theta_3 = \left(\frac{\alpha_2}{\beta_2}p\right)^2\theta_1.$$

In fact we can define a recursion relation that relates all of the fractions of occupied sites to that of the first layer

$$\theta_i = \left(\frac{\alpha_2}{\beta_2}p\right)^{i-1}\theta_1. \tag{5.7}$$

Expressions 5.7 can be used to reduce equation 5.1 to contain only the single layer occupation fraction θ_1

$$n = \frac{N}{N_s} = \theta_1\left[1 + 2\left(\frac{\alpha_2}{\beta_2}p\right) + 3\left(\frac{\alpha_2}{\beta_2}p\right)^2 + \ldots\right] \tag{5.8}$$

If we assume that the number of molecules in successive layers decreases then

$$\left(\frac{\alpha_2}{\beta_2}p\right) < 1$$

and then equation 5.8 is a convergent arithmetic-geometric series that can be evaluated giving the following result

$$n = \frac{\theta_1}{\left(1 - \frac{\alpha_2}{\beta_2}p\right)^2}. \tag{5.9}$$

Similarly, equation 5.2 contains a geometric series that converges, i.e.

$$\theta_0 + \theta_1 + \theta_2 + \theta_3 + \ldots = 1.$$

Next we need to eliminate all the $\theta_i's$ in terms of θ_1 and this is accomplished using equation 5.6 for θ_0 and 5.7 for all others to get

$$\theta_1\left[\left(\frac{\beta_1}{\alpha_1}p\right) + 1 + \left(\frac{\alpha_2}{\beta_2}p\right) + \left(\frac{\alpha_2}{\beta_2}p\right)^2 + \ldots\right].$$

The geometric series is evaluated to get

$$1 + \left(\frac{\alpha_2}{\beta_2}p\right) + \left(\frac{\alpha_2}{\beta_2}p\right)^2 + \ldots = \frac{1}{1 - \frac{\alpha_2 p}{\beta_2}}$$

and hence we get:

$$\theta_1 \left[\frac{\beta_1}{\alpha_1}p + \frac{1}{1 - \frac{\alpha_2}{\beta_2}p}\right] = 1 \tag{5.10}$$

Next we solve equations 5.9 and 5.10 for θ_1, equate the results and solve for n to get

$$n = \frac{\frac{\alpha_1}{\beta_1}p}{\left(1 - \frac{\alpha_2}{\beta_2}p + \frac{\alpha_1}{\beta_1}p\right)\left(1 - \frac{\alpha_2}{\beta_2}p\right)}. \tag{5.11}$$

This is easily reduced to the familiar BET equation [61] if we define $p_0 \equiv \frac{\beta_2}{\alpha_2}$ and $c/p_0 \equiv \frac{\alpha_1}{\beta_1}$

$$n = \frac{c\frac{p}{p_0}}{\left(1 + (c-1)\frac{p}{p_0}\right)\left(1 - \frac{p}{p_0}\right)}. \tag{5.12}$$

In practice c is nearly always taken to be much greater than 1; i.e.

$$c = \frac{\alpha_1 \beta_2 e^{(E_1 - E_2)/k_B T}}{\alpha_2 \beta_1} \gg 1.$$

Brunauer, Emmett and Teller also made the further distinction that E_2 is the latent heat of condensation; although it does add to the understanding of the result it does not affect the utility in any way.

5.1.2 The Langmuir Equation

The BET model breaks down for a microporous surfaces because multi-layer adsorption simply cannot occur given the physical constrictions that exist inside the micropores. In this case we can simplify the problem by assuming that the majority of adsorption occurs in a single layer. This greatly simplifies the infinite series in

equations 5.1 and 2. Hence for equation 5.1 we get $\frac{N}{N_s} = n = \theta_1$ and for 5.2 we get $\theta_0 + \theta_1 = 1$. Similar to the BET derivation, we use equation 5.6 to eliminate θ_0, solve the two equation for θ_1, equate the results and solve for n to get the familiar Langmuir equation:

$$n = \frac{\frac{\alpha_1}{\beta_1} p}{\frac{\alpha_1}{\beta_1} p + 1} = \frac{c\left(\frac{p}{p_0}\right)}{c\left(\frac{p}{p_0}\right) + 1}. \tag{5.13}$$

where we have chosen $c/p_0 = \frac{\alpha_1}{\beta_1}$.

If we plot equation 5.13 vs. partial pressure (p/p_0) we can see the structure dictated by the constant c (see figure 5.2).

5.1.3 Statistical Mechanics Derivation of the Langmuir Equation

The most simple statistical mechanics model consists of a lattice of N_0 identical and independent adsorption sites that can either be unoccupied (energy = 0) or occupied (energy = $-\epsilon_0$). At any given time let N be the number of occupied sites and $n = N/N_0$ be the probability of any site being occupied by an adsorbed gas molecule. Proceeding in the usual statistical mechanics fashion, the Helmholtz free energy is defined as: A = E - TS. The entropy S is defined as $\mathrm{Tr}\rho \ln \rho$ where ρ is the density matrix of states. The two possible states are occupied or unoccupied and so we can write the Helmholtz free energy as follows

$$A = -n\epsilon_0 + k_B T \left[n \ln n + (1-n) \ln (1-n)\right]. \tag{5.14}$$

The chemical potential can now be calculated

$$\mu = \frac{\partial A}{\partial n} = -\epsilon_0 - k_B T \ln \frac{n}{(1-n)}. \tag{5.15}$$

Gas adsorption consists of two systems, the gas molecules adsorbed onto the surface and the ideal gas surrounding the sample. In thermodynamic equilibrium, these

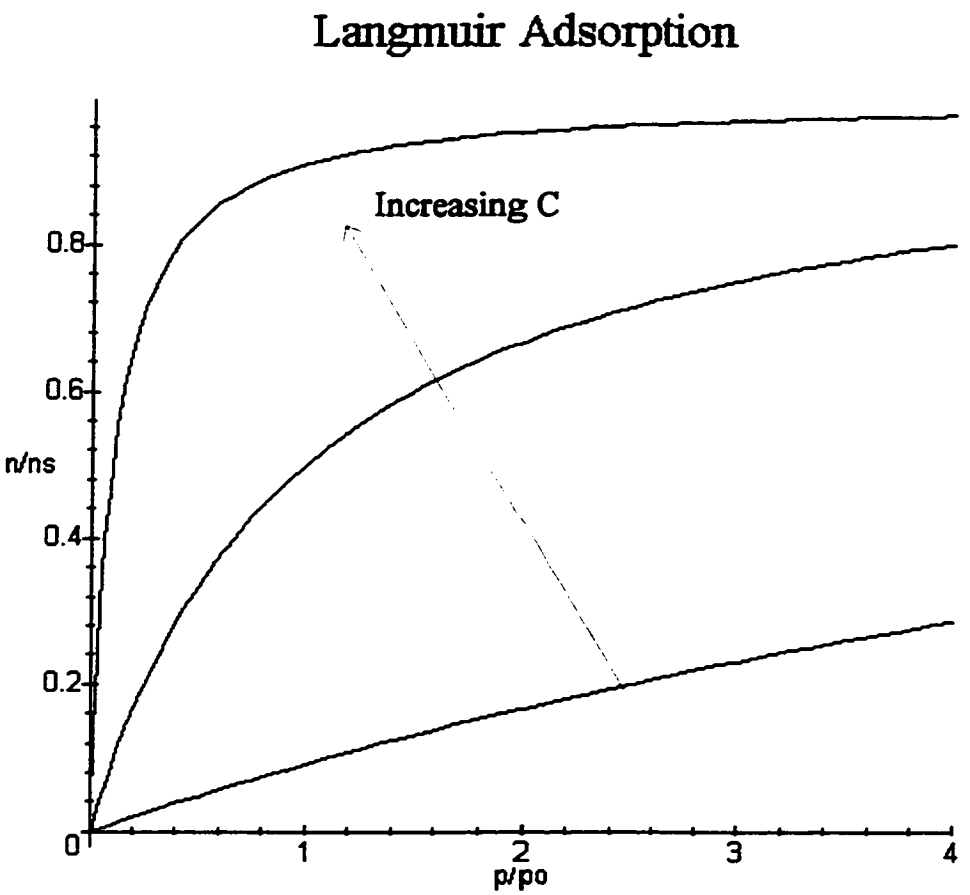

Figure 5.2: The effect of the parameter c on the shape of the Langmuir adsorption isotherm.

two systems must be at the same temperature and must have the same chemical potential which for an ideal gas is[65]

$$\mu_{[gas]} = k_B T \ln \frac{N_g \lambda^3}{V} \tag{5.16}$$

where λ is the thermal wavelength, V is the volume and N_g is the number of gas molecules in the gas phase.

Using the properties of the ideal gas law, the Langmuir equation is easily derived by equating equations 5.15 and 5.16. The result is identical to the classical derivation of the Langmuir equation (5.13) however new meaning is given to the constant c, i.e.

$$\frac{c}{p_0} = \lambda^3 \frac{e^{\frac{\epsilon_0}{k_B T}}}{k_B T} \tag{5.17}$$

5.1.4 Dubinin-Radushkevich Equation

The problem of micropores has been dealt with in a somewhat different manner by Dubinin [66] and his colleagues [67, 68]. It is based on the potential theory originally formulated by Polanyi in 1914 [69]. This theory relates the adsorption potential on the surface of the adsorbate ϵ to the pressure of the gas p through the relation

$$\frac{p}{p_0} = e^{-\frac{\epsilon}{RT}}, \tag{5.18}$$

where p_0 is the saturation vapour pressure of the adsorbate and $R = 8.31$ J mol^{-1} K^{-1}.

Dubinin and his co-workers argued that the volume of the adsorbed gas W could be expressed as a Gaussian function of the corresponding adsorption potential. This is written as

$$\frac{W}{W_0} = e^{-k(\frac{\epsilon}{\beta})^2} \tag{5.19}$$

where W_0 is the total pore volume, β is termed by Dubinin the *affinity coefficient* and k is a constant characterizing the pore size distribution. Substituting ϵ from equation

5.18 into 5.19 gives

$$\frac{W}{W_0} = \exp\left[-k\left(\frac{RT}{\beta}\right)^2\left(\ln\frac{p}{p_0}\right)^2\right], \tag{5.20}$$

the well known Dubinin and Radushkevich equation as described in its original form [70]. Equation 5.20 can be linearized, i.e.

$$\ln W = \ln W_0 - D\left(\ln\frac{p}{p_0}\right)^2, \tag{5.21}$$

where

$$D = k\left(\frac{RT}{\beta}\right)^2. \tag{5.22}$$

Thus a plot of $\ln W$ against $\ln\frac{p}{p_0}$ should give a straight line of slope D and intercept $\ln W_0$. Dubinin has plotted the results for adsorption isotherms of nitrogen, saturated hydrocarbons, benzene and cyclohexane in this manner and has found equation 5.22 to apply over the relative pressure range of 1×10^{-5} to 0.2 in the cases where the solid is microporous.

5.1.5 Dubinin-Astakhov Equation

The Dubinin-Astakhov equation [71] is essentially the same as equation 5.20 with the exponent 2 replaced by the Astakov exponent N,

$$\frac{W}{W_0} = \exp\left[-k\left(\frac{RT}{\beta}\right)^N\left(\ln\frac{p}{p_0}\right)^N\right]. \tag{5.23}$$

The Astakov exponent is now a variable and hence equation 5.23 cannot be linearized in the same fashion as equation 5.20. The value of the N must be optimized to give the best fit to the measured data. This is performed using a χ^2 fitting algorithm in an Excel 5.0 spreadsheet to determine the best value of the pore volume W_0.

5.1.6 BJH Pore Volume Distribution Calculation

Barrett, Johner and Halenda [72] developed the BJH method of determining the pore volume distribution based on the Kelvin [73] and Halsey [74] equations. Generally the desorption branch of the isotherm is used to relate the amount of adsorbate lost in a desorption step to the average size of pores emptied in that step.

A pore has two regions, the core and the adsorbed layer as shown in figure 5.3. A pore loses its condensed liquid adsorbate from the core at a particular relative pressure related to the core radius by the Kelvin equation. After the core has evaporated, a layer of adsorbate remains on the wall of the pore. The thickness of this layer is calculated, from the Halsey equation [74], for a particular relative pressure so that the measured quantity of gas desorbed in a step can be corrected for the remaining surface layer. This layer becomes thinner with successive decreases in pressure so that the measured quantity of gas desorbed in a step is comprised of both the thinning of the adsorbed layer on previously emptied pores as well as the emptying of new pores.

The Kelvin equation [73], developed in 1871, relates in thermodynamic terms the vapour pressure p of a liquid contained in a cylindrical capillary to its radius r. Assuming the liquid wets the walls of the pore, i.e. the contact angle is 0, a simplified form of the Kelvin equation is

$$r = -\frac{a}{ln(p/p_0)} \tag{5.24}$$

where $a = -\frac{2V\gamma}{RT}$, γ is the surface tension of the adsorbate in the pore, V the molar volume of the liquid, p_0 the saturation vapour pressure, $R = 8.31 Jmol^{-1}K^{-1}$ and T is the temperature.

The BJH pore volume distribution is most often calculated for nitrogen adsorption at 77 K. Typical values for a are 4.8 Å and 2.0 Å for nitrogen at 77 K and CO_2 at 273 K respectively [75]. For nitrogen at 77 K the saturation vapour pressure is atmospheric pressure and hence p/p_0 can range from 0 to 1. This allows for the characterization of pores from a few Å to many hundreds of Å. CO_2 on the other hand has a saturation vapour pressure of 34 atm at 273 K. Adsorption isotherms are typically measured by

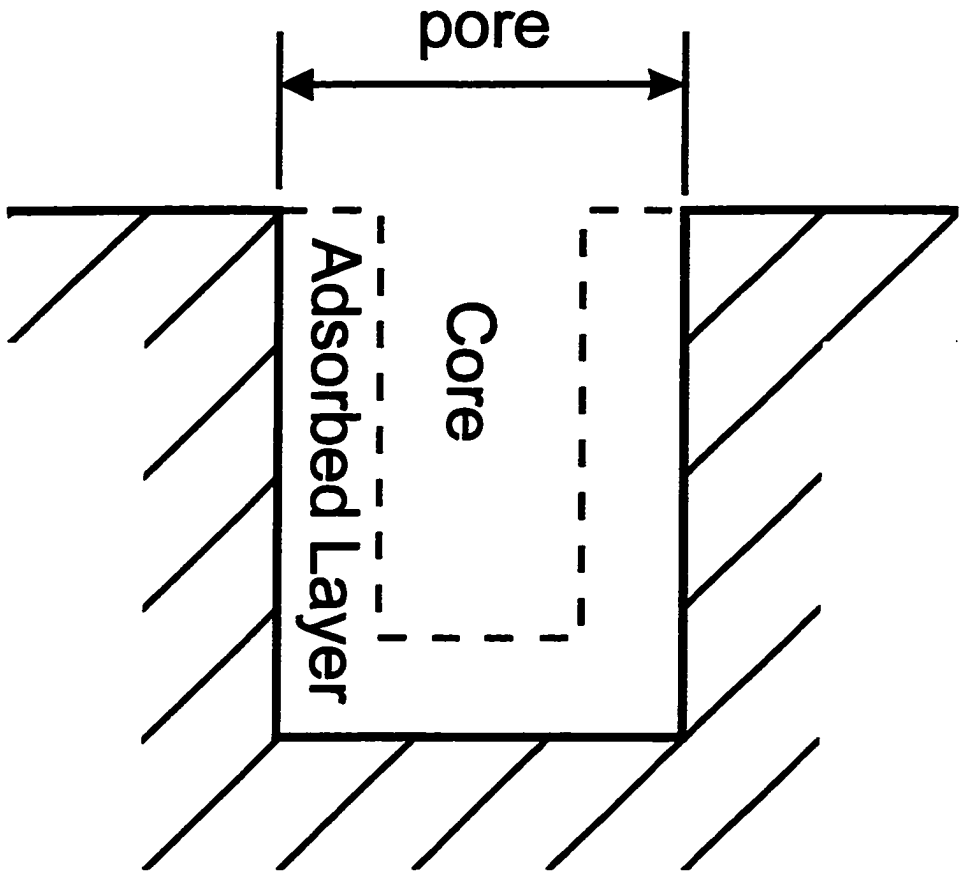

Figure 5.3: A pore filled with a condensed liquid has two zones: the core and the adsorbed layer.

our apparatus from $p/p_0 = 0$ to 0.03. The corresponding range of pore radii, calculated from the Kelvin equation, is from 0 to ~1.2 Å in diameter. This is a ridiculously small range of pore size, evidence for the breakdown of the Kelvin equation when only a small number of gas molecules fill a micropore, and effectively explains why the pore size distributions are not typically calculated when CO_2 is used. Consequently, pore size distributions were not calculated from the measured isotherms.

5.2 Gas Adsorption Apparatus

A prototype gas adsorption analyser was built specifically to measure the adsorption properties of hard carbons showing long rates of adsorption and large micropore volume. Hard carbon shows a dramatic decrease in CO_2 adsorption when heated to temperatures between 1100-1300°C. In this temperature range, the rate of adsorption decreases by an order of magnitude and determining when adsorption-desorption of the sample has reached equilibrium is critical in obtaining reproducible results. The description of the apparatus will begin with a much simplified model to explain the basic principles of operation and then complications/modifications to the design will be explained later.

5.2.1 Basic Operating Strategy

The basic operating strategy of the gas adsorption apparatus is to dose the sample with a fixed amount of gas and measure the amount of gas adsorbed vs. pressure. There are two common designs. The first is a gravimetric system that determines the amount of adsorption by measuring mass changes of the sample. This system is the simplest to implement however very sensitive balances are required that cost about $15, 000 and must be kept in a vibration free environment. The second system makes use of the ideal gas law and features two fixed volume chambers at different pressures, connected by a valve, and it is this type of apparatus that was constructed.

In the most simplistic form, the volumetric gas adsorption analyser is comprised

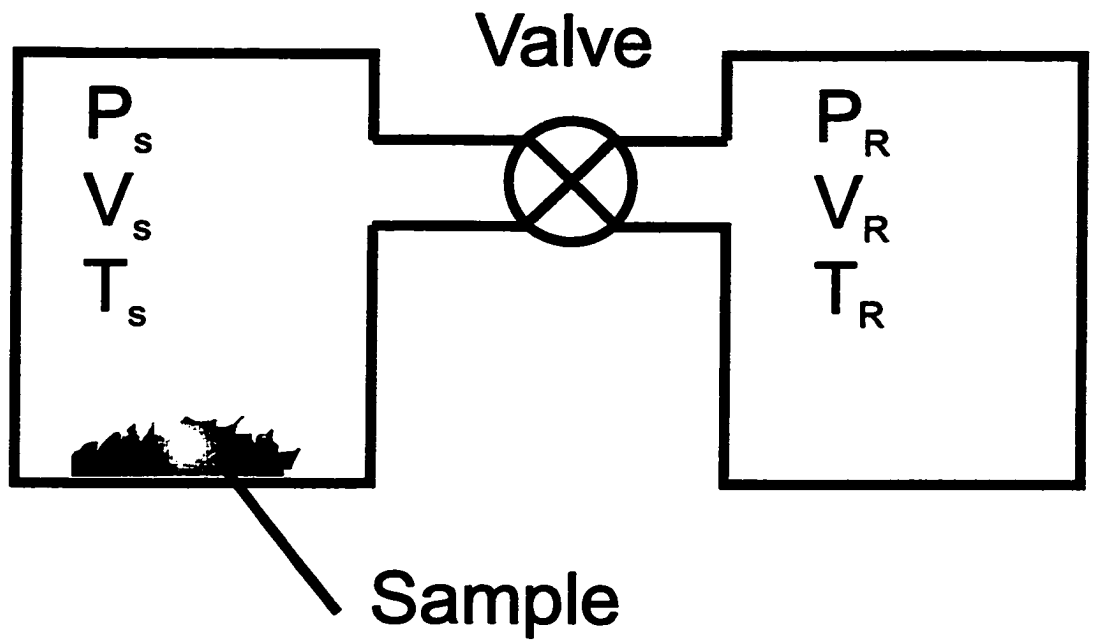

Figure 5.4: Schematic diagram of a simplistic volumetric gas adsorption analyser.

of a reservoir, a sample holder and a valve as shown in figure 5.4. Initially the sample is degassed under vacuum and high temperature to remove any adsorbed species from the surface (this is explained in section 5.4). With the reservoir filled and the pressure in the sample holder near 0 psia, the valve is opened to allow a small amount of gas to be transferred to the sample holder. The amount of gas transferred to the sample holder is calculated by applying the ideal gas law to the reservoir before (primed) and after (unprimed) the valve is opened;

$$\Delta N_R = \frac{P'_R V'_R}{T'_R k_B} - \frac{P_R V_R}{T_R k_B} \tag{5.25}$$

where P is the pressure, T is the temperature, V is the volume, k_B is Boltzmann constant and the subscript R refers to the reservoir.

Some of the gas transferred to the sample holder will remain in the gas phase and some will adsorb onto the sample. Once equilibrium is reached (i.e. the gas pressure no longer changes with time), we can calculate the amount that remains in the gas

phase.

$$\Delta N_S = \frac{P'_S V'_S}{T'_S k_B} - \frac{P_S V_S}{T_S k_B} \tag{5.26}$$

The subscript S refers to the sample holder. Assuming that there are no leaks in the system the total number of gas molecules must remain constant. Hence,

$$\Delta N_R + \Delta N_S + \Delta N_A = 0 \tag{5.27}$$

where N_A is the number of adsorbed molecules. Substituting equations 5.25 and 5.26 into 5.27 and solving for N_A gives:

$$\Delta N_A = -\left(\frac{P'_R V'_R}{T'_R k_B} - \frac{P_R V_R}{T_R k_B}\right) - \left(\frac{P'_S V'_S}{T'_S k_B} - \frac{P_S V_S}{T_S k_B}\right). \tag{5.28}$$

Traditionally, this result is reported in a volume of gas at STP (standard temperature and pressure). This is calculated by multiplying equation 5.28 by $\frac{k_B T_{STP}}{P_{STP}}$.

$$\Delta V_{ads} = -\frac{T_{STP}}{P_{STP}}\left[\left(\frac{P'_R V'_R}{T'_R} - \frac{P_R V_R}{T_R}\right) + \left(\frac{P'_S V'_S}{T'_S} - \frac{P_S V_S}{T_S}\right)\right] \tag{5.29}$$

Equation 5.29 represents the volume adsorbed in a single dose and must be totaled to get the volume of gas adsorbed onto the sample. Since the system is designed to begin after the sample has been throughly degassed, the total volume adsorbed (V_{ads}) as a function of pressure (p_n) after the n^{th} dose is calculated from:

$$V_{ads}(p_n) = \sum_{i=1}^{n} \Delta V_{ads}(p_i) \tag{5.30}$$

where p_1 would be the pressure of the gas in the sample holder after the first dose and after the system has reached equilibrium.

5.2.2 Temperature Stability and Design Considerations

Compensating for temperature fluctuations is one of the most important considerations facing a good gas adsorption apparatus design. The ideal gas law is used to

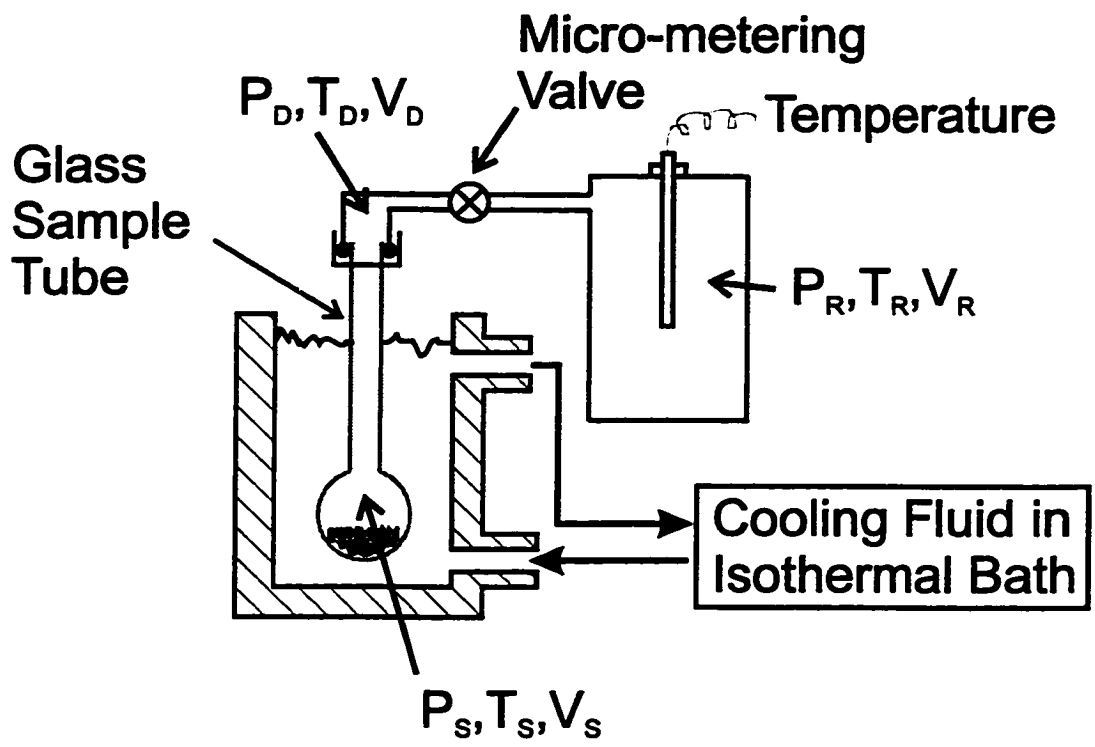

Figure 5.5: Schematic diagram of a gas adsorption analyser modified to control the sample temperature during adsorption.

calculate the gas quantities and thus it is important to know the temperature accurately and to insulate the apparatus against environmental changes. Furthermore, as we have seen in section 5.1.3, the Langmuir equation 5.16 contains a Boltzmann factor and hence is strongly dependent on temperature. In order to measure the adsorption isotherm (V_{ads} vs. p) we must control the temperature of the sample holder. Initially an ice bath was thought to be sufficient, however the temperature changes associated with melting produced substantial artifacts in the measured data. It was replaced by a temperature controlled flowing water/glycol bath and greatly improved the sensitivity of the measurements.

Unfortunately various problems prohibit submerging the entire apparatus in the water/glycol bath and this leads to the problem of temperature gradients. i.e. the

reservoir will be near room temperature while the sample holder is fixed at 273 K. The majority of the apparatus is constructed from 316 stainless steel and the sample holder is made of glass and is submerged in the water/glycol bath. The fittings and valves needed to connect the sample holder have significant volume and will most likely be close to room temperature. This presents the problem that the sample volume will consist of two separate sections at different temperatures. In order to isolate the temperature gradient in a region where the volume is small, the glass sample tube was designed with a small neck as shown in figure 5.5. The presence of this new volume created in the dead space of the valve and fittings, shown in grey, must be incorporated into equation 5.29.

$$\Delta V_{ads} = -\frac{T_{STP}}{P_{STP}}\left[V_R\left(\frac{P'_R}{T'_R}-\frac{P_R}{T_R}\right)+V_S\left(\frac{P'_S}{T'_S}-\frac{P_S}{T_S}\right)+V_D\left(\frac{P'_D}{T'_D}-\frac{P_D}{T_D}\right)\right] \quad (5.31)$$

V'_R, V'_S and V'_D have been factored out because the volumes do not change during operation.

The following assumptions are made when calculating the adsorption from equation 5.31:

1. The bath temperature does not change appreciably ($T'_S = T_S = 0°C$).
2. The pressure of the dead space and sample holder will be equal ($P_D = P_S$).
3. The temperature in the dead space is closer to the temperature of the surrounding metal fittings than the cooling bath and hence close to the temperature of the reservoir ($T_D \approx T_R$).

Thus we arrive at the final form of the equation used to calculate the volume adsorbed per dose of adsorbent.

$$\Delta V_{ads} = -\frac{T_{STP}}{P_{STP}}\left[V_R\left(\frac{P'_R}{T'_R}-\frac{P_R}{T_R}\right)+\frac{V_S}{T_S}\left(P'_S-P_S\right)+V_D\left(\frac{P'_S}{T'_R}-\frac{P_S}{T_R}\right)\right] \quad (5.32)$$

5.2.3 Automation and Increasing Accuracy

Automatic control of the gas pressure in the reservoir was achieved using an automatic three way valve (computer controlled) to fill/evacuate the reservoir as necessary. This

allows for adsorption and desorption to be run consecutively, reduces the amount of user intervention and increases the sensitivity and accuracy of the measurements. Although up to this point only the adsorption process has been discussed, equation 5.32 works equally well for desorption and this can be achieved by removing gas from the sample holder by having the reservoir at a lower pressure (usually near vacuum).

The majority of the error involved in this experiment results from determining the volume of adsorbent transferred to and from the reservoir. Without being able to refill/evacuate the reservoir, the reservoir volume has to be much larger to ensure the needed pressure gradient to dose/negative dose the sample towards the end of adsorption/desorption. Hence the pressure changes are smaller and the resulting error in calculating the volume of gas transferred is larger. Reducing this error requires larger pressure and hence a smaller reservoir volume that must be either filled or evacuated before dosing/negative dosing. Two automatic valves connected to a gas supply line and vacuum respectively have been added to the apparatus as shown in fig 5.6 to accomplish this function.

The adsorption process in hard carbon may take very long periods (days - weeks) to reach equilibrium. In order to measure a useful amount of data in less time, the adsorption measurements can be performed under pseudo equilibrium conditions provided the choice of equilibrium is consistent between successive data points. To achieve this goal, a computer was used to fully automate the apparatus so that after the sample was loaded and degassed, both adsorption and desorption could be performed without the intervention of the user. Once the system reaches a user-defined pressure limit for adsorption (e.g. the sample holder reaches atmospheric pressure) then the system evacuates the reservoir and begins negative dosing the sample holder but continues to perform all the calculations in the same manner. In this way, continuity between adsorption and desorption is ensured. A schematic of the gas adsorption apparatus is shown in figure 5.7.

Determining a consistent equilibrium condition was achieved by calculating the magnitude of the rate of pressure change in the sample holder and then comparing

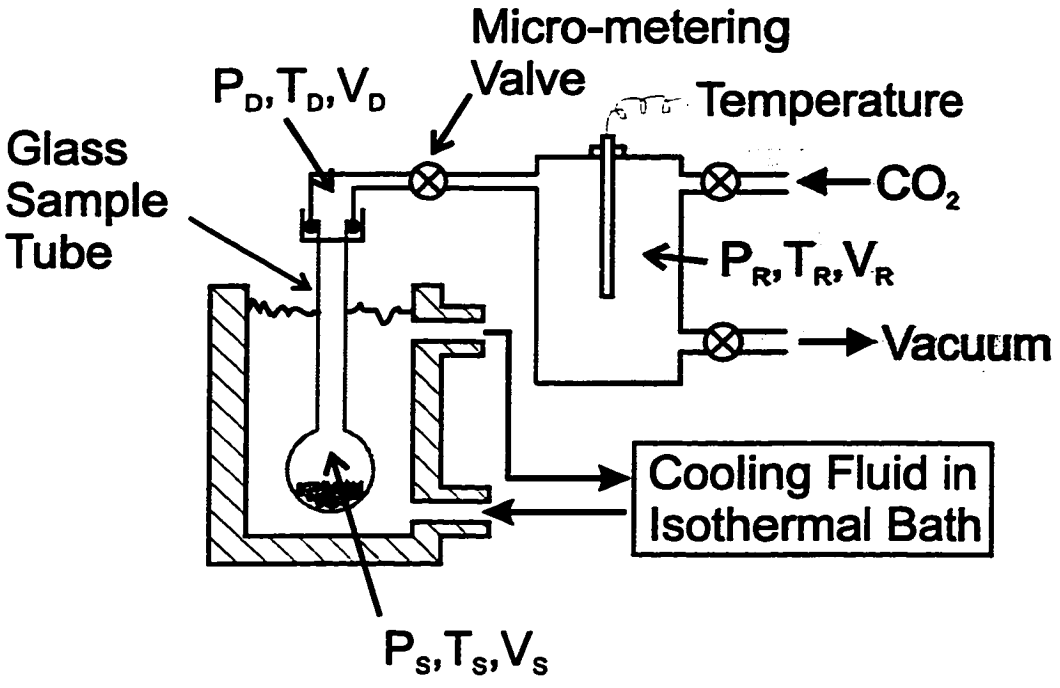

Figure 5.6: Schematic diagram of the gas adsorption apparatus with the additional ability to fill/evacuate the reservoir through the automated valves to vacuum and gas supply.

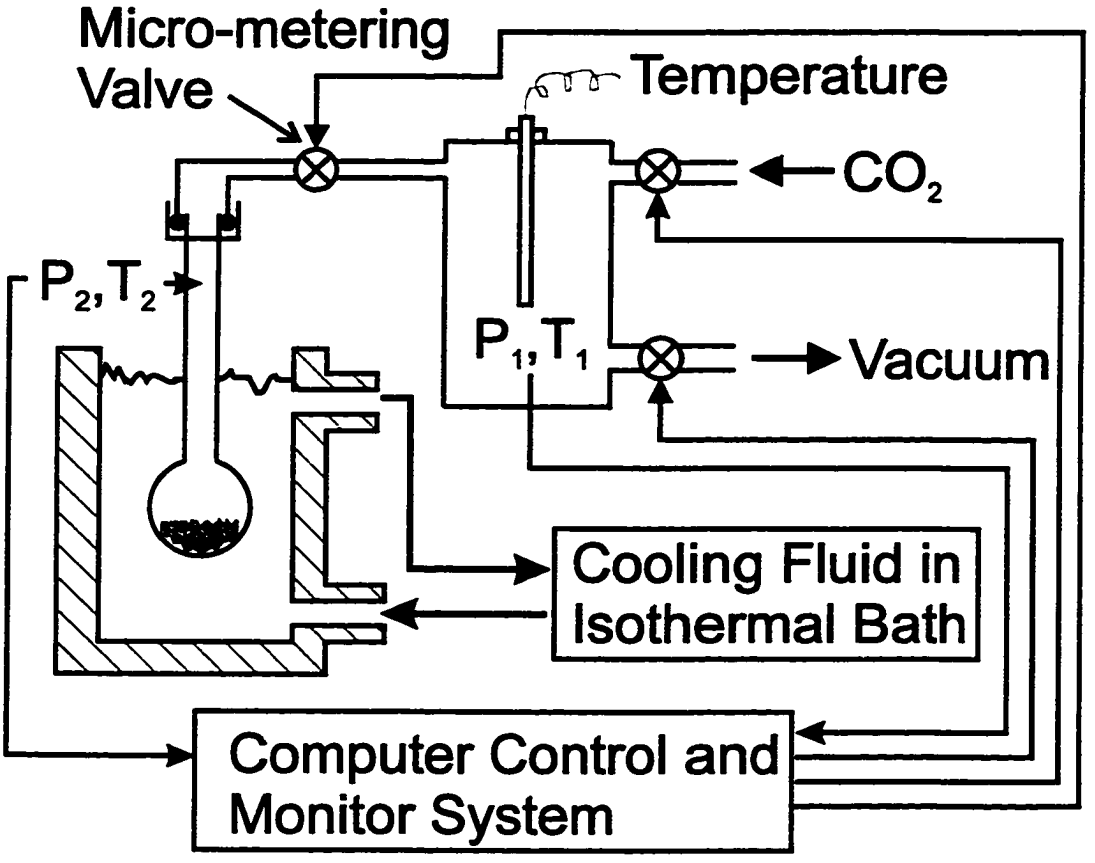

Figure 5.7: Schematic diagram of the CO_2 gas adsorption apparatus with automated computer control.

this valve to a predefined cut-off point. The rate of pressure change is calculated by running a linear least-squares fitting function to the last twenty pressure data points (collected every 15 seconds) to extract the slope and hence rate of pressure change.

$$\frac{dp}{dt} = \frac{\sum t_i p_i - \frac{1}{n}\sum t_i \sum p_i}{\sum t_i^2 - \frac{1}{n}\left(\sum t_i\right)^2} \tag{5.33}$$

p_i and t_i are the pressure and time of measurement respectively and the sum is over the last twenty data points which corresponds to approximately five minutes.

5.3 Calibration

Several different devices had to be calibrated before the adsorption measurements could be performed. In order to verify the machine was working properly after calibration, a blank sample tube and a graphite sample were tested and both showed negligible adsorption when compared to a hard carbon sample. The devices/parameters that need to be calibrated are the RTD temperature sensor in the reservoir, the pressure transducers, the reservoir volume, dead space volume and sample holder volume.

5.3.1 RTD Temperature Calibration

The RTD (Omega) was calibrated using a standard laboratory thermometer, beaker of water, stirring bar and hot plate as shown in figure 5.8. The stirring bar was used to keep the water well mixed and the thermometer and RTD were adjacently positioned in the beaker to the same depth. The temperature in the bath was slowly raised at a rate of about 1°C/min. from 0°C to 90°C; the temperature of the bath and resistance of the RTD were recorded and tabulated in table 5.1.

5.3.2 The Pressure Transducers

The pressure transducers used were Sensotec model TJE/713-01TJA. The output of each is approximately 3 mV/V of excitation potential at 25 psia. The excitation

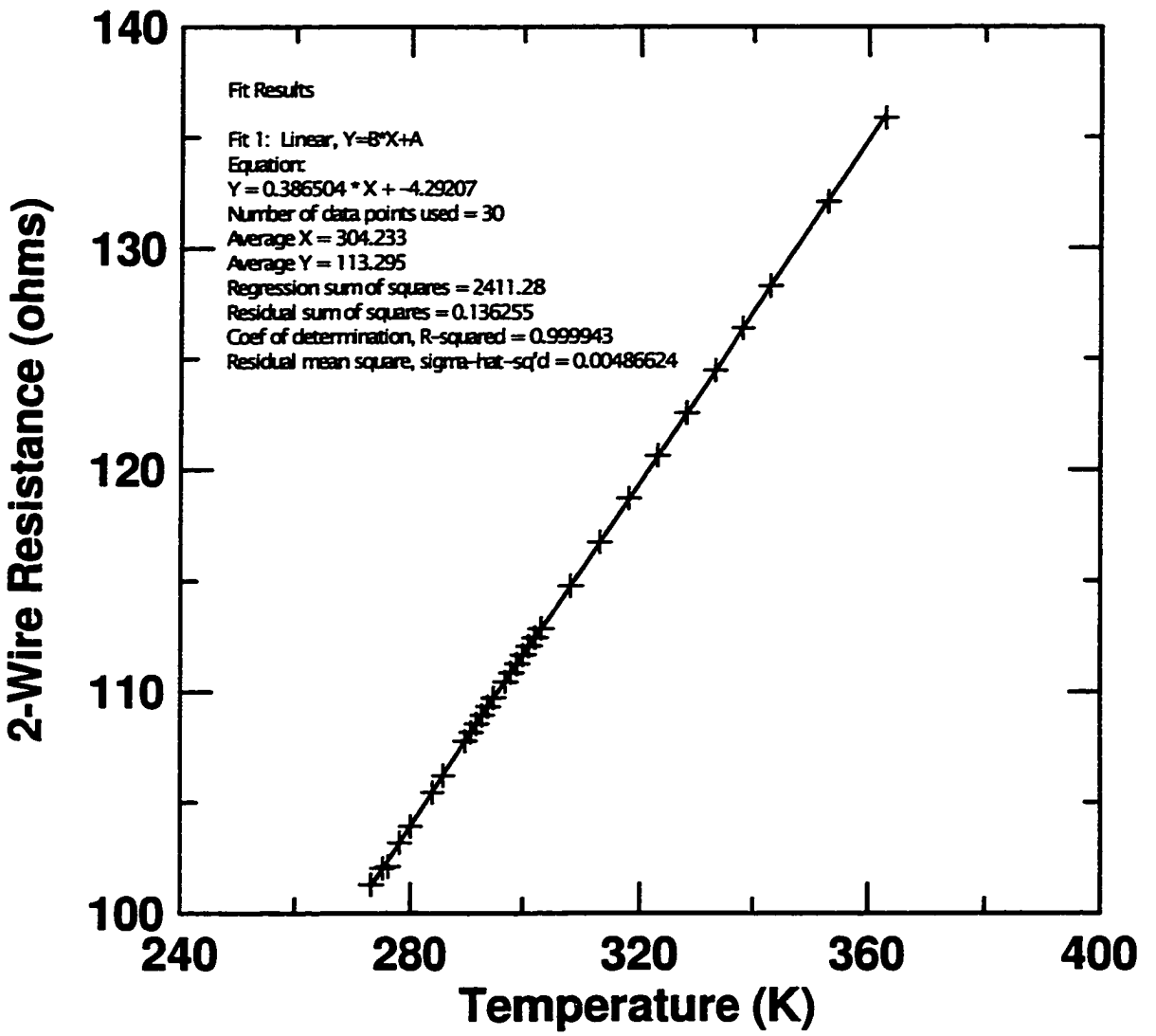

Figure 5.8: RTD temperature calibration measured using a thermometer, beaker of water, hot plate and stirring bar.

Temperature (K) ±0.2	Resistance (ohms) ±0.05	Temperature (K) ±0.2	Resistance (ohms) ±0.05
273.0	101.30	299.0	111.27
275.0	102.03	300.0	111.68
276.0	102.11	301.0	112.07
278.0	103.18	302.0	112.45
280.0	103.92	303.0	112.86
284.0	105.45	308.0	114.77
286.0	106.22	313.0	116.74
290.0	107.78	318.0	118.70
291.0	108.18	323.0	120.62
292.0	108.56	328.0	122.53
293.0	108.96	333.0	124.46
294.0	109.34	338.0	126.38
295.0	109.74	343.0	128.28
297.0	110.46	353.0	132.08
298.0	110.88	363.0	135.86

Table 5.1: The measured resistance and temperature for calibration of the RTD used to measure the temperature of the reservoir.

potential was set at 10 V and hence the full range output of the transducers is approximately 30 mV at 25 psia. These transducers can operate over the pressure range of 0-25.0 psia and are accurate to within 0.1% of full range (0.03 psia). They are calibrated to zero pressure by applying a vacuum to the system for at least 24 hours and measuring the output voltage. The system is then opened and calibrated to atmospheric pressure. In this way, the two pressure scales are calibrated to be consistent with each other.

In order to check for linearity, the reservoir was filled with gas and the sample holder was evacuated. The empty sample holder, at room temperature, was slowly dosed with gas from the reservoir and the two pressures were recorded once the system reached equilibrium (as shown in figure 5.9). If the pressure transducers were non-linear the resulting graph would appear curved assuming the test gas obeys the ideal gas law in this pressure region. By inspection the graph is linear and the transducers were assumed to be operating accurately.

5.3.3 Volume Calibration

There are many different ways to measure the volumes of the dead space, reservoir and sample holders. Equation 5.32 tries to take into account the temperature effects however it is not likely to be perfect and it is desirable to reduce these and other errors using good calibration techniques. We would like to determine the best values (for the parameters in equation 5.32) that will give negligible adsorption isotherms for empty sample holders of different volume. Many different sized sample holders ranging in size from about 20-200 ml were fabricated and their volumes were determined by measuring the mass of water needed to fill them. The volume of each sample holder could be measured to less than ± 0.1 ml.

The actual calibration process consists of measuring the normal adsorption isotherm on several blank sample holders of different volume and then optimizing the parameters to give the least amount of adsorption for the group. First, recall that we need to

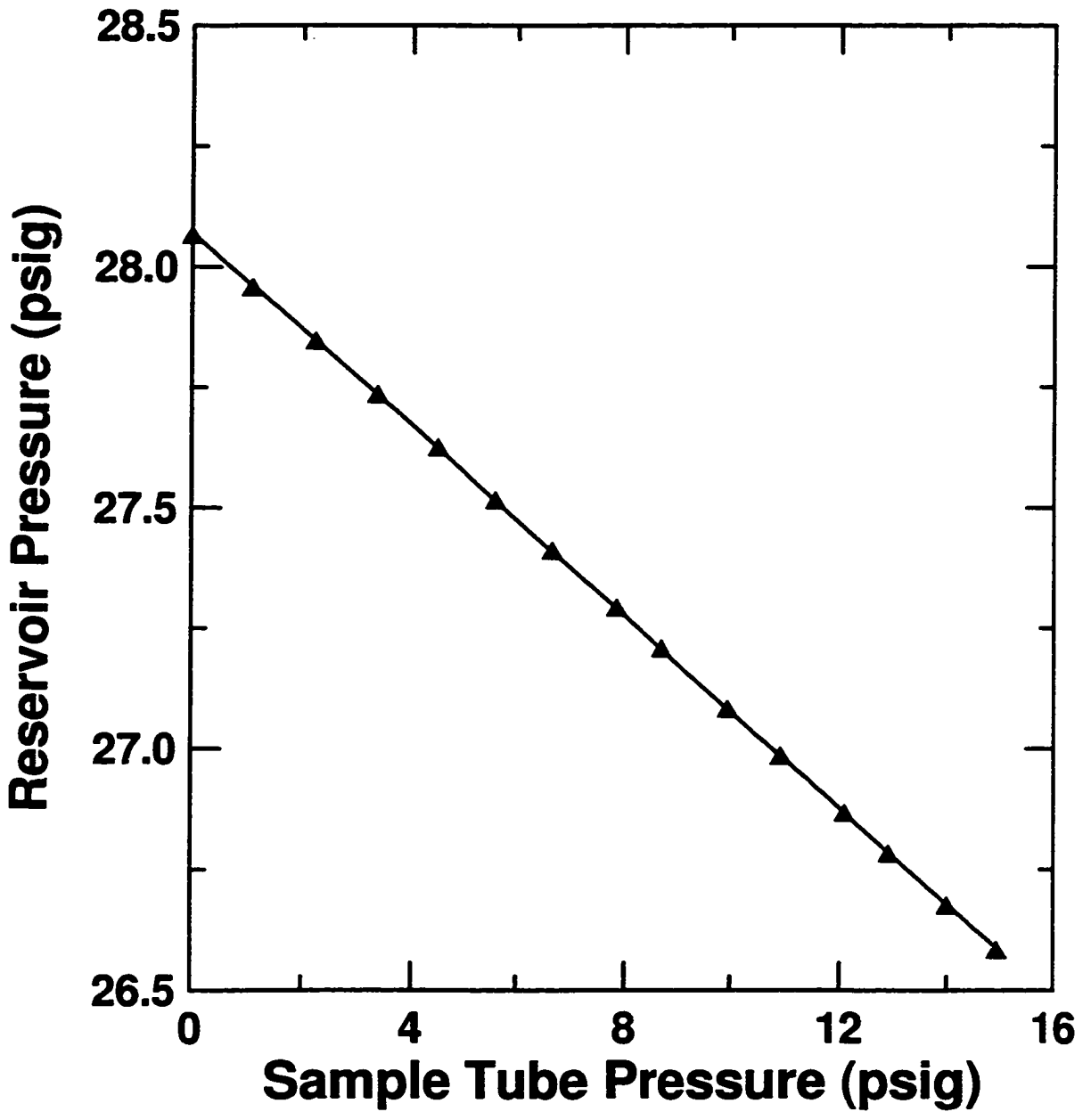

Figure 5.9: Verification of the linearity of the pressure transducers. The solid line represents a linear least-squares fit to the measured data.

mass of sample	N/A	Volume Correction:	V_R'/V_R	V_S'/V_S	V_D'/V_D
sample holder volume	23.59		0.982	1	1
sample_name	calibration				

P/Po	Vads (STP-ml/g)	dV_R	dV_S	dV_D	dV_R+dV_S+dV_D	Vads	chi^2
0.000	0.000	0.00	0.00	0.00	0.00	0.00	0.0000
0.071	0.042	-9.80	4.27	5.21	0.06	-0.02	0.0004
0.141	0.088	-9.40	4.18	5.09	0.04	-0.03	0.0012
0.193	0.125	-7.04	3.13	3.81	0.03	-0.04	0.0019
0.248	0.168	-7.44	3.30	4.02	0.01	-0.05	0.0024
0.302	0.204	-7.40	3.29	4.01	0.03	-0.06	0.0037
0.363	0.259	-8.28	3.66	4.47	-0.01	-0.06	0.0035
0.425	0.313	-8.38	3.71	4.52	0.00	-0.06	0.0035
0.477	0.366	-7.15	3.16	3.85	-0.02	-0.05	0.0028
0.546	0.430	-9.38	4.14	5.05	-0.01	-0.05	0.0024
0.598	0.479	-7.11	3.14	3.83	-0.01	-0.05	0.0021
0.663	0.547	-8.78	3.87	4.72	-0.03	-0.03	0.0012
0.726	0.615	-8.65	3.81	4.65	-0.03	-0.02	0.0005
0.780	0.669	-7.31	3.22	3.93	-0.02	-0.02	0.0003
0.837	0.744	-7.82	3.43	4.18	-0.07	0.01	0.0001
0.890	0.803	-7.29	3.21	3.92	-0.03	0.02	0.0004
0.951	0.883	-8.30	3.64	4.44	-0.07	0.05	0.0021
0.888	0.777	8.66	-3.77	-4.60	0.06	0.02	0.0006
0.823	0.679	8.89	-3.88	-4.73	0.03	0.01	0.0002
0.765	0.589	8.04	-3.51	-4.28	0.03	0.00	0.0000
0.705	0.496	8.29	-3.62	-4.41	0.03	-0.01	0.0001
0.644	0.407	8.41	-3.68	-4.48	0.02	-0.02	0.0004
0.586	0.320	7.88	-3.44	-4.19	0.03	-0.03	0.0009
0.526	0.238	8.32	-3.65	-4.44	0.00	-0.03	0.0010
0.470	0.157	7.85	-3.35	-4.08	0.02	-0.04	0.0014
0.414	0.075	7.88	-3.36	-4.09	0.02	-0.04	0.0020
0.358	-0.002	7.74	-3.39	-4.13	0.01	-0.05	0.0023
0.303	-0.073	7.55	-3.31	-4.04	-0.01	-0.05	0.0021
0.247	-0.149	7.62	-3.34	-4.07	0.00	-0.05	0.0022
0.194	-0.218	7.29	-3.20	-3.90	0.00	-0.05	0.0021
0.144	-0.282	6.88	-3.02	-3.68	-0.01	-0.04	0.0018
						chi^2(sum)	0.028523

Figure 5.10: The calibration data recorded from measuring the adsorption isotherm of a blank sample holder. The grey region represents the data obtained directly from the instrument. The spread sheet is used to determine the optimum values of V_R and V_D that yield the least amount of adsorption based on a χ^2 fitting algorithm.

determine the values of V_R and V_D in equation 5.32 before we can calculate the volume adsorbed onto the sample; all other parameters are already known or measured directly. We choose not to try to measure the values of V_R and V_D directly (by say filling the machine with water) because what we really want are the effective values that will give zero adsorption for various sizes of sample tube. Hence the method we choose is to measure all the important data needed to calculate the volume adsorbed from equation 5.32, organise it into a spreadsheet and then manipulate the value of V_D and V_R until we get negligible adsorption.

An example of this calculation is shown in figure 5.10. The grey region represents the data recorded by the instrument. The values of dV_R, dV_S and dV_D are taken directly from equation 5.32, i.e.

$$dV_R = V_R\left(\frac{P'_R}{T'_R} - \frac{P_R}{T_R}\right), \tag{5.34}$$

$$dV_S = \frac{V_S}{T_S}\left(P'_S - P_S\right), \tag{5.35}$$

$$dV_D = V_D\left(\frac{P'_S}{T'_R} - \frac{P_S}{T_R}\right). \tag{5.36}$$

If these values are added, multiplying by $-T_{STP}/P_{STP}$ as in equation 5.32, the result is the volume adsorbed as reported by the instrument. However, multiplying dV_R, dV_S and dV_D by some coefficients is effectively the same as changing V_D, V_S and V_R. These are the values of V'_R/V_R, V'_S/V_S and V'_D/V_D as shown on the spreadsheet. As can be expected, changing any of these numbers changes the total volume adsorbed at every point which we would like to get as close to zero as possible. Since there are many points, we use a χ^2 fitting algorithm to determine the best values of V_R and V_D; recall V_S has already been determined accurately.

Since, for a single calibration isotherm on a blank sample holder, there is only one number being calculated (i.e. the sum of χ^2), we can not optimize both dV_R and dV_D at the same time. That is to say, we cannot calibrate both the zero point and scale for adsorption with data from one sample holder. Hence, the data from two sample holders of different volume are used and a χ^2 fitting algorithm (applied to both sets of data simultaneously) is used to determine the best values of dV_R and dV_D.

Using this method, the measured volume of adsorption can be determined to better than ±0.1 ml; this being the range over which the adsorption in a blank sample holder was seen to fluctuate. Hard carbon typically adsorbs approximately 40 ml of gas (for a 1g sample) and hence the corresponding error is ±0.3%. The measured adsorption isotherms of a blank sample holder, graphite and a hard carbon are shown in figure 5.11. Graphite has similar chemistry to hard carbon however it does not exhibit a micropore structure and hence it the large difference in the observed adsorption isotherm is attributed to the micropores in the hard carbon.

This system will be used in great detail in the following chapters to compare the micropore structures of different hard carbon and to determine how that structure affects lithium insertion properties.

5.4 Sample Preparation

The samples were prepared for analysis in the following manner. 1 gram of the powders used to make electrochemical cells was sealed in a glass sample tube and outgassed at < 10 mTorr and 300°C for at least 8 hours prior to analysis. The heating apparatus was then removed and replaced by a dewar containing a flowing cooling fluid (as shown in figure 5.7) connected to a thermostatically controlled reservoir. In this way the sample was not exposed to temporal thermal gradients (e.g. those caused by melting ice) and the sample temperature could be controlled to less than 0.1°C. For all measurements, the temperature of the cooling bath was fixed at (0.0 ± 0.1)°C. The degassed sample tube was then dosed with CO_2 by opening and closing the computer-controlled micro-metering valve. Once the pressure in the sample tube reached equilibrium (did not change by more than 0.1 Torr/min.), the amount of gas adsorbed by the sample was calculated using equation 5.32. Kinetics of adsorption data (i.e. the volume of gas adsorbed as the pressure in the sample tube progresses towards equilibrium) was also recorded for each dose.

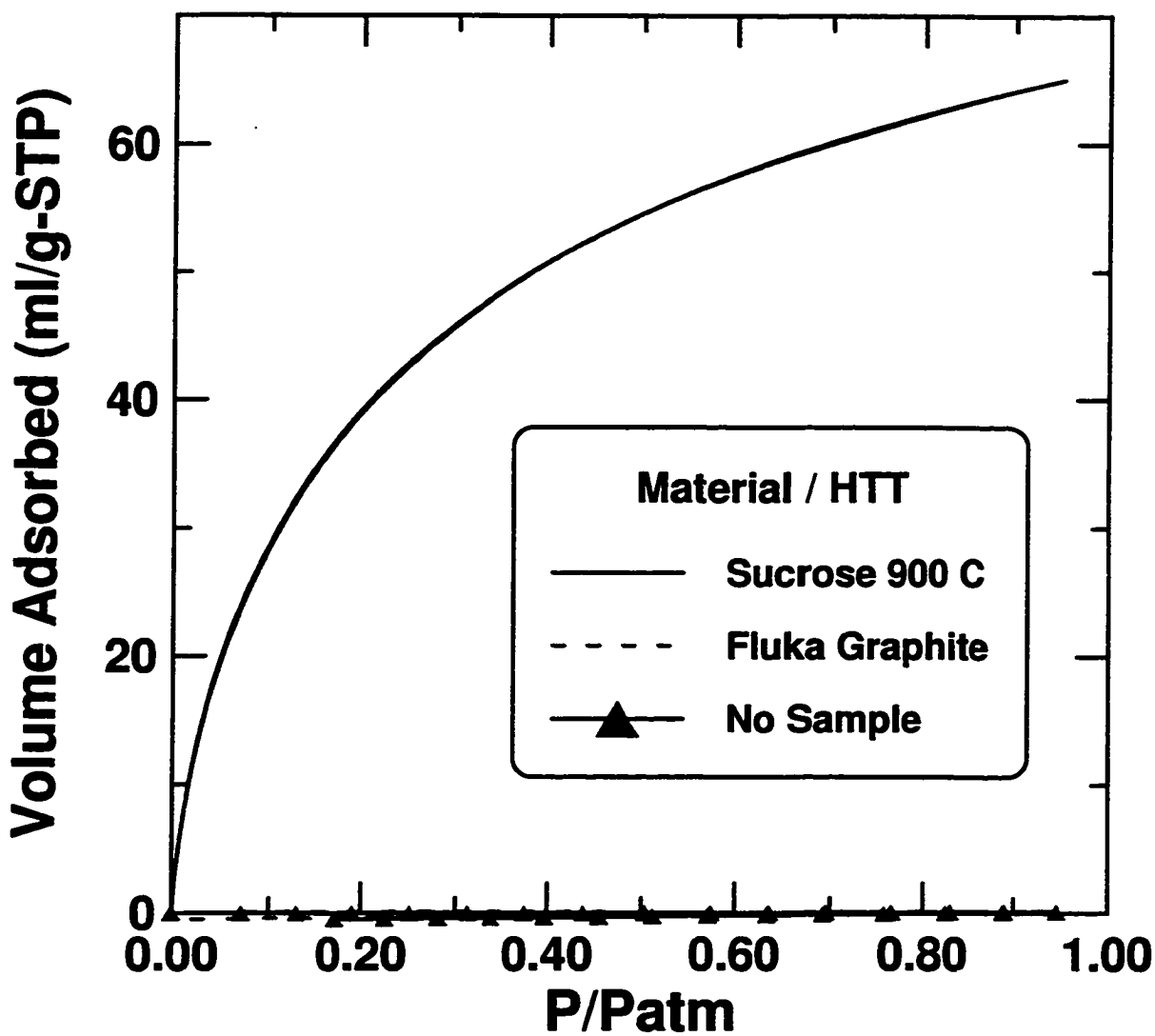

Figure 5.11: The measured adsorption isotherms of hard carbon, graphite and an empty sample holder on the fully calibrated apparatus.

5.5 Conclusion

In this chapter, the construction and calibration of a gas adsorption analyser has been explained with emphasis placed on the "physics" behind the design. This apparatus was tested first with a blank sample holder and later with graphite showing negligible adsorption when compared to a hard carbon sample prepared from sucrose pyrolysed at 900°C. Hence we can conclude that the measured adsorption isotherm is a result of the microporous structure in hard carbon since the graphite sample, with similar chemistry but no micropores, shows no adsorption. The sample loading/degassing procedures have also been explained. This equipment will be used a great deal to characterise the hard carbon samples presented in the next chapters.

One other question that may be of concern; why wasn't a commercially available machine used considering we have one of such machines in our lab. I chose not to include adsorption/desorption isotherms measured by the brand-new Micromeritics ASAP 2000 (cost: $75k) because the data is inconsistent, unbelievable and very difficult to repeat. In order to be fair, it is a good machine for general purpose use and the adsorption isotherm of hard carbon is difficult to measure because determining when a sample has reached equilibrium is critical in obtaining good, consistent, results. Furthermore, many of the hard carbons we wish to analyse exhibit partially closed micropores and are arguably some of the most difficult samples to measure. Other types of hard carbon, such as those designed for water decolourizers and filtering applications, are activated to open the microporosity, and hence are not as sensitive to the equilibrium criteria. Thus, the much less sophisticated and simple design explained in this chapter works well because it is simple, easy to maintain and the purpose of each part is fully understood. It has far fewer parts and only operates one valve which is less likely to fail (essentially leak) when compared to the scores of valves and the complicated design and control algorithms of the commercial machine.

Chapter 6

Irreversible Capacity in Hard Carbon

The irreversible capacity is one of the most important factors preventing the commercialization of hard carbon for Li-ion batteries. Weibing Xing et. al. [4] showed that there are two mechanisms that contribute to the irreversible capacity in hard carbon: 1) reaction of lithium with the electrolyte to form a passivating layer and 2) the reaction of lithium with surface functional groups or absorbed molecules that result from exposing the sample to air after pyrolysis. The electrolyte/lithium reaction will always occur to some extent unless electrolytes can be found that do not react with lithium. This reaction takes place on the surface of the electrode to form a passivating layer called the solid electrolyte interface (SEI). The surface area is likely more important than surface chemistry and usually contributes $\approx$50 mAh/g to the irreversible capacity. The second component is specific to hard carbon and normally contributes $\approx$100 mAh/g; the research presented here focuses primarily on reducing this component of the irreversible capacity.

The mechanism for the irreversible capacity has not yet been completely determined however our results suggest that the adsorption of water on the surface may play an important role. The experimental results presented in this chapter show that

the increased irreversible capacity is not correlated to any changes in the bulk properties of the material as measured by WAXS and SAXS, is not likely explained by the small changes in surface area/micropore structure as shown by gas adsorption studies and is not correlated to the formation of surface functional groups by XPS measurements. In fact, in almost all instances we can show trends in the irreversible capacity and yet by all of our measurements both the bulk and surface properties of the samples remain the same. This has lead us to an obvious candidate; the adsorption of water on the surface of the sample where, for a microporous carbon, the surface also includes the internal surface area of the micropores. TGA results will show that there is substantial mass loss as the materials are heated above 100°C and this we believe results from the desorption of water from the material.

Two processes have been found to lead to lower irreversible capacity in hard carbon; the chemical vapour deposition (CVD) of a carbonaceous substance from ethylene gas at temperatures >700°C and lowering the temperature during the dewatering process. The first technique modifies the surface of the hard carbon before it is exposed to air and this produces a large reduction in the irreversible capacity from >150 mAh/g to <70 mAh/g. Lowering the dewatering temperature has a similar effect which we attribute to preventing the oxidation of the sample that somehow leads to larger irreversible capacities after pyrolysis.

6.1 Ethylene Treatment

In this section, different methods of surface treatment by carbonaceous deposition will be explained and their effects on the irreversible capacity will be shown. These samples will characterized by WAXS, SAXS, BET and XPS measurements.

6.1.1 Sample Preparation

The carbonaceous deposition process can be performed both during and after pyrolysis and the thickness of the deposited carbonaceous layer can be controlled using

one of five different techniques. The pyrolysis process and surface treatment was performed inside a tube furnace using a one inch diameter quartz tube. The sample was contained inside a nickel boat and 6 ± 0.1 grams of dewatered sucrose was the standard mass used.

Vacuum Pyrolysis of Dewatered Sucrose

The first two samples were vacuum pyrolysed at temperatures of 900°C and 1100°C respectively, as described in Table 6.1. These samples were not surface treated and serve as experimental controls for the treated samples.

Direct Pyrolysis of Samples in Ethylene

After the initial out-gassing in vacuum, the third sample was pyrolysed in a steady flow of 200 cc/min of ethylene. The sample temperature profile for vacuum pyrolysis was used (see Table 6.1).

Post Pyrolysis Ethylene Treatment in Steady Flow

The next three samples (4, 5 and 6 in Table 6.1) were first vacuum pyrolysed in the normal fashion and cooled to room temperature. The vacuum was removed and a flow of ethylene gas (200 cc/min) was initiated. The samples were then reheated at 50°C/min to the desired heat treatment temperature for carbon deposition. They remained at this temperature for 1 hour before being cooled to room temperature.

Post Pyrolysis Ethylene Treatment with Single Dose

These samples were pyrolysed as explained in the previous section, however instead of depositing the carbonaceous material from a steady flow of ethylene gas, the tube was filled with ethylene to 30 kPa and sealed. This corresponds to a ratio of approximately 200 cc of ethylene for every 6 grams of dewatered sugar precursor material. The remaining samples were prepared in this way (see Table 6.1) except for the sample treated at 1100°C which was exposed to ethylene for 12 hours at this temperature.

CVD of Carbon on Nickel Foil

In order to determine the electrochemical properties of the material being deposited on the samples, nickel foil was heated in 200cc/min of ethylene gas at 900°C for five hours to deposit a significant amount of carbon directly onto the foil. This sample was then used without further processing to make electrochemical cells directly.

The nickel surface is very different from the surface of hard carbon and consequently the deposited carbonaceous material may have different properties. These electrodes are also not made in the usual way and how this effects the electrochemical behaviour for lithium insertion is unknown. With that said, these electrodes provide the best means of isolating the carbonaceous material deposited from ethylene gas and will provide us with many insights into the electrochemical behaviour of this material.

6.1.2 Sample Characterization

X-ray diffraction, small angle X-ray scattering,CO_2 gas adsorption and BET surface area measurements were used to characterize the stacking of graphene sheets, the number and size of micropores and the open microporosity of the samples.

X-ray photoelectron spectroscopy (XPS) measurements were carried out with an ultra-high vacuum surface analysis system at Simon Fraser University. The base pressure of the system was better than 1×10^{-10} torr. A hemispherical electron energy analyser (Perkin Elmer 10-360 Precision Energy Analyser) was used for the electron spectroscopy. The combined instrument resolution is believed to be 0.8 eV (using a 50-eV pass energy). Samples were prepared by pressing pellets from sucrose dewatered at 180°C and then processing the pellets identically to those samples prepared for electrochemical testing. The samples were exposed to lab air for 1 week and then held with a piece of copper foil to a stainless-steel holder to ensure adequate grounding during the XPS measurement.

Sample	Material	HTT (C)	Net Yield %	Ethylene Exposure			Rev. Cap. mAh/g	Irrev. Cap. mAh/g	BET (m2/g)
				Temp. (C)	Flow Rate (cc/min)	Method of Exposure			
#1	Sucrose	900	32.5	N/A	N/A	N/A	511	220	251
#2	Sucrose	1100	33.3	N/A	N/A	N/A	532	149	114
#3	Sucrose	900	48.1	900	200	During Pyrolysis	516	52	22
#4	Sucrose	1100	30.5	300	200	Post Pyrolysis	537	131	71
#5	Sucrose	1100	30.4	500	200	Post Pyrolysis	548	136	39
#6	Sucrose	1100	35.5	700	200	Post Pyrolysis	571	60	28
#7	Sucrose	1100	31.3	700	0	Post Pyrolysis	600	71	41
#8	Sucrose	1100	31.2	800	0	Post Pyrolysis	545	79	86
#9	Sucrose	1100	31.2	900	0	Post Pyrolysis	541	70	29
#10	Sucrose	1100	31.0	1000	0	Post Pyrolysis	533	63	63.7
#11	Sucrose	1100	31.2	1100	0	Post Pyrolysis	416	14	74
#12	No Sample	900	N/A	N/A	200	During Pyrolysis	522	27	N/A

Table 6.1: Preparation conditions and properties of the samples described in the text.

6.1.3 Results and Discussion

Electrochemical Testing

The first two samples (no ethylene treatment) will be considered to display the 'benchmark' charge/discharge curves for untreated hard-carbon materials. These samples produce results that are consistent with numerous authors [4, 76, 42, 9], i.e. they show large irreversible capacity; the reduction of which is the focus of this chapter. The yield was calculated as the ratio of the mass after either dewatering or pyrolysis to the mass of the starting precursor material; the yield for both is tabulated in Table 6.1. Yields in excess of those measured for the vacuum pyrolysed samples show evidence for the deposition of carbonaceous material from the ethylene treatment.

Electrochemical tests shown in figure 6.1 indicate that the irreversible capacity for the cell made from the sample pyrolysed in ethylene is substantially lower than that of the vacuum pyrolysed sample (52 mAh/g vs. 220 mAh/g) while the reversible capacity remains essentially the same (516 mAh/g vs. 511 mAh/g for the vacuum pyrolysed sample). The first curve (sample 12) in figure 6.1 is the voltage profile of the CVD of ethylene directly onto a nickel current collector that was subsequently

made directly into a cell. The large hysteresis in the voltage profile of this material is indicative of a soft carbon with large hydrogen content. Such a material has low commercial value because the large hysteresis significantly reduces the voltage of a real cell. Hence, the goal of these experiments is to treat the surface of a hard carbon with enough soft carbon to reduce the irreversible capacity but not so much as to increase the hysteresis in the voltage profile.

There are two contributions to the irreversible capacity labelled A and B on figure 6.1. 'A', corresponds to the formation of the SEI layer [21] and is visible in all carbonaceous anode materials leading to between 30 and 50 mAh/g of irreversible capacity [4]. We believe the second component, 'B', is particular to hard carbon materials exposed to air and leads to an increase in irreversible capacity of up to 200 mAh/g. This can be explained by either the presence of surface functional groups or adsorbed molecules of air (possibly water) on the surface. The ethylene treatment has the effect of modifying the surface of the hard carbon to prevent adsorption/formation of surface functional groups and hence essentially eliminates this component of the irreversible capacity.

The large yield of the sample pyrolysed to 900°C in ethylene indicates substantial deposition of carbonaceous material that is high in hydrogen content. More controlled treatment techniques will show the same reduction in irreversible capacity can be achieved without significant increases in yield.

Ethylene treating the samples after pyrolysis allows for better control of the deposition process. Figure 6.2 shows that such samples exposed to ethylene at temperatures above 700°C show evidence for the reduction in irreversible capacity to about 70 mAh/g. The samples treated at 300°C and 500°C do not show a reduction in irreversible capacity and this seems to indicate that the deposition process is not occurring at these low temperatures.

A further step to reduce the amount of carbon deposition is to treat the samples with only a fixed amount of ethylene. Such samples still produced the reduction in irreversible capacity observed by the first two treatment procedures. Figure 6.3

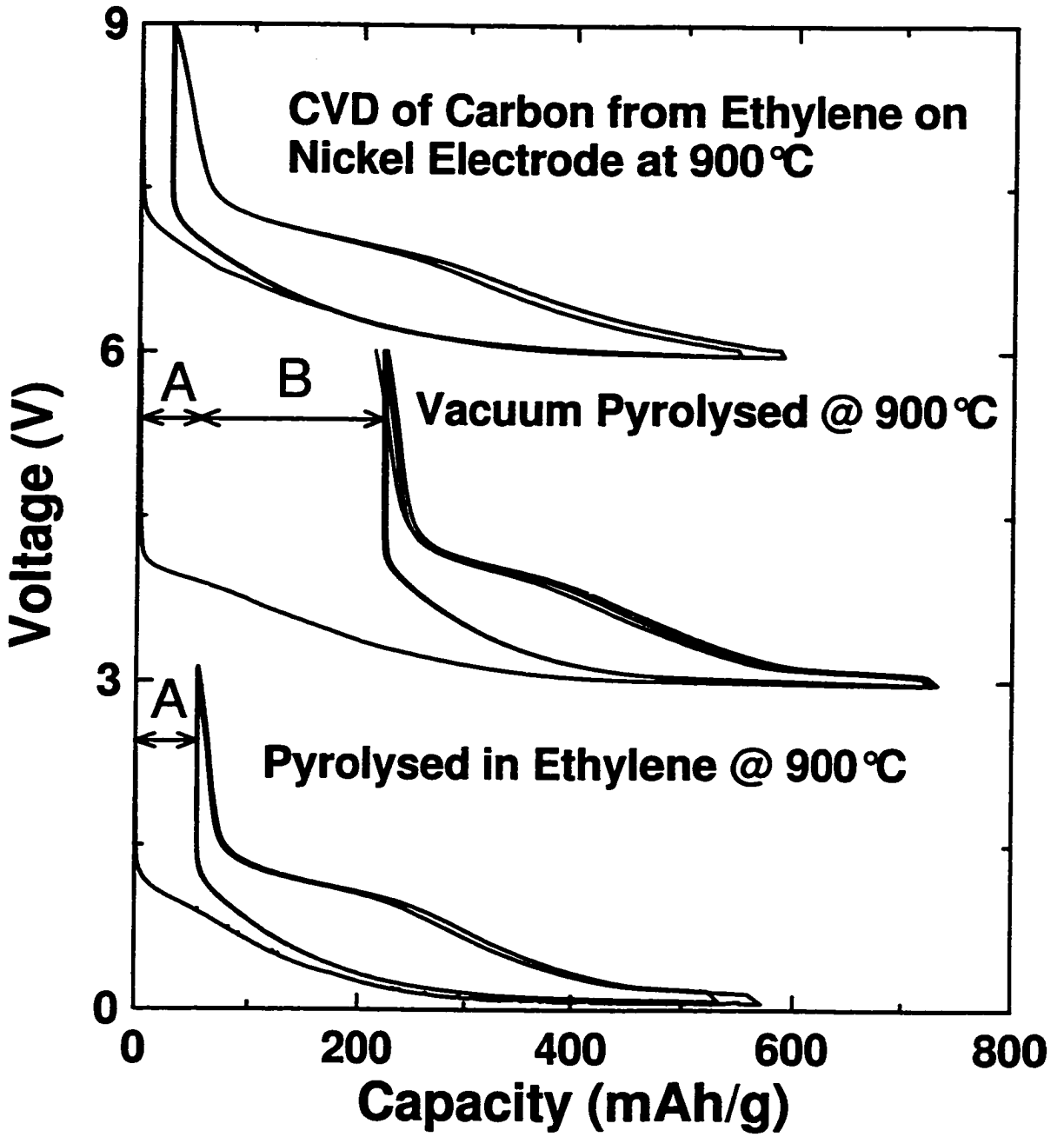

Figure 6.1: Voltage-capacity profiles for the specified samples. The data has been shifted sequentially by 3 V for clarity. The irreversible capacity in hard carbon is thought to contain two components; A: related to the formation of the SEI layer and B: the component related to the reaction of Li atoms with species adsorbed from air in the micropores of the sample.

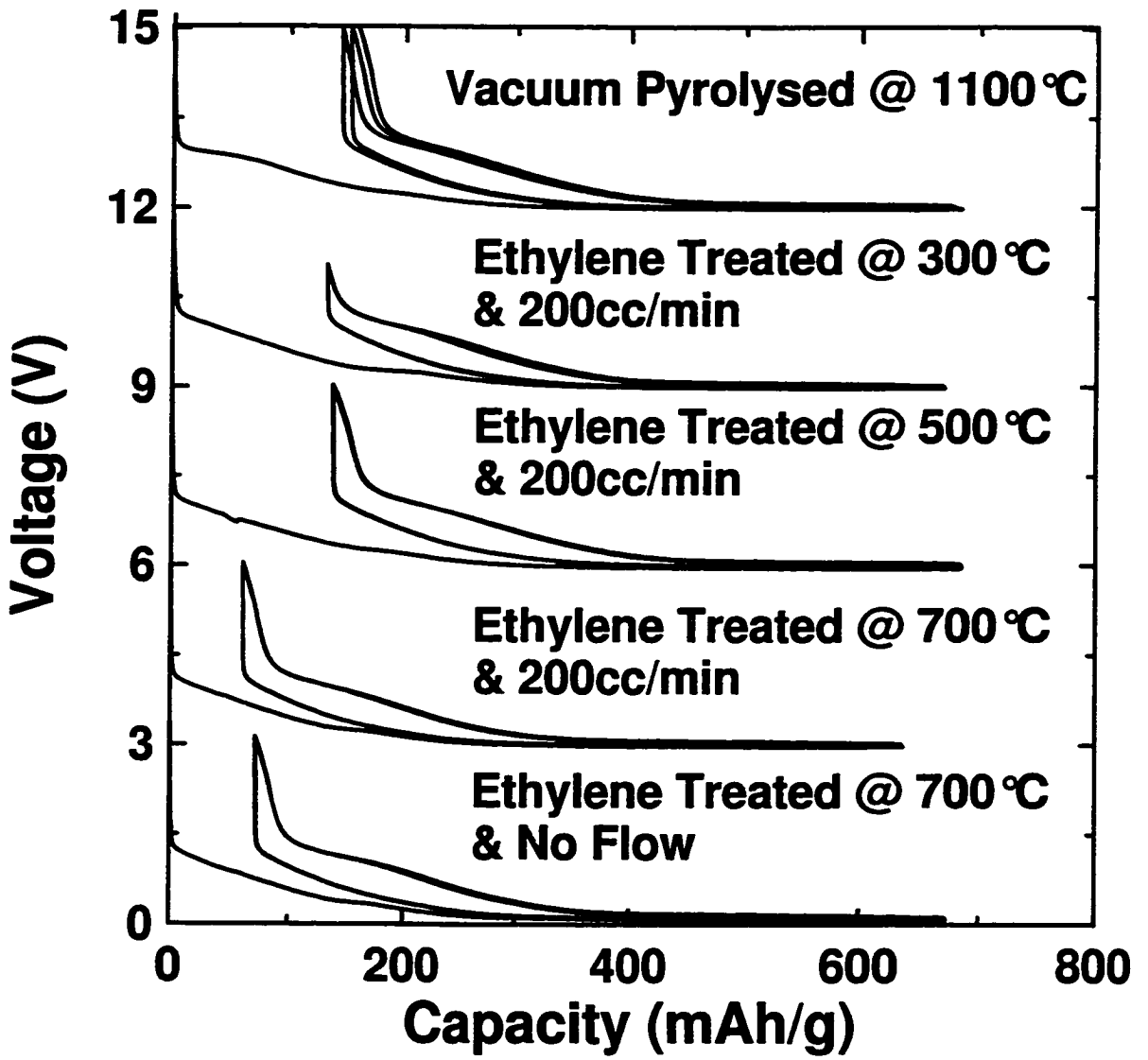

Figure 6.2: Voltage-capacity profiles for samples treated with ethylene after vacuum pyrolysis with a flow rate of 200 cc/min., vacuum pyrolysed to 1100°C and treated with a single dose of ethylene after vacuum pyrolysis. Curves have been shifted sequentially by 3 V for clarity.

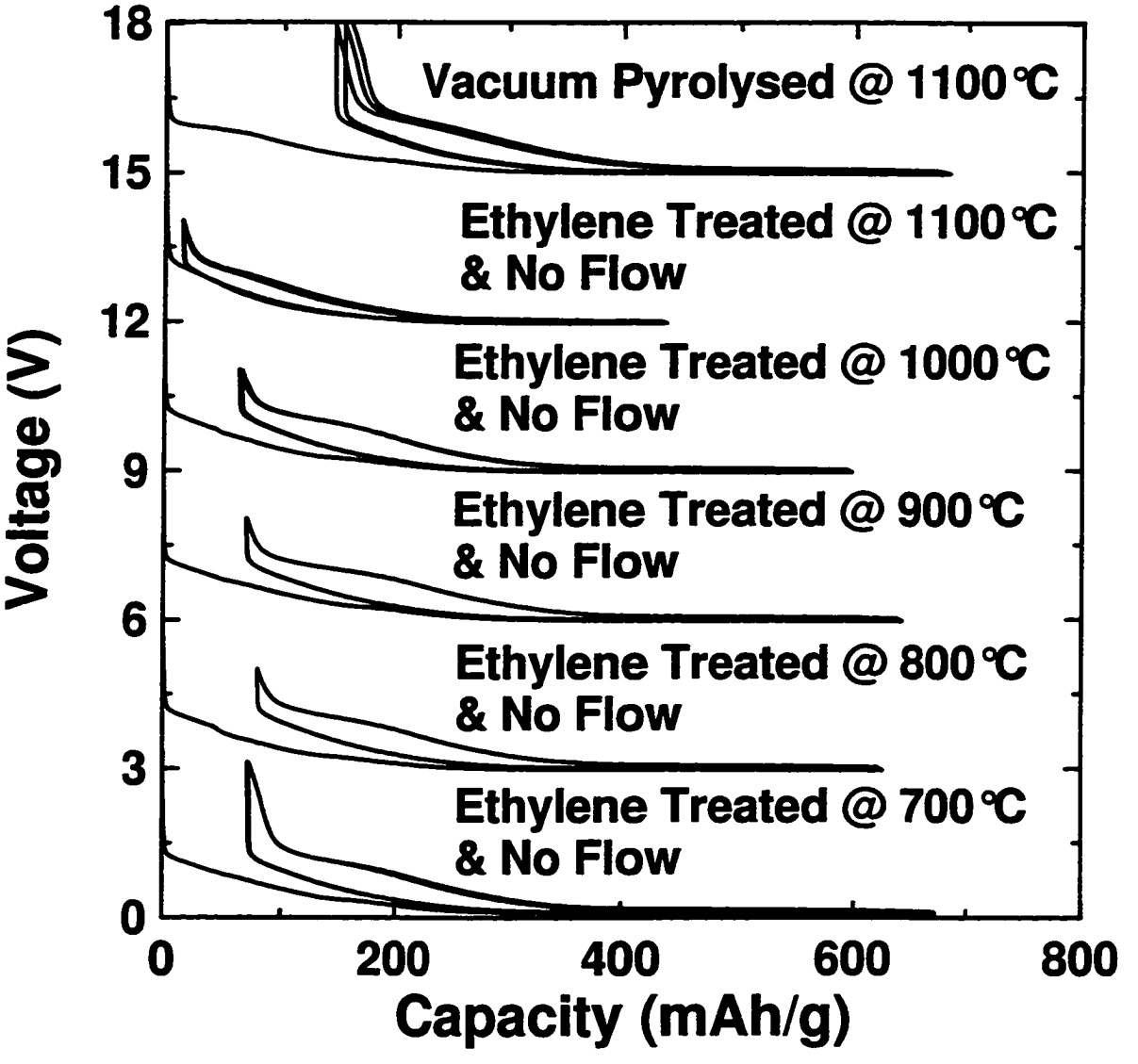

Figure 6.3: Voltage-Capacity profiles for the samples treated with a single dose of ethylene after vacuum pyrolysis and vacuum pyrolysed to 1100 C. Curves have been shifted sequentially by 3 V for clarity.

shows that the samples exposed to ethylene at temperatures between 700°C - 1100°C show a reduction in irreversible capacity to about 70 mAh/g. The sample heated for 12 hours in ethylene showed the greatest reduction in irreversible capacity but also showed signs of reversible capacity loss associated with prolonged exposure at high temperatures. This loss of reversible capacity is associated with micropore closure and is the topic of the next chapter.

During the first discharge there is a long plateau in the voltage profile at about 1-0.8 V that is not seen during subsequent discharge processes. This plateau is responsible for the majority of the irreversible capacity in hard carbon believed to result from air exposure [4, 6]. This plateau corresponds to a peak in the derivative curve at about 1-0.8 V as shown in figure 6.4. The vacuum pyrolysed sample shows a large peak, during the first discharge, corresponding to the large irreversible capacity of this material. The ethylene treated sample shows a smaller peak during the first discharge which is correlated to a lower irreversible capacity. Interestingly, the CVD material shows no peak in the range 1-0.8 V during the first discharge and has a lower irreversible capacity than any of the hard carbon material studied thus far (27 vs. 220 mAh/g for the vacuum pyrolysed sample). It does show some peaks at lower voltage and the origins of these peaks are unknown and seem to present in the vacuum pyrolysed sample as well.

These results show strong evidence that the carbonaceous material deposited from ethylene gas forms a material that does not react with air as does hard carbon. Consequently, it does not suffer from the large irreversible capacity and can be used to reduce the irreversible capacity in hard carbon depending on how much of the surface is covered by the CVD material.

6.1.4 BET Surface Area

The BET surface areas, listed in Table 1, tend not to be well correlated to the irreversible capacities except for the vacuum pyrolysed and ethylene pyrolysed samples with the same HTT. These samples show a reduction in irreversible capacity from

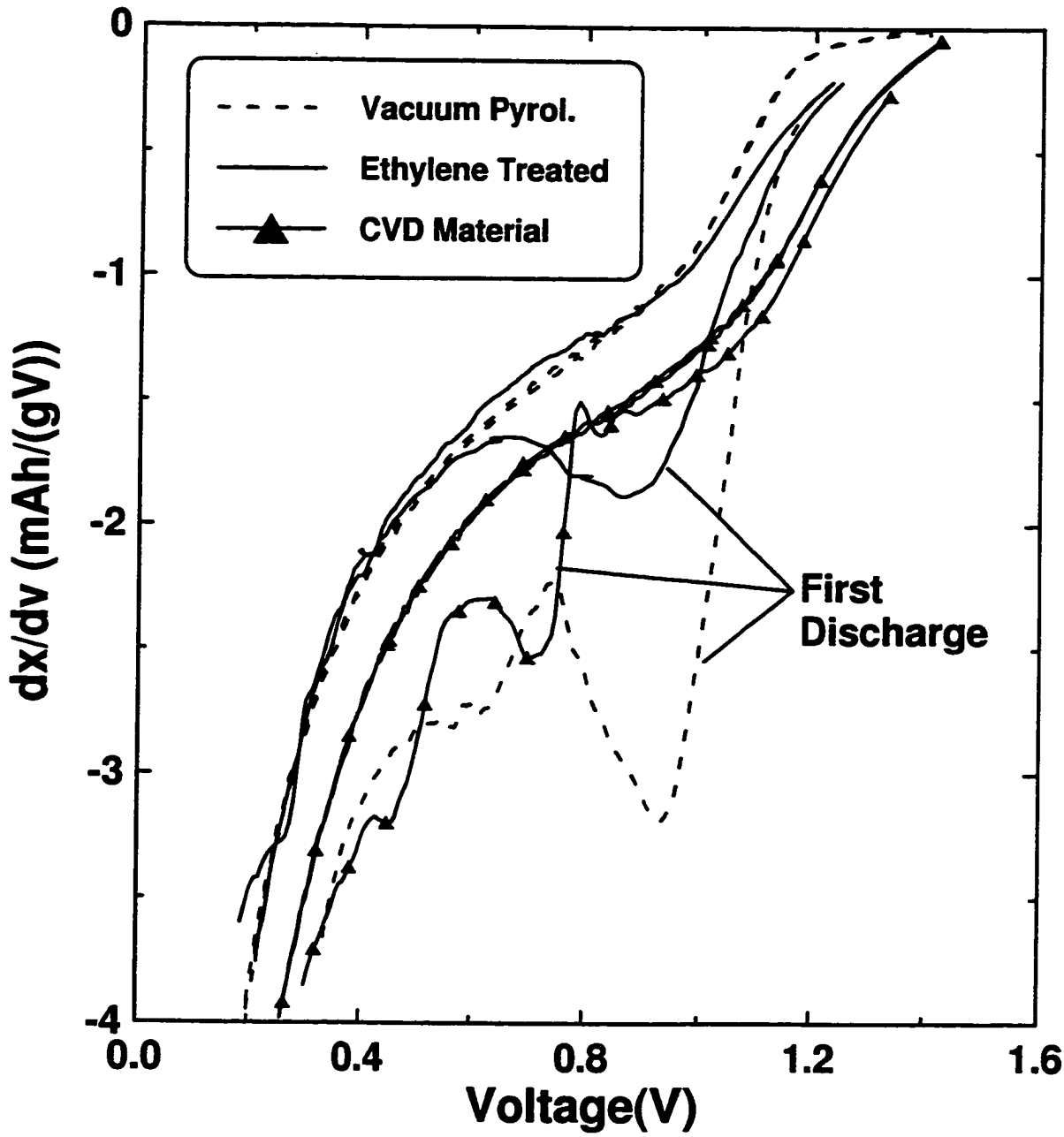

Figure 6.4: The differential capacity versus voltage for vacuum pyrolysed sucrose to 900°C, sucrose pyrolysed in ethylene to 900°C and the electrode prepared by the CVD of carbon on nickel foil (from ethylene gas) at 900°C. The first discharge is indicated on the graph.

220 to 52 mAh/g and in BET surface area from 251 to 22 m^2/g after being ethylene treated. This reduction in surface area is naturally correlated to the irreversible capacities associated with both the SEI layer and adsorption/formation of surface functional groups. All other samples were vacuum pyrolysed to 1100°C and at this temperature the BET surface area drops dramatically and is very sensitive to pyrolysis conditions. The surface areas of these samples are not correlated to the ethylene treatment and thus not correlated to the irreversible capacity. Hence the ethylene treatment does not reduce the irreversible capacity by simply reducing the surface area.

6.1.5 WAXS

Wide angle X-ray scattering experiments show that samples treated with ethylene at temperatures greater than 700°C begin to exhibit a soft carbon phase. In figure 6.5, the sample pyrolysed directly in ethylene shows a much more pronounced 002 peak when compared to the vacuum pyrolysed sample. This is indicative of the soft carbon phase deposited on the surface as shown in the top panel. In figure 6.6, the sample treated with flowing ethylene at 700°C begins to show the signs of a graphitic phase whereas the sample treated at 500°C does not. The presence of this graphitic phase is correlated to the reduction of irreversible capacity which is evident between the samples shown in figure 6.2.

The samples treated with a single dose of ethylene, shown in figure 6.7, also show the appearance of a graphitic phase but only at temperatures above 900°C. This delay in the appearance of a graphitic phase between samples treated with flowing ethylene and the single-dose methods is likely due to a lack of available ethylene. The single-dosed sample at 700°C still shows the low irreversible capacity even though the graphitic phase is not visible in the WAXS data. Assuming the intensity of the graphite peak is proportional to the amount of deposited carbonaceous material, only a very small amount of ethylene is required to reduce the irreversible capacity and substantial build up of the carbonaceous material on the surface is not needed. Hence,

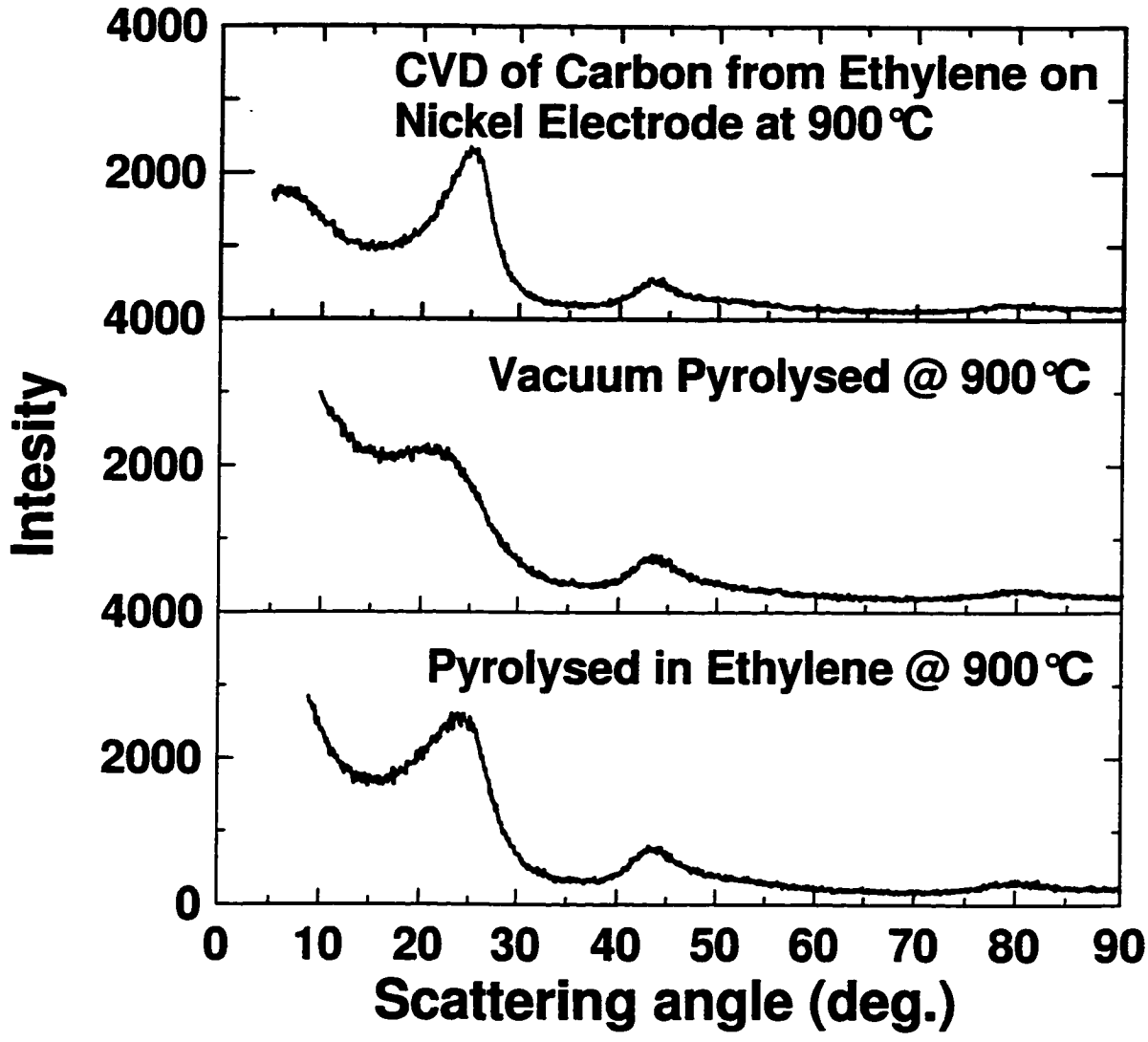

Figure 6.5: Comparison of the WAXS curves measured for the sample which was vacuum pyrolysed to 900°C and pyrolysed in ethylene to 900°C.

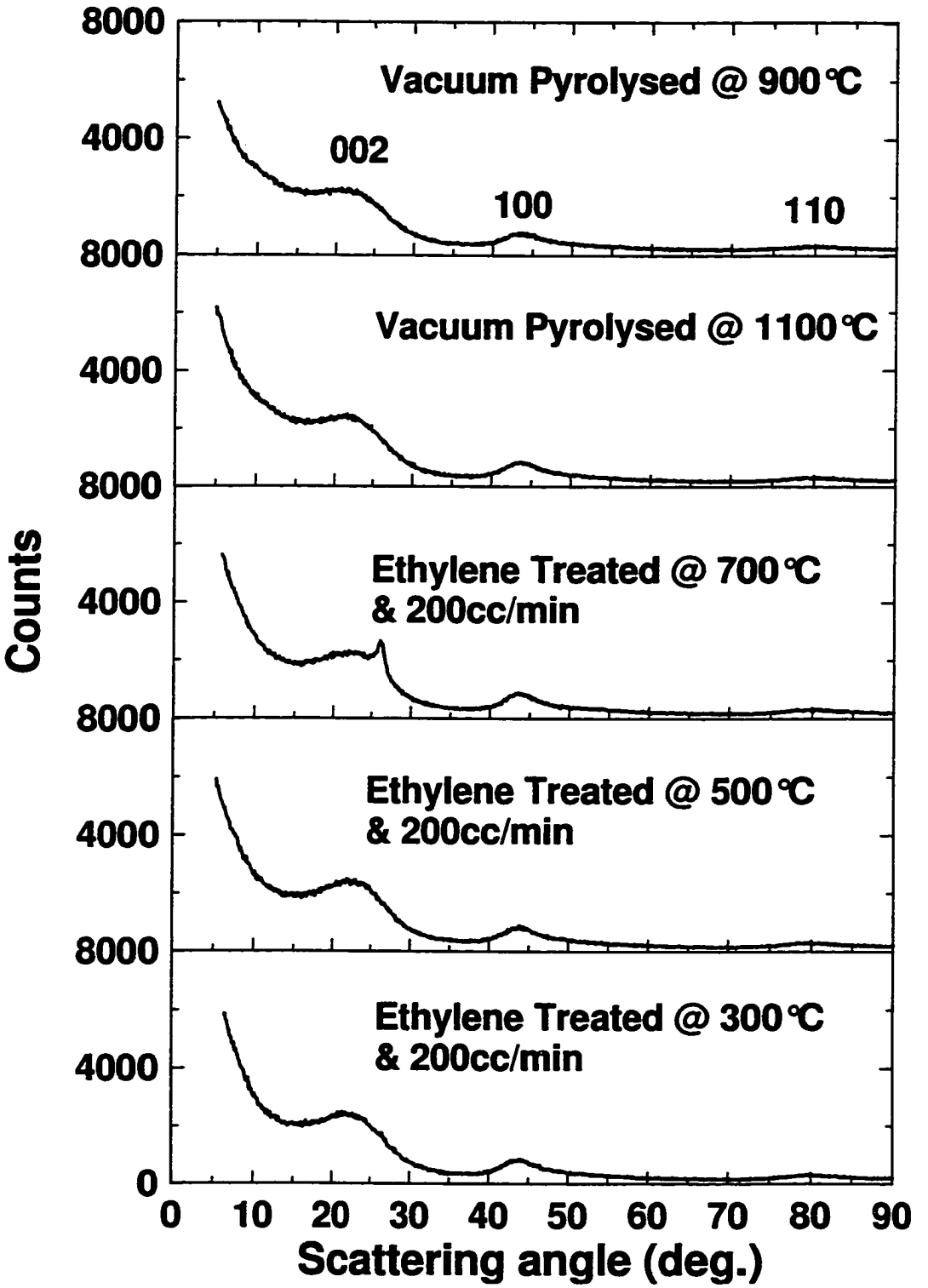

Figure 6.6: WAXS curves for samples pyrolysed to 1100°C in vacuum and then treated with ethylene to varying degrees, mainly with an ethylene flow of 200 cc/min..

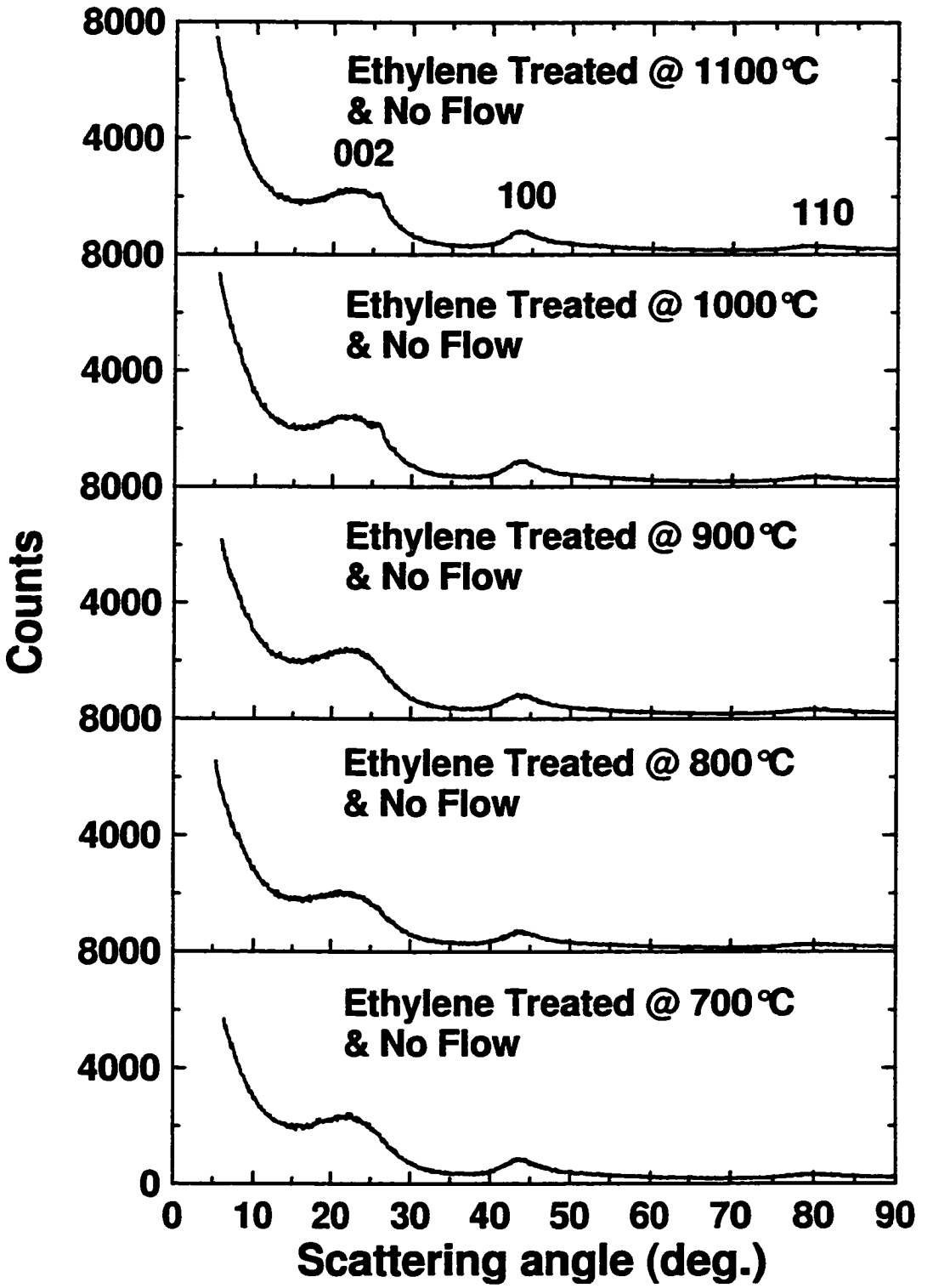

Figure 6.7: WAXS curves for samples pyrolysed to 1100°C in vacuum and then treated with a single dose of ethylene and heated to various temperatures.

it is possible to maximize the reduction in irreversible capacity without building up too much soft carbon on the surface as to increase the observed hysteresis. This explains why the hystereses in the voltage profiles, shown in figures 6.2 and 6.3, do not change.

6.1.6 SAXS

SAXS studies show that the internal pore structure of these materials depends on the heat treatment temperature and not the degree of ethylene treatment as shown in figure 6.8. The vacuum and ethylene treated samples to 900°C and show almost identical scattering curves and micropore size even though one was vacuum pyrolysed and the other was not. Subsequently, all samples were pyrolysed to 1100°C and show similar scattering curves. From this we can conclude that the ethylene treatment does not affect the internal pore structure of the material and it's effects are likely limited to the surface of the sample.

6.1.7 XPS

XPS measurements show that the surfaces of the samples are almost entirely carbon with very small evidence for the presence of oxygen. The O_1S peak is only barely visible for the non-treated sample and even less detectable for the treated sample (see figure 6.9). It is difficult to determine whether such a small difference in oxygen content on the surface of the carbon could produce the dramatic differences in irreversible capacity shown in figure 1. Alternatively, if the mechanism for the irreversible capacity is adsorption (possibly of water or oxygen) then these species would desorb in the UHV chamber and not be detected by the XPS measurements.

6.1.8 CO_2 Gas Adsorption Studies

CO_2 gas adsorption studies essentially show that the surface properties of the samples are not significantly changed by ethylene treatment. The adsorption isotherms were

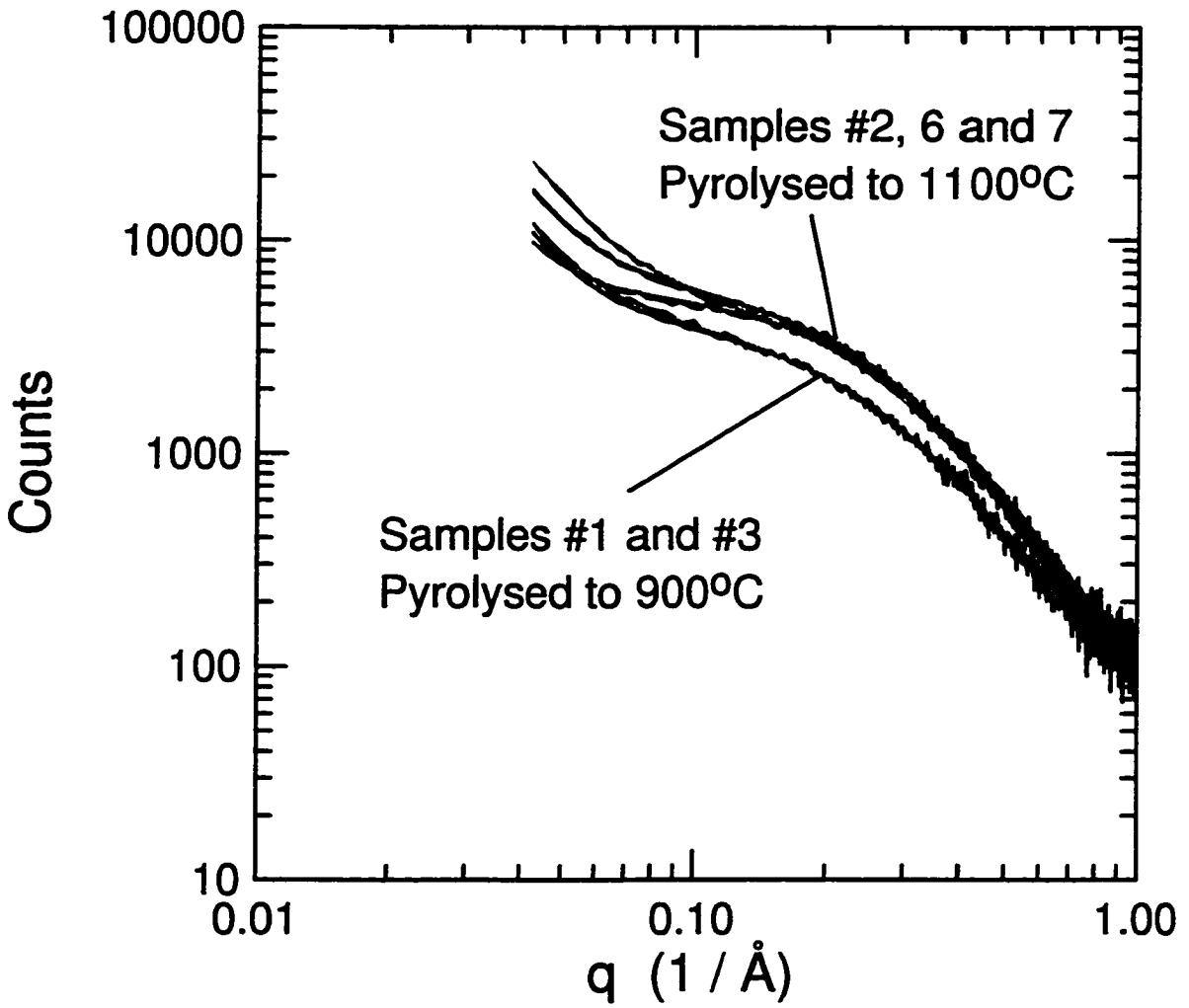

Figure 6.8: SAXS measurements for various samples pyrolysed to either 900°C or 1100°.

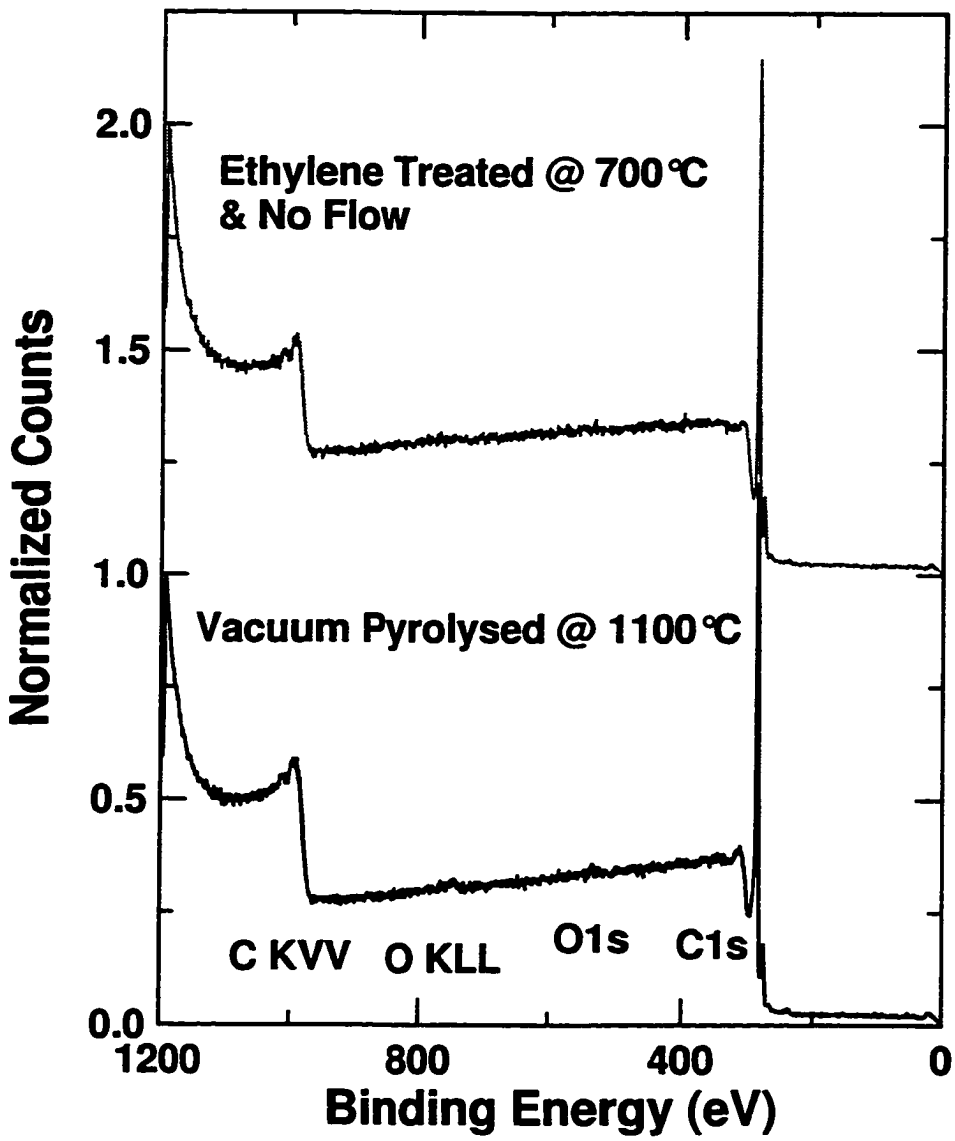

Figure 6.9: XPS studies of the sample pyrolysed to 1100°C and treated with ethylene at 700°C and the vacuum pyrolysed sample to 1100°C.

measured for the two control samples and three ethylene treated samples; namely the sample pyrolysed in ethylene to 900°C, the sample ethylene treated at 700°C with 200cc/min and the sample ethylene treated at 700°C with no flow. The adsorption isotherms are shown in figure 6.10.

The adsorption isotherms for the majority of the ethylene treated samples are only slightly lower than the vacuum pyrolysed samples. When only a small amount of ethylene was deposited on the surface for the no-flow sample, the adsorption isotherm is only slightly lower than the vacuum pyrolysed sample and also shows a small amount of hysteresis. The sample treated with 200 cc/min of ethylene shows slightly lower adsorption and the sample pyrolysed in ethylene, giving the largest amount of carbonaceous deposition, showed a significant decrease in adsorption; consistent with BET surface area measurements. These results seem to indicate that the ethylene treatment is modifying the surface of the hard carbon however it is not destroying the micropore structure or significantly decreasing the surface area of the sample and hence these small changes in structure are unlikely to explain the large changes in irreversible capacity. These changes are more likely to result in a change in surface chemistry that results from the small amount of soft carbon deposited on the surface which resists the influences of air.

6.1.9 Conclusion of Ethylene Treatment

Samples treated with ethylene during/after pyrolysis, at temperatures above 700°C, show a dramatic reduction in the irreversible capacities without a detectable change in the voltage profile. In our model where two independent components contribute to the irreversible capacity, we believe that the ethylene treatment either greatly reduces or eliminates the component caused by exposing the sample to air. These samples show almost identical internal micropore structure when compared by SAXS measurements. WAXS measurements show that samples treated with ethylene above 700°C begin to show the presence of a soft carbon phase that is presumably forming on the surface of the sample. WAXS and electrochemical data suggest that only a very

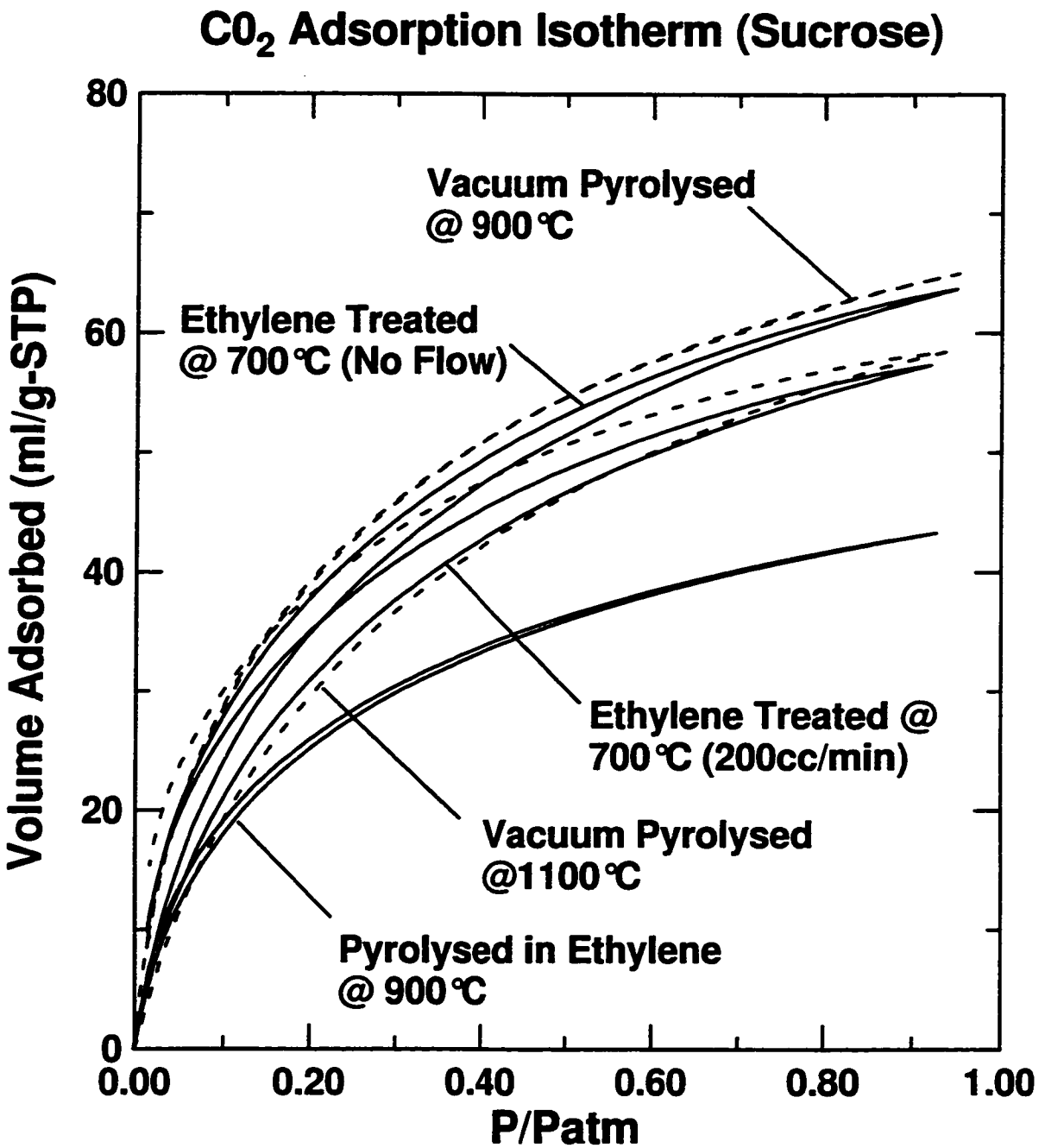

Figure 6.10: CO_2 gas adsorption isotherms for the specified samples.

small amount of carbonaceous deposition, undetectable by WAXS measurements, is required for the reduction in irreversible capacity. BET surface area measurements for the samples pyrolysed under vacuum and in ethylene to 900°C seem to correlate the surface area to the irreversible capacity but all other samples do not show such a correlation. XPS studies have shown that the surfaces of the carbon electrodes are almost entirely pure carbon. The lack of evidence for the presence of oxygen-rich surface functional groups suggests that some component of air adsorb in the pores of the sample. It may react with lithium during the first discharge to produce the large irreversible capacities characteristic of untreated hard carbons. Adsorbed species may be removed by the UHV system of the XPS analyser and hence go undetected. In conclusion, the ethylene treatment described here is successful in reducing the irreversible capacity caused by exposing hard carbons to air which we believe is more likely due to surface adsorption than the formation of surface functional groups.

One important question arises if the mechanism is surface adsorption: why would the ethylene treatment reduce the adsorption of air but not CO_2? This can be explained by the differences in the interaction of different molecules with the surface. For example, the ethylene treatment deposits a carbonaceous material containing hydrogen. From SAXS, the micropores are not destroyed and CO_2 can still adsorb in them. However, the deposited hydrogen-rich carbon layer may cause the surface to become hydrophobic and thus prevent the adsorption of water on the surface. This would tend to agree with the difference between saturated and unsaturated fats. Unsaturated fats contain carbon double bonds and are more hydrophilic than saturated fats that are formed by hydrogenating the C=C groups in the former. Thus, when hydrogen is added to an unsaturated fat to produce a saturated fat, the molecule becomes more hydrophobic. If the same is true for hard carbon, then adding hydrogen to the surface may simple reduce the number of C=C groups causing the surface to become more hydrophilic. Since the underlying structure is not significantly changed, CO_2 adsorption remains essentially the same.

6.2 Irreversible Capacity Reduction by Improved Dewatering Methods

6.2.1 Sample Preparation and Experimental Results

Lowering the dewatering temperature is correlated to a decrease in the irreversible capacity in hard carbon. Samples were prepared by dewatering sucrose at temperatures between 135°C and 190°C and subsequently pyrolysing to 1050°C in vacuum. The electrodes were prepared in the usual way and standard WAXS, SAXS and BET measurements were performed on the samples. The results of these experiments are tabulated in table 6.2.

The results of electrochemical testing are shown in figure 6.11. Lowering the dewatering temperature significantly decreases the irreversible capacity. WAXS and SAXS measurements on the samples (shown in figures 6.12 and 6.13 respectively) do not show any changes in the bulk properties of the samples. CO_2 gas adsorption experiments were also unable to detect any differences in the surface properties of the samples. In figures 6.14 and 6.15 the adsorption isotherms and kinetics of adsorption data are shown for the three samples. All show identical behaviour for CO_2 adsorption and suggest that the micropore structure is only dependent on the final HTT and not on the dewatering process. Gas adsorption studies also show no sign of burn-off

De-H_2O Temp. (°C) $\pm 10°C$	Yield After De-H_2O $\pm 1\%$	Yield After Pyrol. $\pm 1\%$	BET SA (m^2/g) $\pm 5\%$	R ± 0.05	R_g (Å) ± 5Å	IRREV. Capacity (mAh/g) $\pm 5 mAh/g$	REV. Capacity (mAh/g) $\pm 10 mAh/g$
140	93%	23%	40	1.88	6.61	67	555
155	87%	24%	9.0	1.94	6.98	93	520
170	66%	24%	16	1.88	6.66	102	560

Table 6.2: Measured parameters of sucrose samples dewatered and pyrolysed to the specified temperatures.

that may have been present if prolonged dewatering at higher temperatures lead to the oxidation of the samples surface. It is possible that some type of burn-off is still present but that it does not affect the surface structure enough to be detected by the CO_2 gas adsorption studies presented here. This would be consistent with the results of oxidation shown by Xue et. al. [42] which showed that even the most limited burn-off can cause a dramatic increase in irreversible capacity, a decrease in reversible capacity and generally has a very negative effect of the shape of the voltage profile.

6.3 TGA Analysis

TGA studies were used to determine the amount of adsorbates on the surface of the samples. Thermal gravimetric analysis is the heating of a sample in a controlled environment while monitoring the mass of the sample. Hard carbon samples exposed to air for different periods of time were analysed in argon gas to temperatures of 900°C and show a substantial decrease in mass beginning at temperatures of about 100°C (see figure 6.16) [4]. This decrease in mass is more pronounced with longer exposure times to air and occurs at temperatures much lower than the ignition point for hard carbon (≈400°C). Judging by the temperature and the dependence on exposure time, this observed mass loss in very likely the adsorption/desorption of water or carbon dioxide on the surface. This strongly suggests that the second contribution to the irreversible capacity (observed in hard carbon) is the reaction of lithium with water adsorbed on the surface or in the micropores of the sample to form lithium hydroxides.

TGA studies of various samples with differing amounts of irreversible capacity are correlated to a loss in sample mass in the temperature range 100-500°C (figure 6.17). The samples have been heat treated to 900°C and thus the observed mass loss is more likely the desorption of adsorbed species on the surface of the samples. The ethylene treated sample, showing the lowest irreversible capacity, shows the smallest mass loss

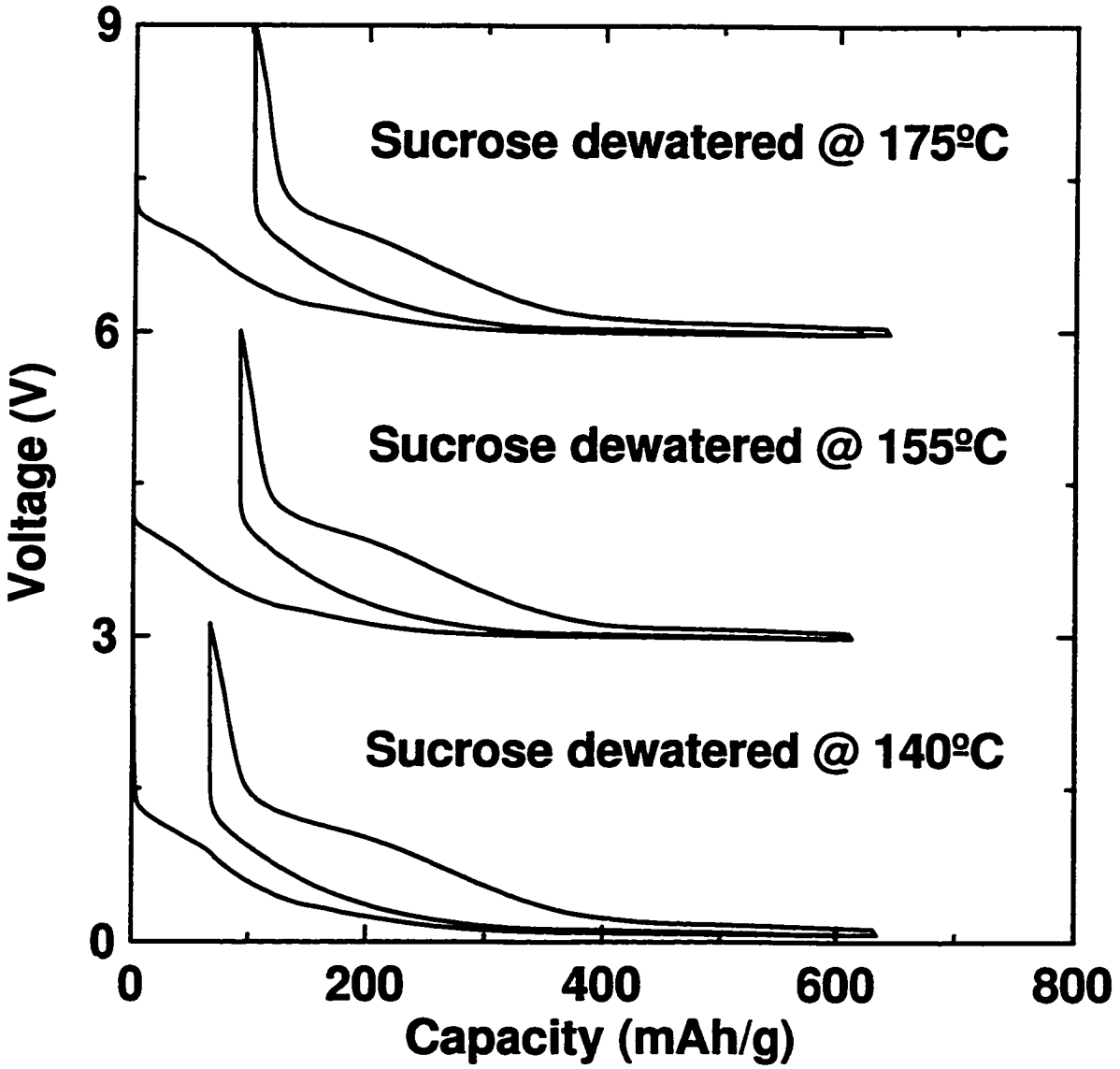

Figure 6.11: Voltage profiles of sucrose dewatered to the specified temperature followed by vacuum pyrolysis to 1050°C.

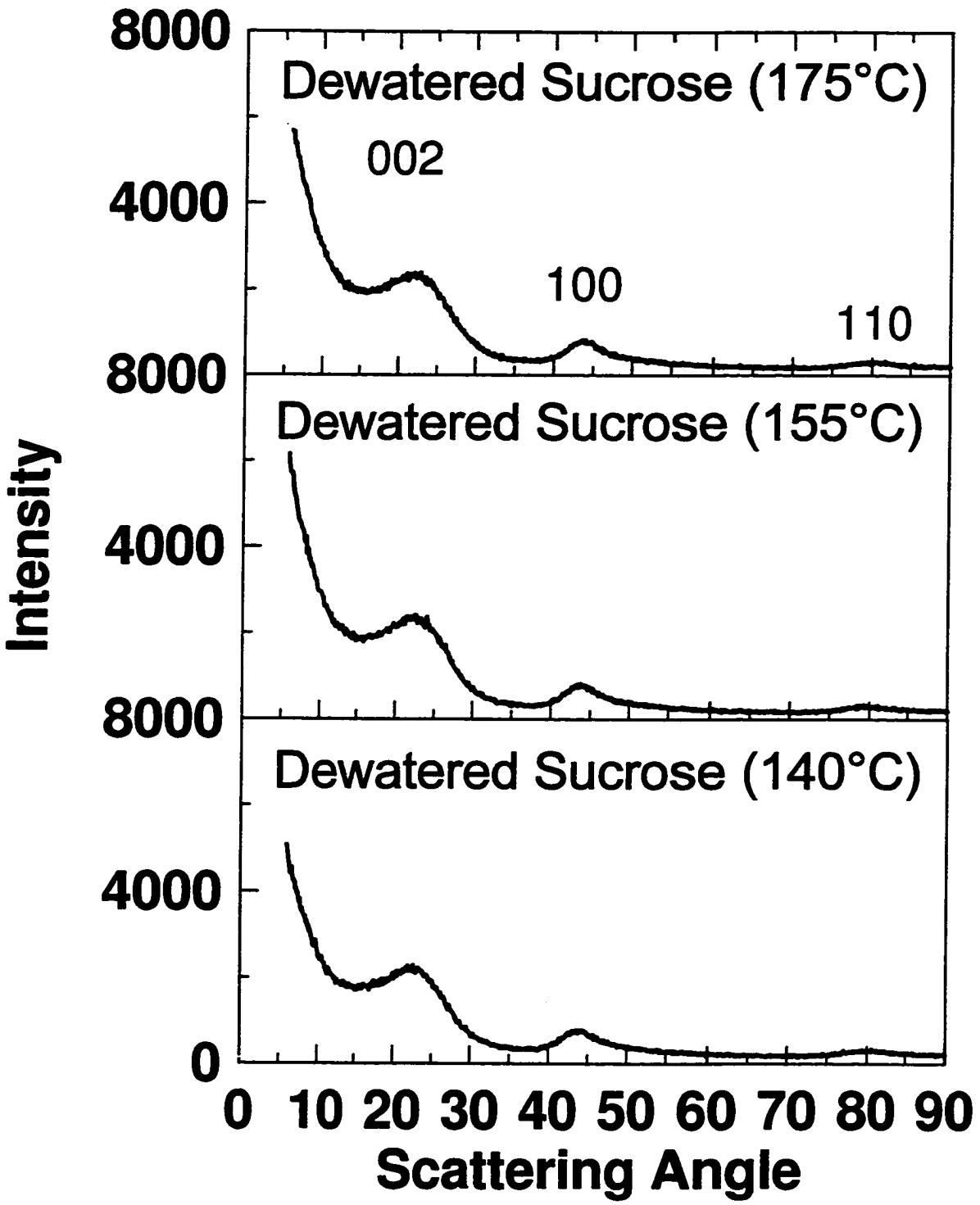

Figure 6.12: WAXS measurements of samples prepared from sucrose dewatered to the specified dewatering temperature followed by vacuum pyrolysis to 1050°C.

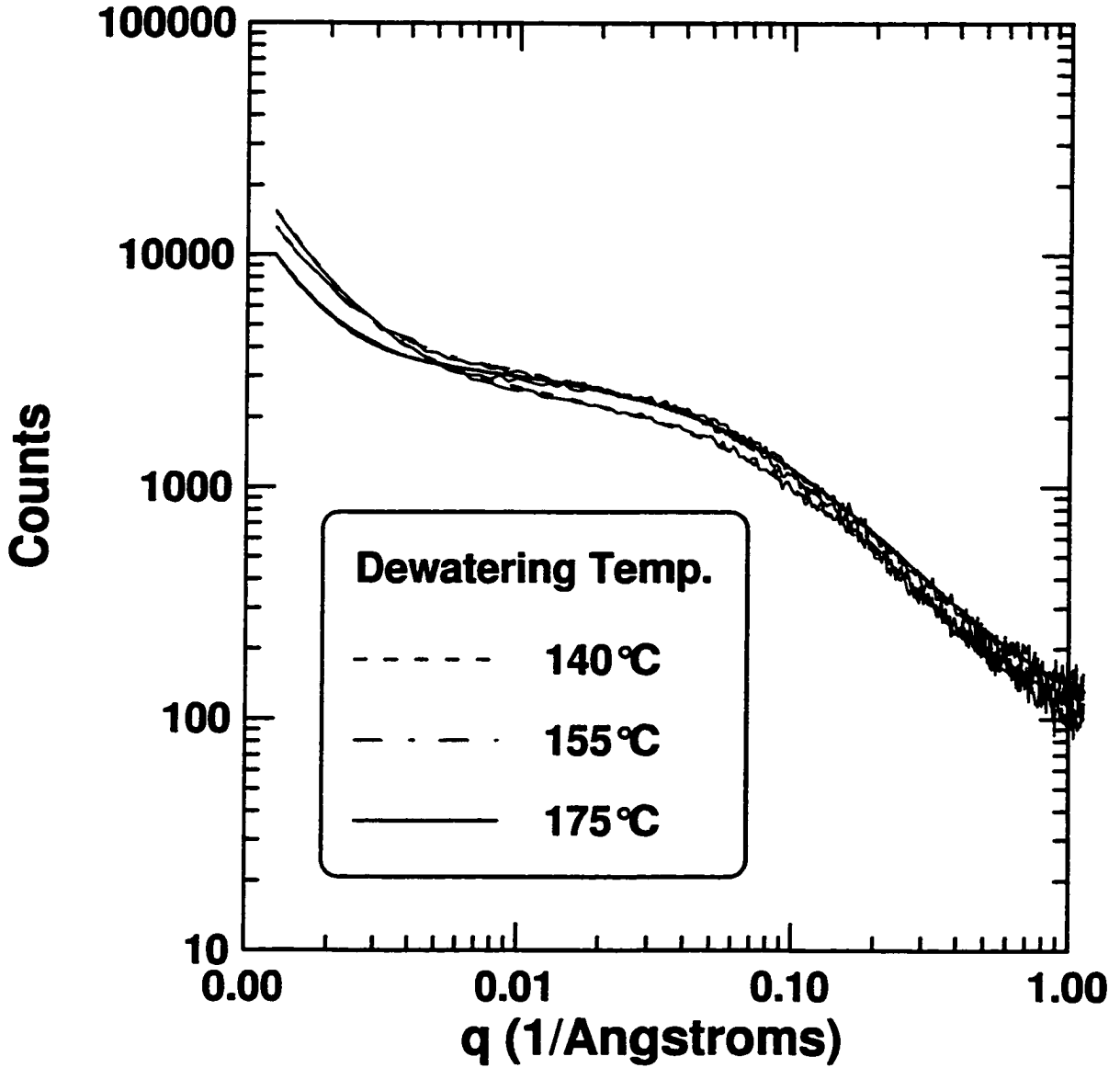

Figure 6.13: SAXS measurements of samples prepared from sucrose dewatered to the specified dewatering temperature followed by vacuum pyrolysis to 1050°C. The smooth lines, shown in the legend, represent the fitted curves to the data.

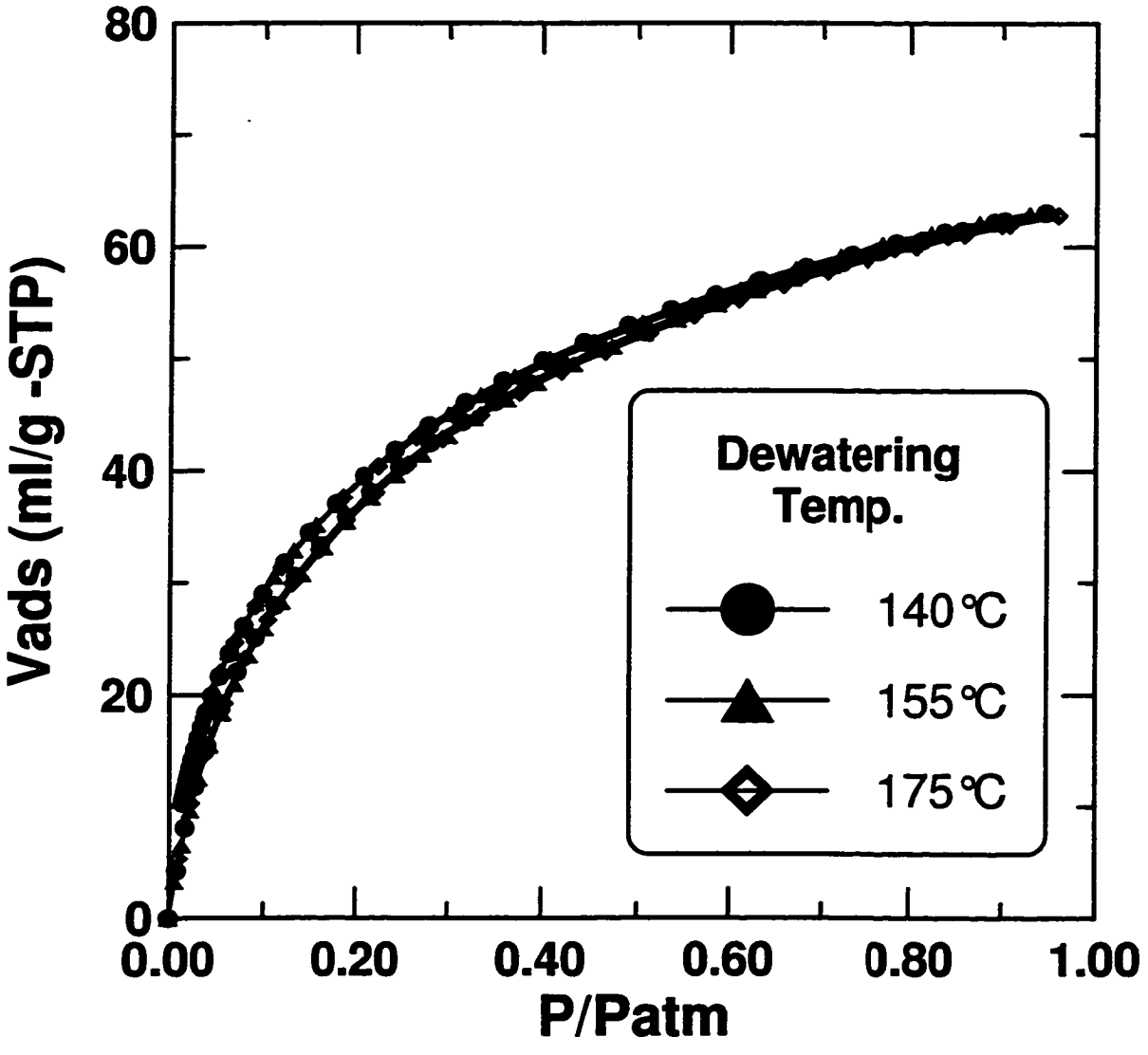

Figure 6.14: CO_2 adsorption isotherms for samples dewatered at the specified temperatures and subsequently pyrolysed to 1050°C.

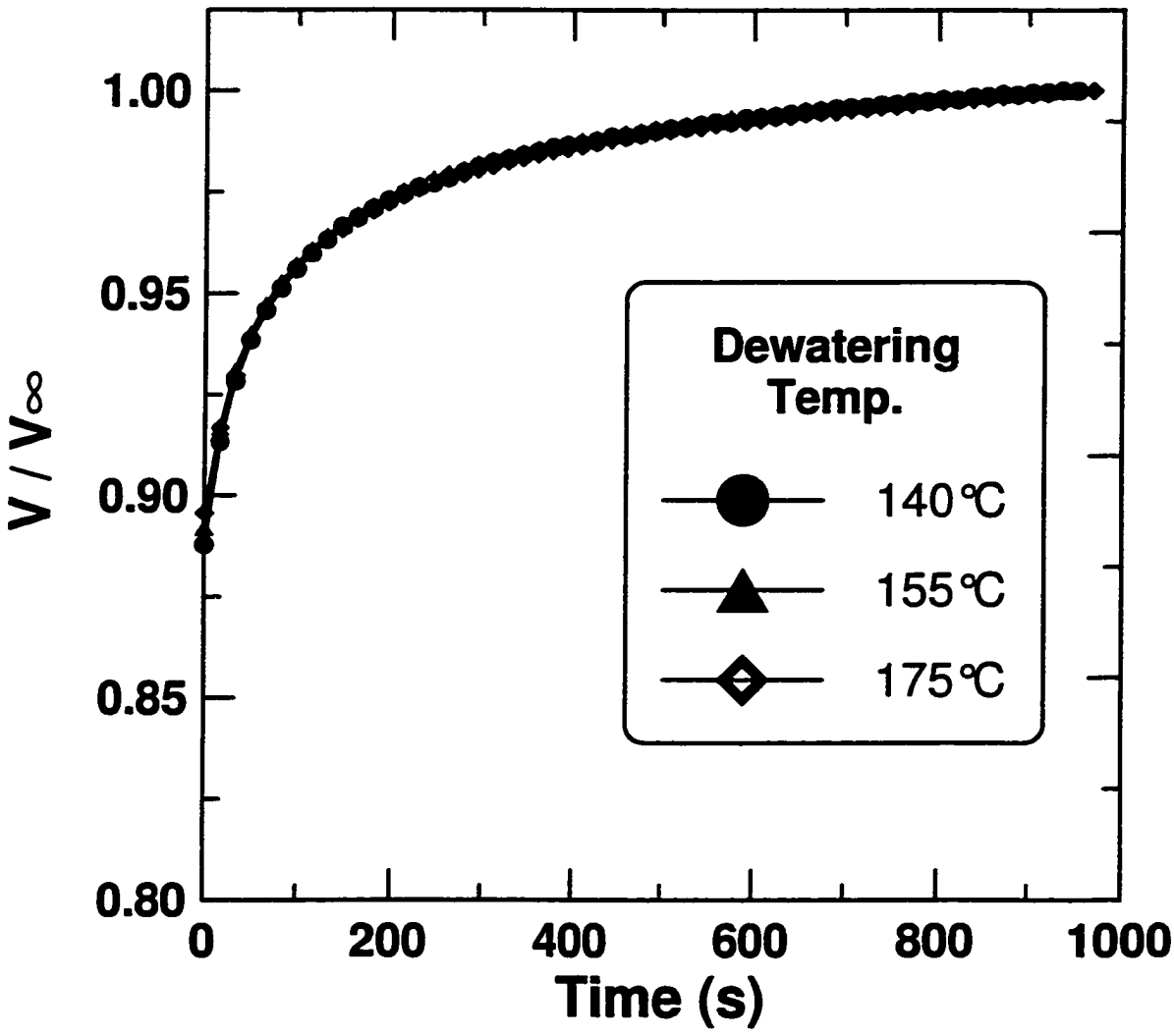

Figure 6.15: CO_2 adsorption kinetics for samples dewatered at the specified temperatures and subsequently pyrolysed to 1050°C.

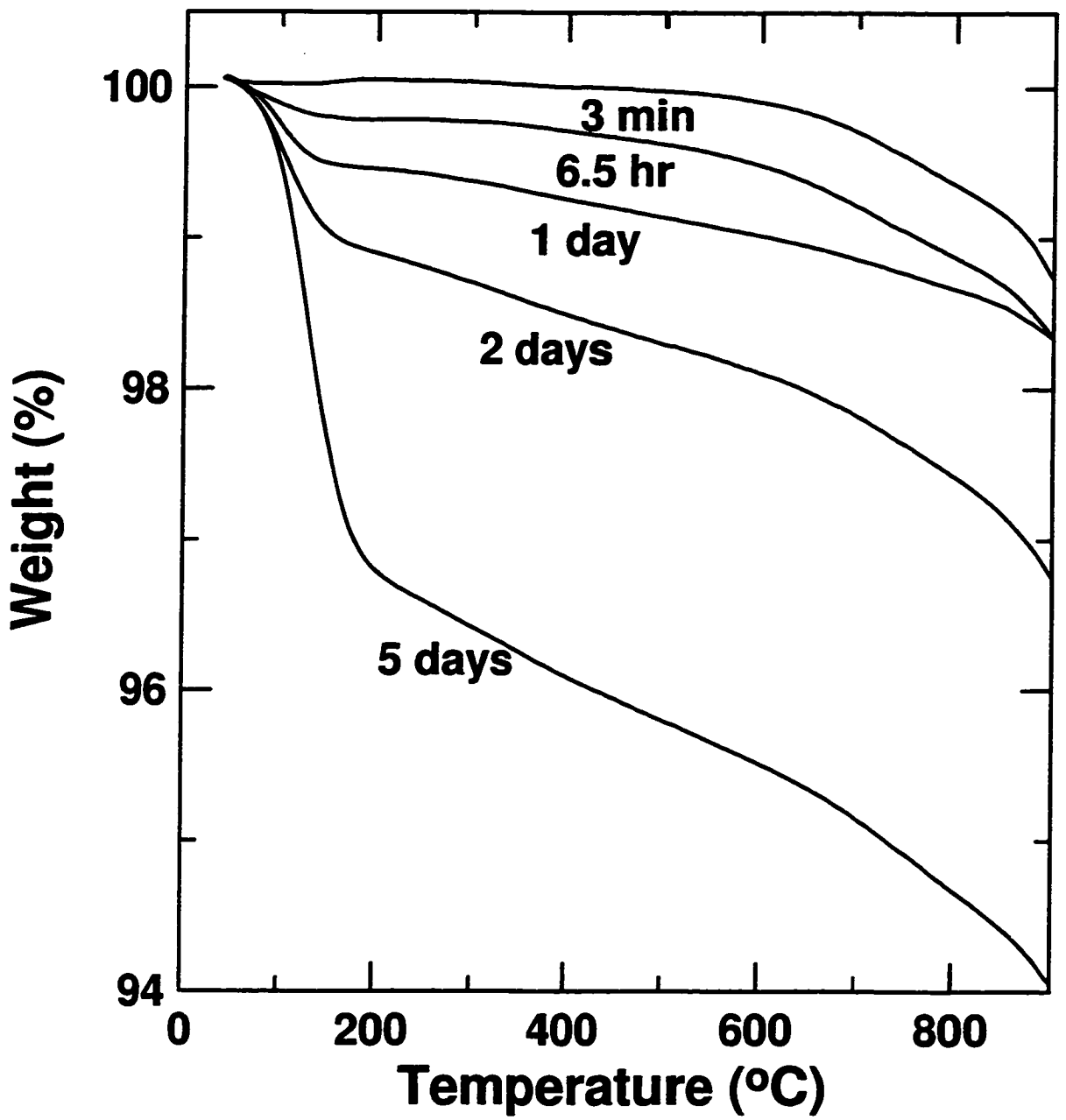

Figure 6.16: Thermal gravimetric analysis (TGA) of sugar carbon tablets under argon gas. The tablets had been pyrolysed at 1050°C and exposed to air for different periods of time as indicated before the TGA measurements. [4]

and hence the lowest affinity for adsorption. All other samples show increasing mass loss with increasing irreversible capacity. These results give strong evidence that the large irreversible capacity in hard carbon results from the adsorption of air.

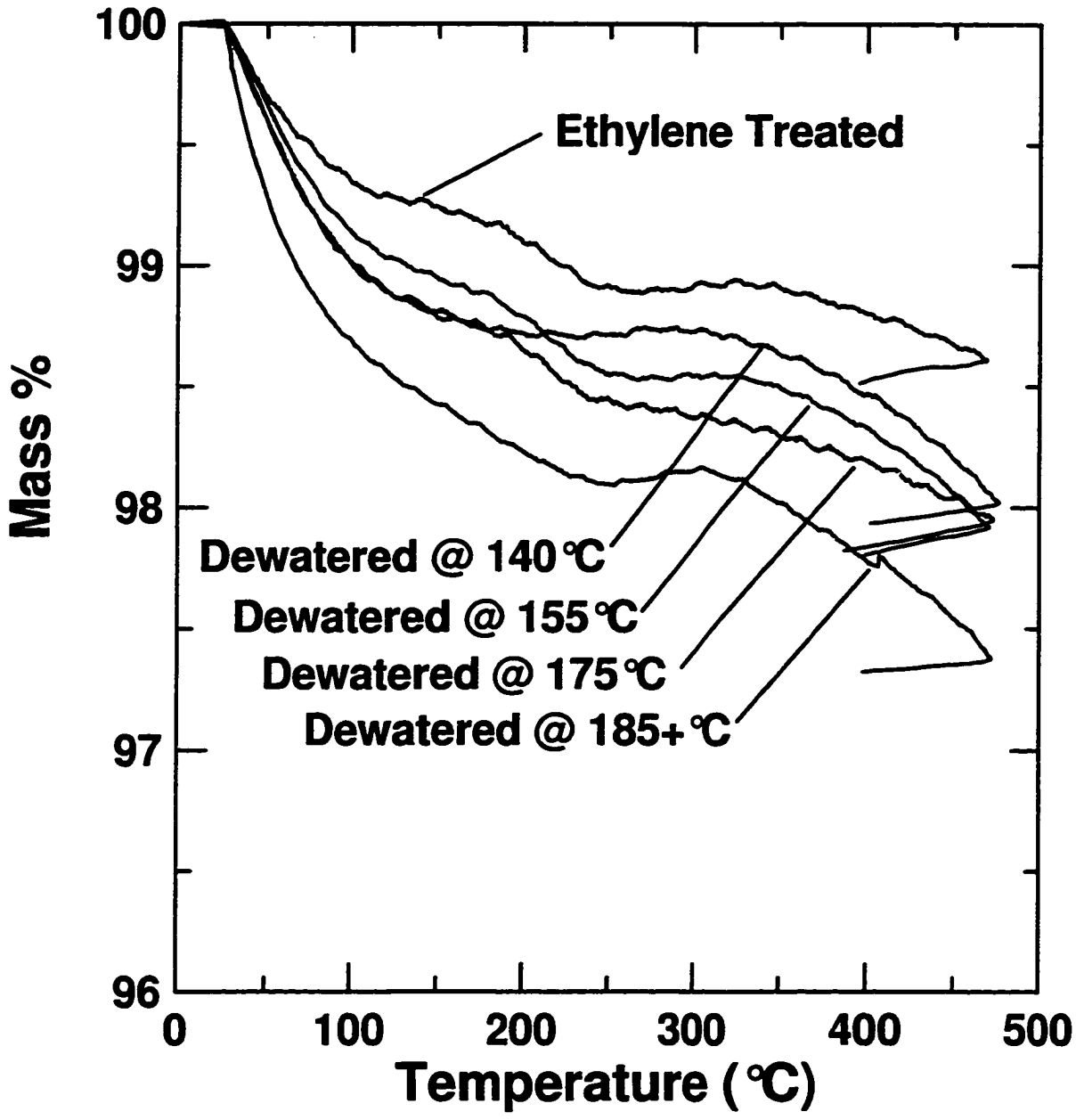

Figure 6.17: Thermal gravimetric analysis (TGA) of various samples with different irreversible capacity prepared from pyrolysed sucrose.

6.4 Conclusion

In this chapter the irreversible capacity in hard carbon has been studied and two methods have been described to reduce the irreversible capacity. This work has led to hard carbons with irreversible capacities that are similar to other anode materials such as MCMB. Both the ethylene surface treatment and dewatering temperature experiments suggest that the irreversible capacity is correlated to the surface of the hard carbon sample.

For the ethylene treatment, the deposited carbonaceous layer somehow inhibits the formation of surface functional groups or the adsorption of some species of air into the micropores of the sample. This dramatically decreases the component of the irreversible capacity associated with air exposure from greater than 150 mAh/g to less than 50 mAh/g for certain treatment procedures. XPS studies showed that the surface was essentially pure carbon with no evidence for surface functional groups and thus it is likely that adsorption plays a more important role.

A careful study of the dewatering process has shown that reducing the dewatering temperature significantly decreases the irreversible capacity. For all intents and purposes we were unable to correlate the irreversible capacity to changes in the bulk properties, as measured by WAXS and SAXS, or the surface properties, as measured by BET surface area and CO_2 gas adsorption studies.

TGA analysis provides considerable evidence that adsorption of air on the surface of the sample is responsible for the observed trends in irreversible capacity. In fact, the mass loss during heating to 500°C, believed to result from desorption, has been correlated to the irreversible capacity.

Chapter 7

Reversible Capacity Loss with Increased HTT

The large reversible capacity of hard carbon makes it a very attractive material to study with good potential for use in commercial applications. The small hysteresis in the voltage profile degrades real cell performance and has been correlated to the residual hydrogen content[77] after pyrolysis ($< 0.5\%$ by mass). In order to reduce the hydrogen content, one would simply heat the materials to higher temperatures during pyrolysis. However, there is a critical temperature above which the hard carbon begins to show a loss in reversible capacity. More specifically, this capacity loss occurs in the low voltage region sometimes referred to as the low voltage plateau in hard carbon. This plateau is likely due to the adsorption of lithium in the micropores found in hard carbon. As our experimental results will suggest, the loss in capacity is due to the closing of these micropores.

In this chapter, a series of samples pyrolysed to different temperatures, showing a range of capacity loss and micropore closure, were synthesized. These samples were characterised by WAXS, SAXS, BET surface area and CO_2 gas adsorption measurements. An adsorption model based on the Langmuir equation is used to calculate the voltage profile and differential capacity in order to develop a qualitative understanding of the low voltage plateau in hard carbon. Furthermore, a model for micropore

closure is also developed to predict the number of open micropores as a function of the heat treatment temperature and exposure time.

7.1 Sample Preparation

A series of samples was prepared from dewatered sucrose pyrolysed at temperatures between 900 and 1400°C in argon gas. This temperature range is chosen for a number of reasons:

1. 1400°C is near the limit of practical tube furnace operation and induction furnaces would be required for higher temperatures.

2. This temperature range corresponds to the region where hard carbon shows large reversible capacity and low hysteresis and hence has the highest commercial value.

3. Hard carbon begins to show capacity loss at 1100°C and thus the range from 900 to 1400°C is appropriate for studying this phenomena.

After these samples were pyrolysed, electrodes were prepared and electrochemically tested.

7.2 Electrochemical Testing

The results of electrochemical testing are tabulated in table 7.1 and shown in figure 7.1. By observation, the hysteresis in the voltage profile and irreversible capacity decreases as the HTT increases. The reversible capacity remains essentially constant up to about 1100°C and then begins to decrease with increased HTT. By observation, this capacity loss is most pronounced in the low voltage region of the voltage profile.

In figure 7.2, the differential capacity is plotted versus voltage to elucidate the capacity at low voltage. The vertical lines at -0.02 and 0.02 V represent the plating and stripping of lithium metal on the surface of the carbon anode respectively. For

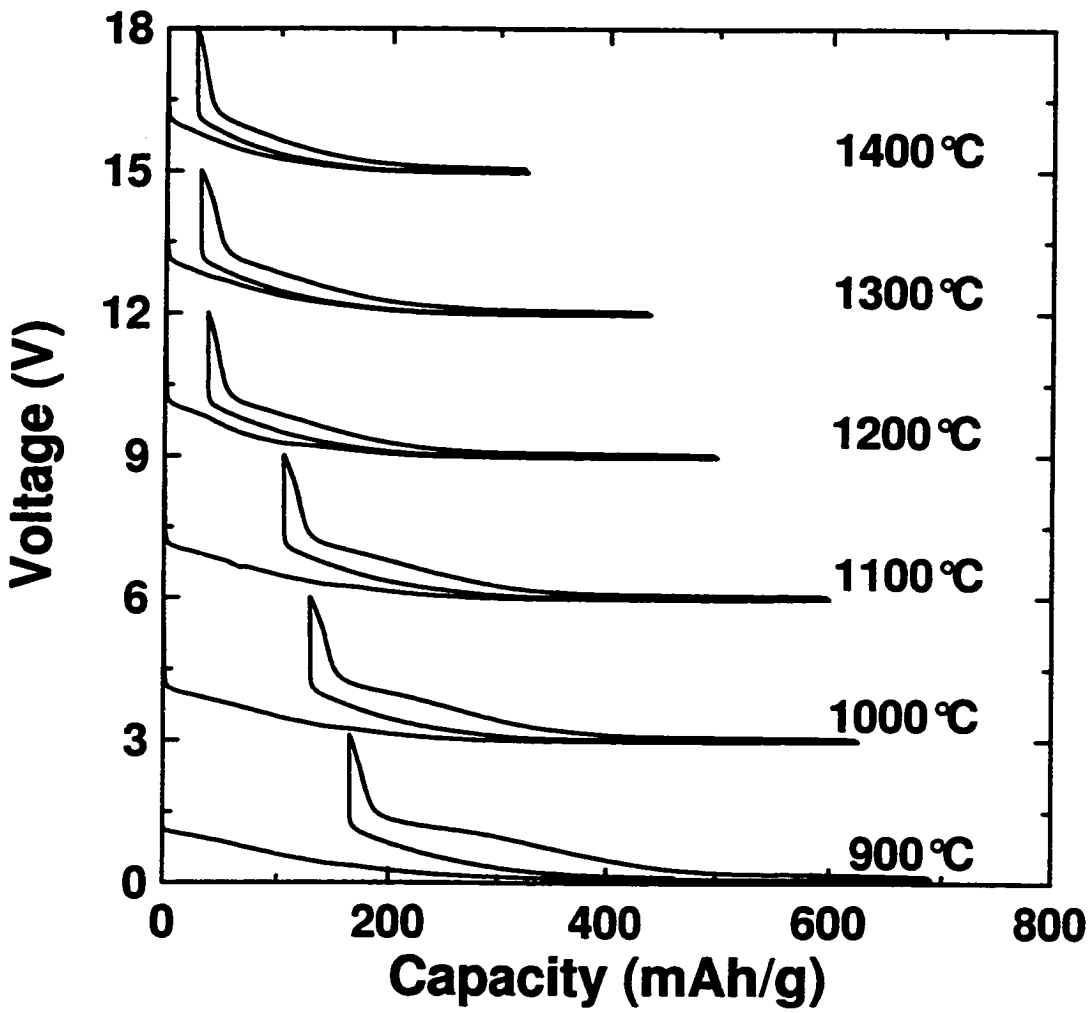

Figure 7.1: Voltage profiles of hard carbon prepared by pyrolysis of sucrose in argon gas. Heat treatment temperatures are indicated.

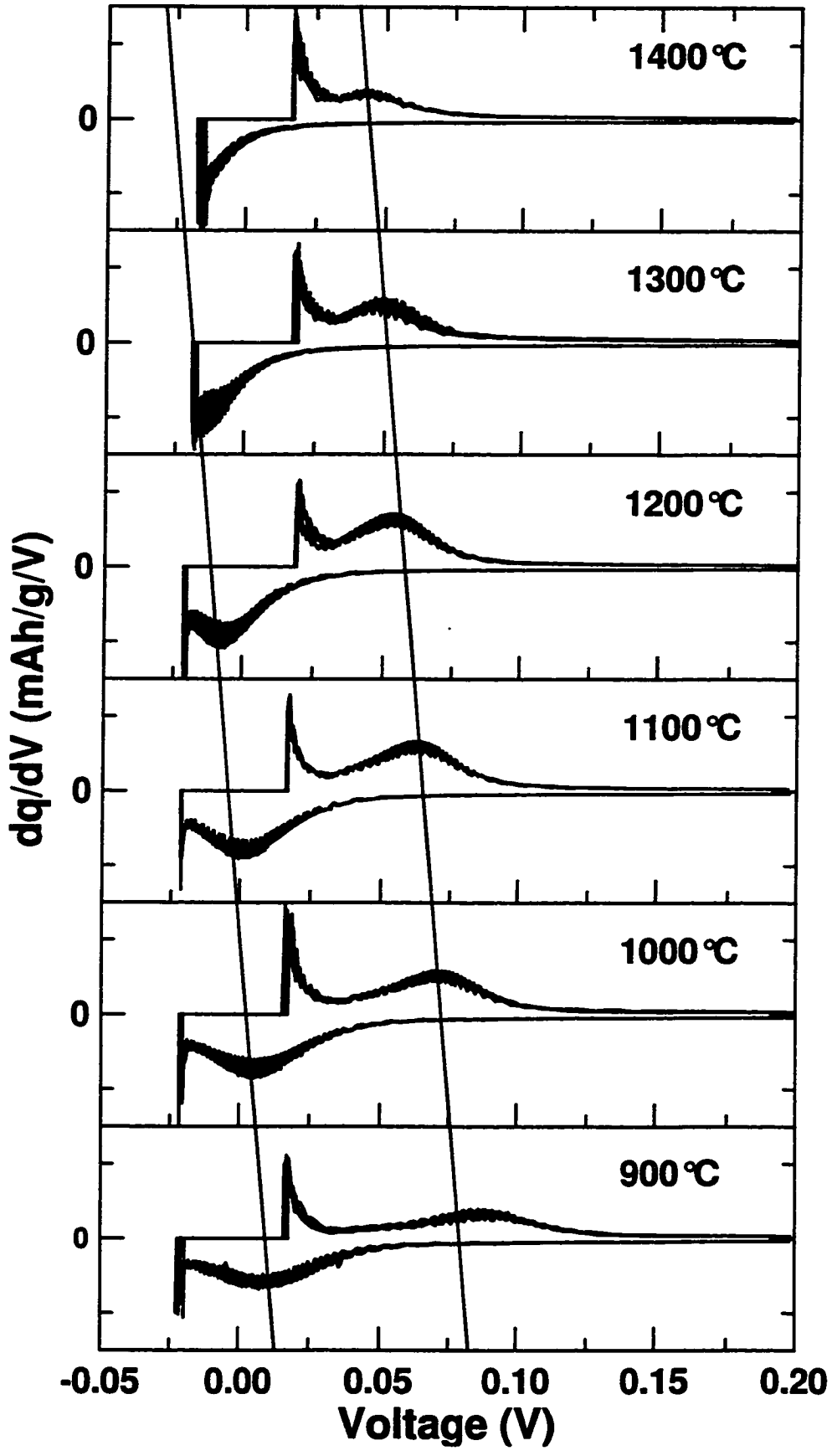

Figure 7.2: The differential capacity versus voltage for samples pyrolysed to different temperatures between 900 and 1400°C. The solid lines are guides to the eye.

HTT (°C) $\pm 10°C$	BET SA (m^2/g) ±5%	R (WAXS) ±0.05	Rg (SAXS) (Å) ±0.1Å	IRREV. Capacity (mAh/g) $\pm 10 mAh/g$	REV. Capacity (mAh/g) $\pm 10 mAh/g$	Capacity Ratio $\frac{rev.}{irrev.}$
900	121	1.65	6.10	164	527	3.2
1000	35.3	1.78	6.49	128	497	3.9
1100	13.1	1.82	6.96	105	494	4.7
1200	9.0	1.91	7.42	38	462	12.2
1300	9.9	1.95	8.03	30	408	13.6
1400	9.0	2.11	8.01	26	299	11.5

Table 7.1: Electrochemical and physical properties of the pyrolysed sucrose samples.

either charge or discharge, this corresponds to the lithium metal chemical potential measured under constant current conditions. These are shifted between charge and discharge because of the non-zero internal impedance of the cell. The peak in both curves corresponds to the low voltage plateau (seen in the voltage-capacity curves of figure 7.1) or the insertion or removal of lithium in the hard carbon at a potential near that of lithium metal. The area of this peak is a measure of capacity. The potential of the peak itself is a measure of the binding energy for lithium insertion in the hard carbon.

The observed shift in binding energy is not a result of changing cell impedance. This would shift the lithium insertion peaks in opposite directions between charge and discharge when the current is reversed. In figure 7.2, parallel lines are drawn through the discharge and charge peaks showing that the shift is in the same direction for both. These peak positions have also been plotted versus HTT in figure 7.3 and, by observation, are approximately linear and parallel. Hence the shift in binding energy for lithium insertion is inherent to changes in the binding energy of lithium in the sample and not a result of changing diffusion kinetics of lithium into the hard carbon structure. So far we have spoken of the binding energy as a single binding energy even though the differential capacity curves (figure 7.2) suggest that a distribution of

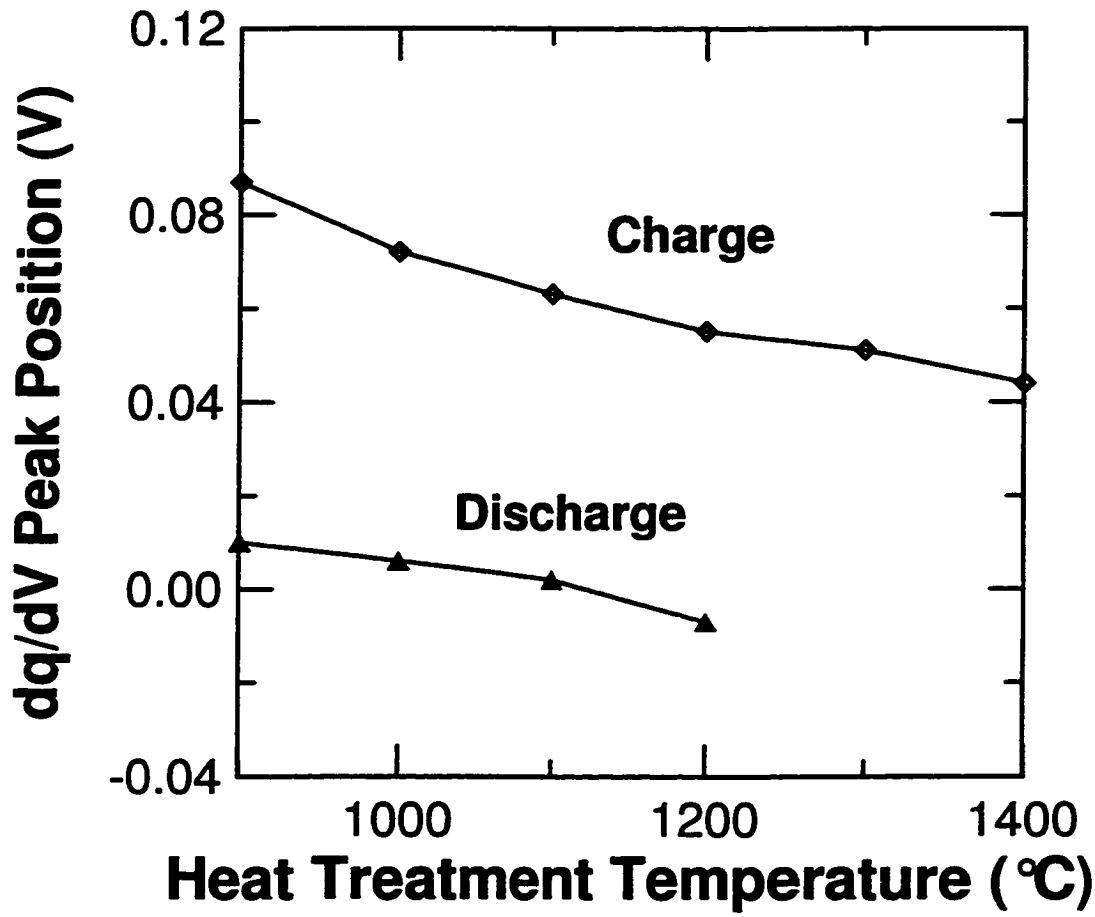

Figure 7.3: Voltage of the peak in differential capacity versus HTT for both charge and discharge.

binding energies exists.

7.2.1 Voltage Profile Modeling Based on Lithium Adsorption

A qualitative adsorption model can be used to describe the insertion of lithium in hard carbon along the low voltage plateau. This model contains only a single binding energy and an entropy component that acts to broaden the peak in the derivative curve with increasing temperature. Since the hard carbon is a disordered material with a very well developed micropore structure, the surface for adsorption is essentially the surface of each graphene sheet and hence substantial capacity can be expected from this mechanism.

The micropore structure creates a complicated surface for adsorption and therefore the simple model presented here is not expected to fit the data perfectly. It will however, give a qualitative understanding of how a single binding energy can lead to the broad peaks observed in the derivative curves and how a change in the binding energy of lithium adsorbed in the micropores of hard carbon can dramatically effect the low voltage capacity.

The adsorption model of lithium in the micropores of hard carbon is essentially identical to the statistical mechanics derivation of the Langmuir equation presented in chapter 4. Interactions between adsorbed Li atoms have been neglected since the inclusion of such a term is counter-intuitive. That is, a lithium-lithium attractive interaction is required to improve the results of the model with respect to the observed voltage profiles. Since only a repulsive coulomb interaction is expected for an adsorption process (i.e. no intercalation is occurring between graphene sheets in the low voltage plateau region), a good argument for an attractive interaction can not be given at this time and it has been excluded from this discussion.

A model of the chemical potential for lithium adsorption on the hard carbon surface (including the internal surface of micropores) is given by the Langmuir model

in analogy to equation 5.13

$$\mu = \frac{\partial A}{\partial x} = -\epsilon_{Li} - k_B T \ln \frac{x}{(1-x)}. \tag{7.1}$$

All the parameters are the same as before except that the binding energy ϵ_0 has been replaced by ϵ_{Li} to represent the binding energy of Li on the sample and n has been replaced by x; the fraction of sites occupied, to be consistent with the usual conventions.

The voltage of the cell is given by $V = -(\mu_{cathode} - \mu_{anode})/\epsilon$, where $\mu_{cathode}$ is the chemical potential of Li on the hard carbon and μ_{anode} represents the chemical potential of Li metal which is taken to be the reference, i.e. $\mu_{anode} = 0$. Using equation 7.1, the voltage profile can be calculated for different values of ϵ_{Li} at 30°C.

In figure 7.4 two calculated voltage profiles are shown. The entropy term is responsible for the shape of the curve and the peak is shifted in voltage by the binding energy of Li on the surface. One can see that if the binding energy of Li on hard carbon was equal to that of Li-metal, then only half the occupied sites in the carbon could be filled before it becomes energetically favourable to plate Li-metal. As the binding energy increases, the cell potential increases and more sites are available for adsorption before plating occurs.

The differential capacity curves can be calculated by solving equation 7.1 for x and then differentiating with respect to V

$$\frac{dx}{dV} = -\frac{e^{\frac{\epsilon_{Li}-eV}{k_B T}}}{k_B T (e^{\frac{\epsilon_{Li}-eV}{k_B T}} + 1)^2}. \tag{7.2}$$

The differential capacity given by equation 7.2 is plotted for three different binding energies as shown in 7.5. As can be see on the graph, the peaks in the differential capacity coincide with their binding energies. These peaks are broadened, due to the entropy term included in the free energy, and the capacity below 0 V is not realised because it is more energetically favourable to plate lithium metal on the surface of the electrode than fill an adsorption site with lower binding energy.

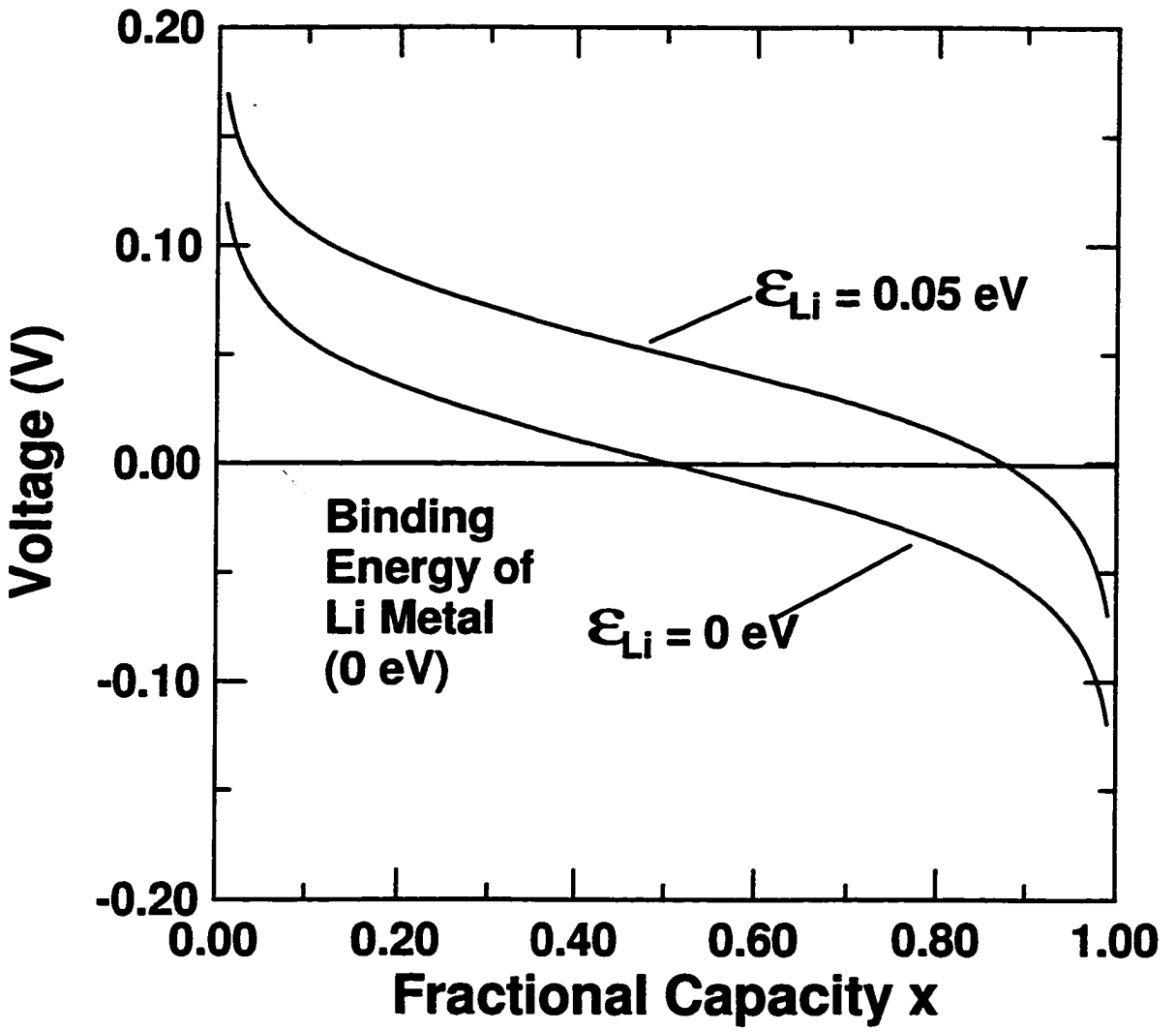

Figure 7.4: Calculated voltage curves for the adsorption of Li on a surface with a single binding energy.

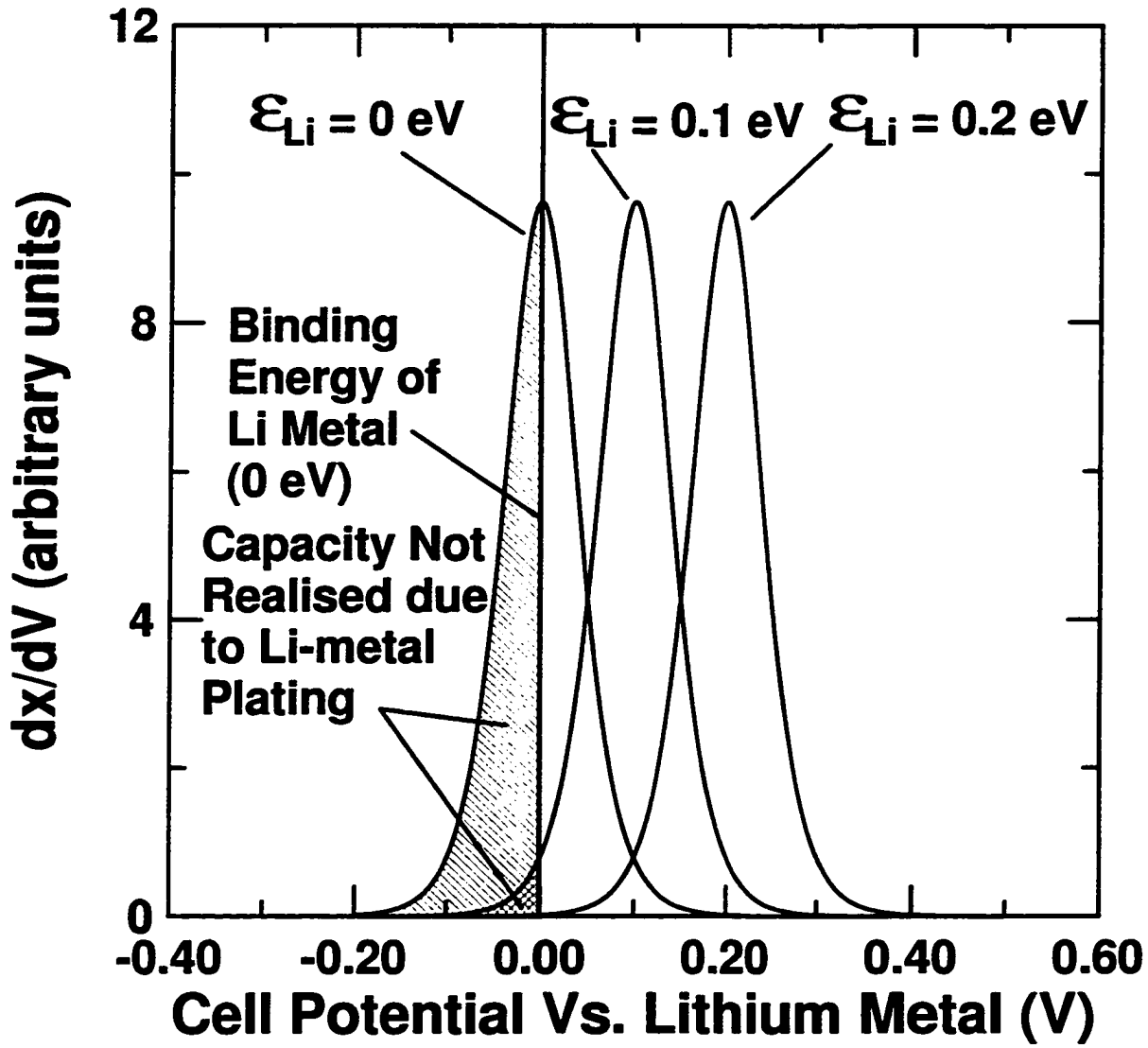

Figure 7.5: Calculations of the differential capacity versus voltage for the adsorption of Li on a surface with a single binding energy. The sign of the differential capacity has been changed for convenience.

These calculations have shown that it is possible to describe the lithium insertion at low voltage in hard carbon using a simple adsorption model that contains only a single binding energy. This description is poor since the shape of the calculated voltage profile and width of dx/dv are not well matched to the measured data suggesting a Li-Li interaction term in the model is necessary. However, changes in this binding energy, as shown in figure 1.2, may be responsible for a shift in capacity below 0 V thus causing lithium plating to occur earlier; i.e. before the entire capacity of the low voltage plateau can be filled. It is not yet fully understood how this shift in the chemical potential is correlated to micropore closure or if it is correlated at all. At present, it is believed that both will contribute independently to the reversible capacity reduction.

7.3 WAXS and SAXS Measurements

The WAXS measurements show that the internal structure is essentially independent of HTT. For brevity, figure 7.6 shows only the two extreme cases for samples pyrolysed to 900 and 1400°C. The sharp peaks are due to corundum and are artifacts of the alumina boat used to contain the sample.

The SAXS curves shown in figure 7.7 shows a continuous trend to larger micropores as the HTT is increased. In figure 7.8, the empirical parameter R and the effective micropore radius R_g are plotted against HTT. Both tend to increase with HTT and this can be explained with the simplistic "falling cards" model [59] depicted in figure 7.9.

Two micropores separated by a single graphene sheet coalesce when a single layer becomes mobile at high temperature and aligns with neighbouring layers. This process is similar to graphitization but on a very small scale. The importance of these results is that the graphene sheets in hard carbon are, to some degree, mobile at temperatures above about 1000°C. Another important result from SAXS is that the micropore structure is always present in the sample. There is no evidence for the loss of this

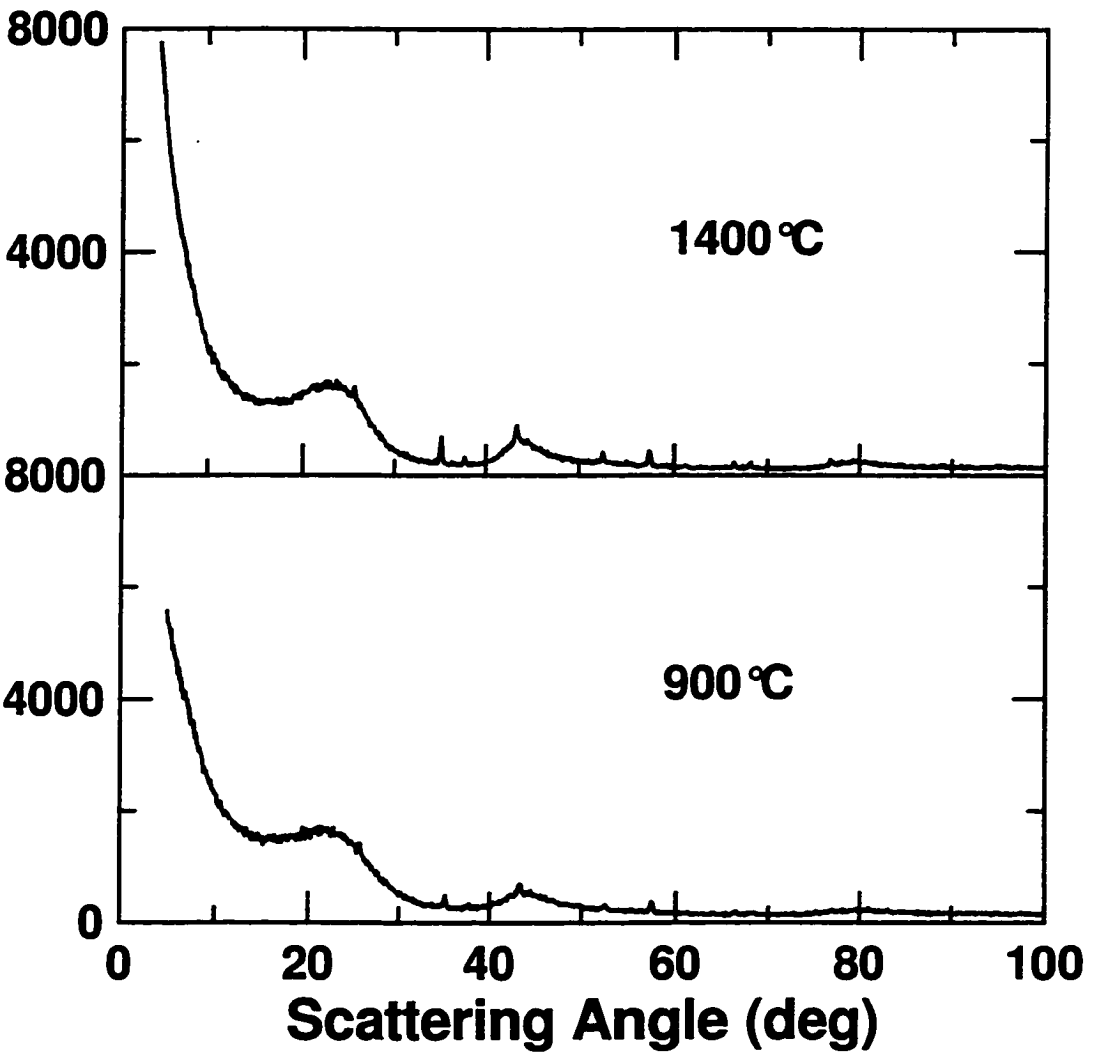

Figure 7.6: WAXS scattering profiles for samples pyrolysed to 900 and 1400°C.

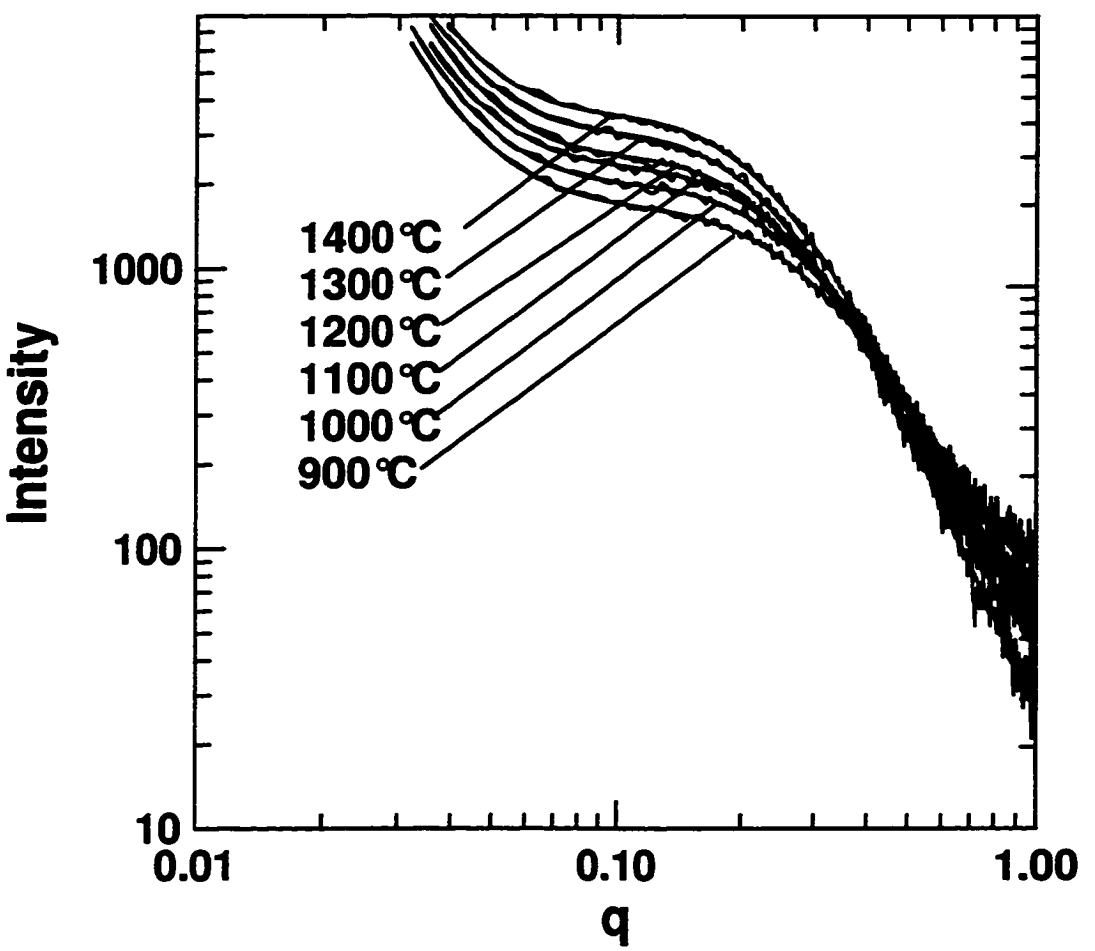

Figure 7.7: SAXS curves for samples pyrolysed between 900 and 1400°C. Smooth solid lines represent the best fit calculated intensities.

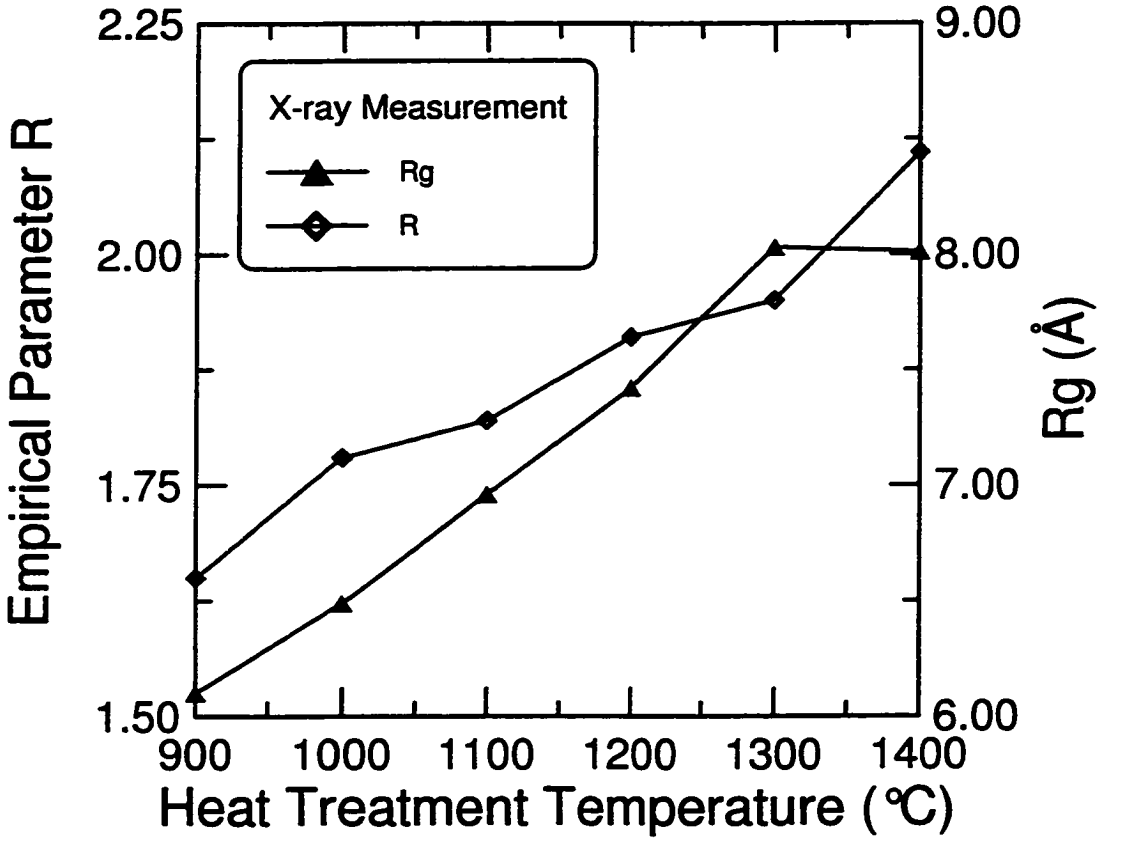

Figure 7.8: The empirical parameter R and the effective pore size R_g determined from WAXS and SAXS data respectively, vs. HTT.

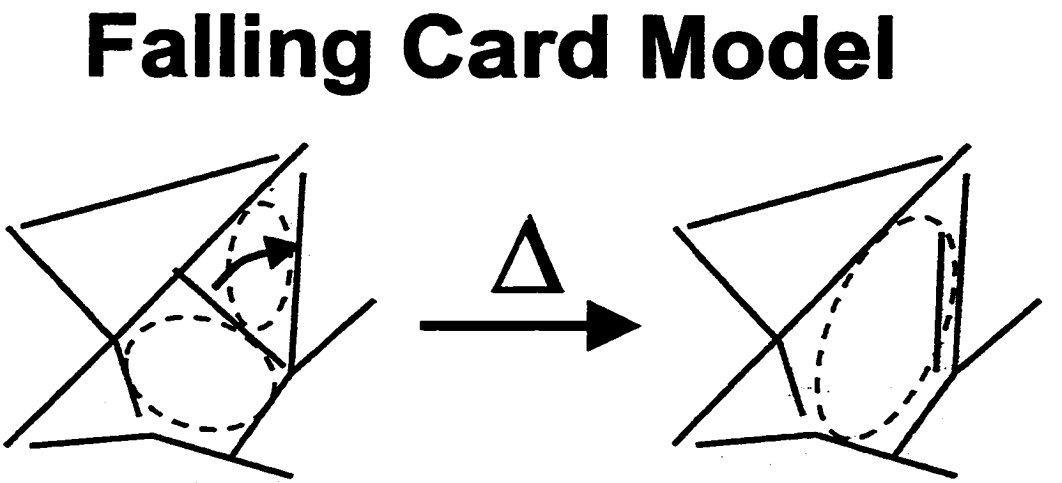

Figure 7.9: The falling card model for hard carbon; solid lines represent graphene sheets.

structure; only an increase in the average micropore size. Therefore the capacity loss can not be attributed to a loss of the micropore structure.

7.4 BET Surface Area

The limited graphitization at high HTT has a dramatic effect on the surface properties of the sample as measured by gas adsorption. As shown in figure 7.10, as the HTT increases, the BET surface area decreases by almost an order of magnitude. Such large changes in surface area are difficult to explain by even the most dramatic changes in surface geometry. Introducing the idea of micropore closure is one way of explaining this phenomena and CO_2 gas adsorption techniques are instrumental in providing evidence for such a process.

7.5 CO_2 Gas Adsorption Studies

CO_2 gas adsorption provides three distinct sources of evidence for micropore closure:

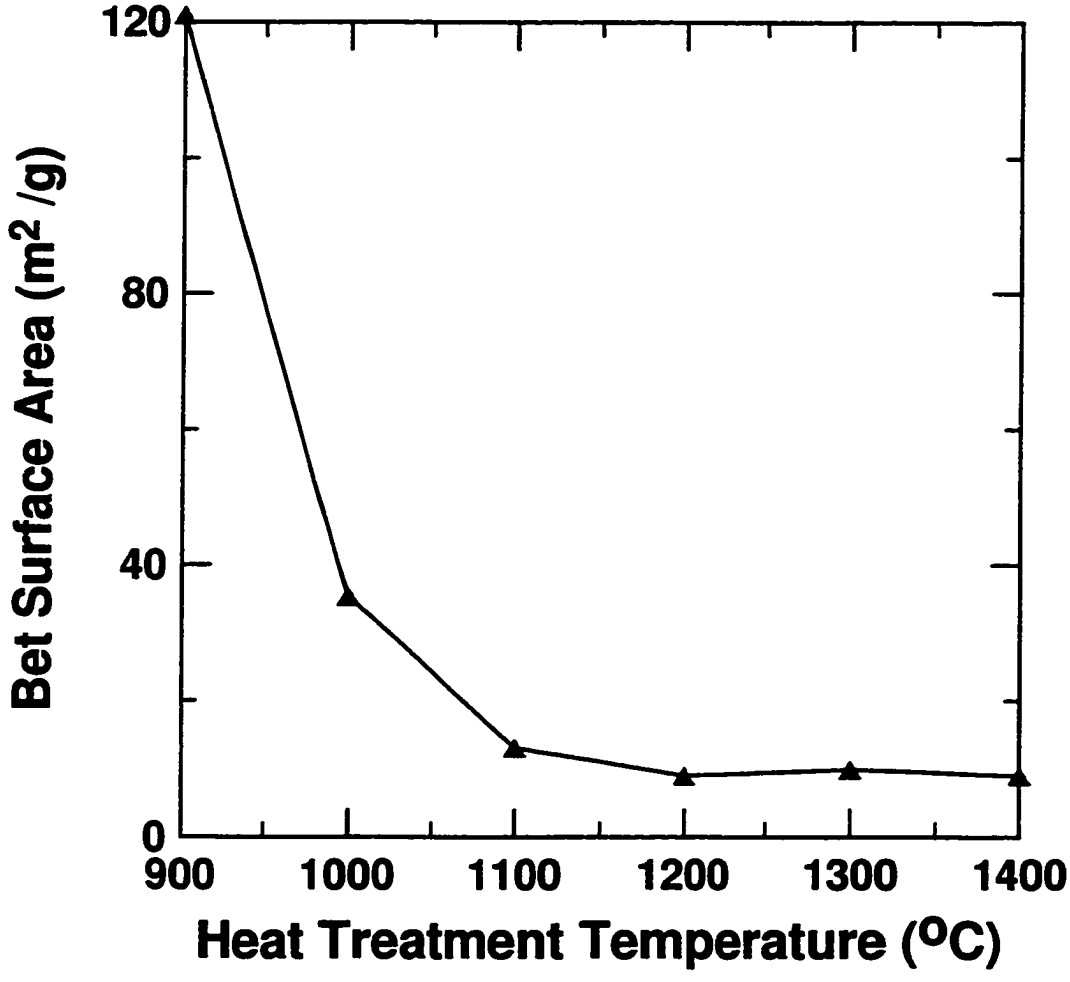

Figure 7.10: BET surface area vs. HTT for the studied samples.

1. The dramatic decrease in adsorption with increasing HTT (figure 7.11).

2. The hysteresis that appears and then disappears with increased HTT is evidence for presence of partially closed micropores.

3. Kinetics of adsorption data (figure 7.12) shows that the rate of adsorption decreases dramatically for the range of HTTs where partially closed micropores are present in the samples.

The surprisingly large adsorption of 60cc per gram of hard carbon corresponds to roughly 1 CO_2 molecule for 5 aromatic rings (C_6). This substantial amount of adsorption is taken as a good indication that there is a significant amount of penetration of CO_2 inside the hard carbon sample and that the micropore structure is well developed and accessible throughout the material.

A simple model explaining the process of micropore closure is shown in figure 7.14. At 900°C we believe that the micropores in the sample are predominantly of type 1. These micropores are easily accessible by CO_2 and as a result there is no hysteresis between adsorption and desorption and the kinetics of adsorption are relatively fast. At temperatures higher than 900°C, we believe that a combination of all three micropores exist in hard carbon.

Type 2 micropores have an "ink bottle" shape because they are partially closed and this type of micropore results in hysteresis between adsorption and desorption [64]. The hysteresis adsorption model is based on the work done many years ago by Kelvin [78] who discussed in thermodynamic terms the vapour pressure p of a liquid contained in a cylindrical capillary or radius r. From his treatment it is possible to arrive at what is called the Kelvin equation:

$$\ln \frac{p}{p_0} = -\frac{2V\gamma}{rk_BT} \cos\phi \tag{7.3}$$

where p_0 is the saturation vapour pressure, γ the surface tension, V the molar volume of the liquid and ϕ is the angle of contact between the liquid and the walls of the capillary. In order to make progress with the Kelvin equation it is necessary to assign

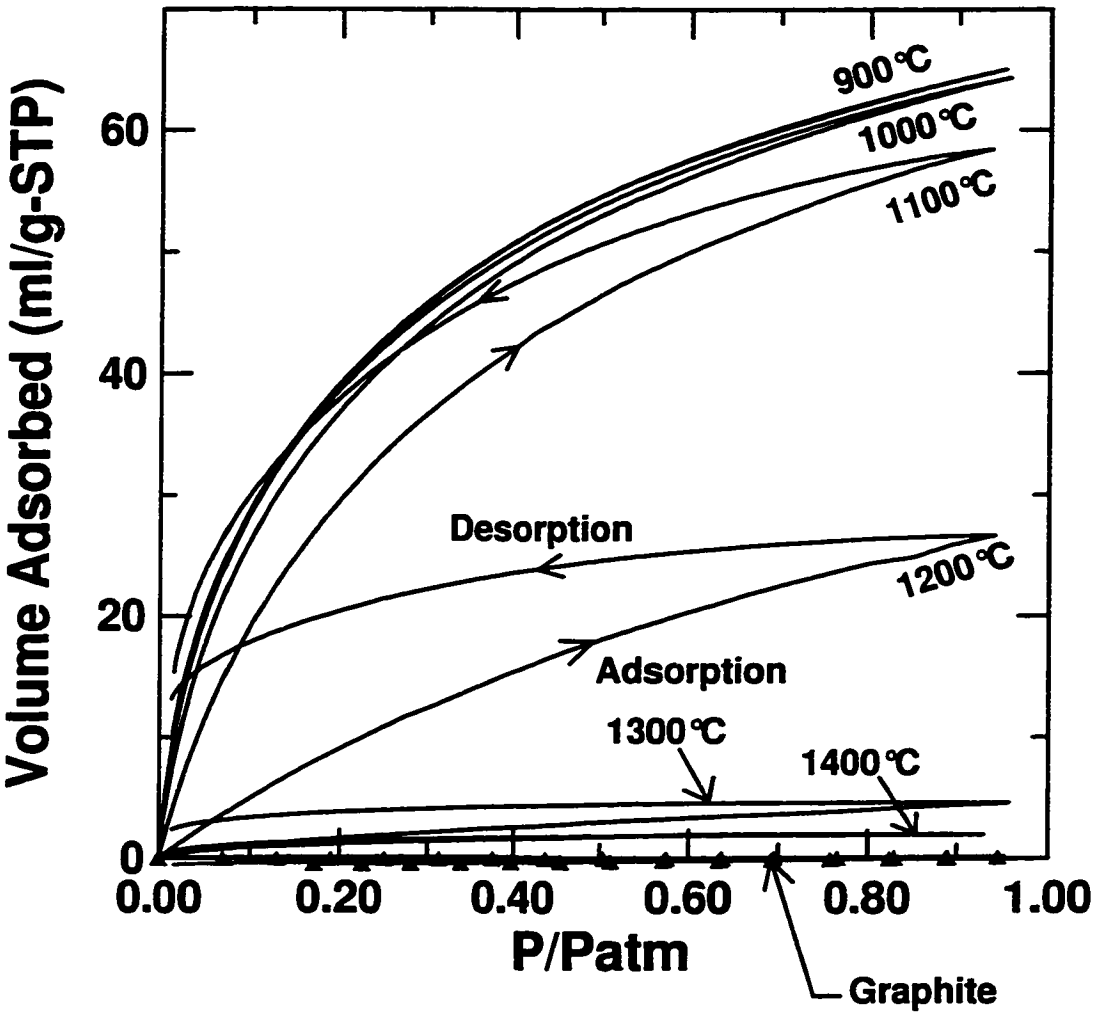

Figure 7.11: CO_2 gas adsorption isotherms for samples pyrolysed between 900 and 1400°C. HTTs are indicated.

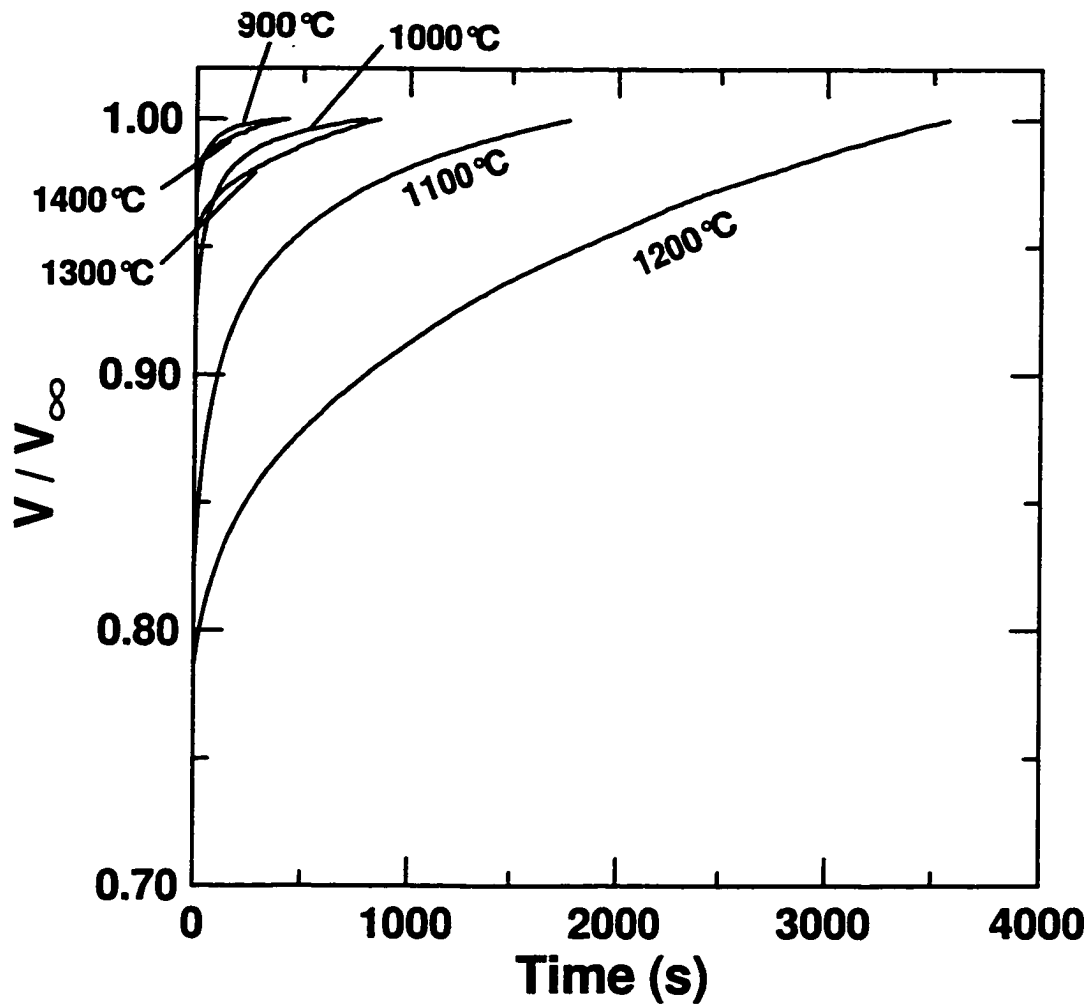

Figure 7.12: Kinetics of adsorption data for samples pyrolysed between 900 and 1400°C. HTTs are indicated.

a value to the contact angle ϕ, a quantity which is unfortunately extremely difficult to determine directly in the case of porous solids. Although not justified, the usual method is to make the simplifying assumption that $\phi = 0$ i.e. the liquid wets the walls of the pores. The Kelvin equation then simplifies to the form

$$\ln \frac{p}{p_0} = -\frac{2V\gamma}{rk_BT}. \tag{7.4}$$

In the "ink bottle" hypothesis, hinted at by Kraemer[79] and developed by McBain[80] and others [81, 82], the pore is visualized as having a narrow neck of radius r_1 and a wide body of radius r_2 as shown in figure 7.13. Along the adsorption branch, condensation in the body of the pore will occur when the pressure reaches the value of $\ln \frac{p_2}{p_0} = -\frac{2V\gamma}{r_2k_BT}$ given by inserting $r = r_2$ into equation 7.4. During desorption, evaporation cannot occur at pressure p_2 since the neck of the pore is blocked by a meniscus which can only evaporate when the pressure has fallen to $\ln \frac{p_1}{p_0} = -\frac{2V\gamma}{r_1k_BT}$; the whole pore then empties at once. The pressure is thus greater during adsorption than during desorption thus giving rise to the observed hysteresis.

The type 2 micropore also forces CO_2 molecules to diffuse through narrow pore openings. These openings become narrower (until they finally close off) as the HTT is increased and the rate of adsorption decreases dramatically as gas molecules are forced to diffuse through smaller and smaller openings. Examining the kinetics of adsorption data (figure 7.12), we notice that the sample pyrolysed to 1200°C exhibits the slowest rate of adsorption. In figure 7.14, we also notice that this sample shows the largest amount of hysteresis between adsorption and desorption. Since both of these phenomena are attributed to type 2 micropores, it is likely that this sample contains the largest number of these micropores.

The third type of micropore is a closed micropore not capable of adsorbing CO_2 in its interior. The presence of this type of micropore acts only to reduce the total amount of adsorption. We believe that samples pyrolysed to temperatures of 1400°C and above show primarily this type of micropore. In figure 7.12 the kinetics of adsorption between this sample and the sample heat treated to 900°C are very similar. From the model we would not expect to see a significant difference in the kinetics of

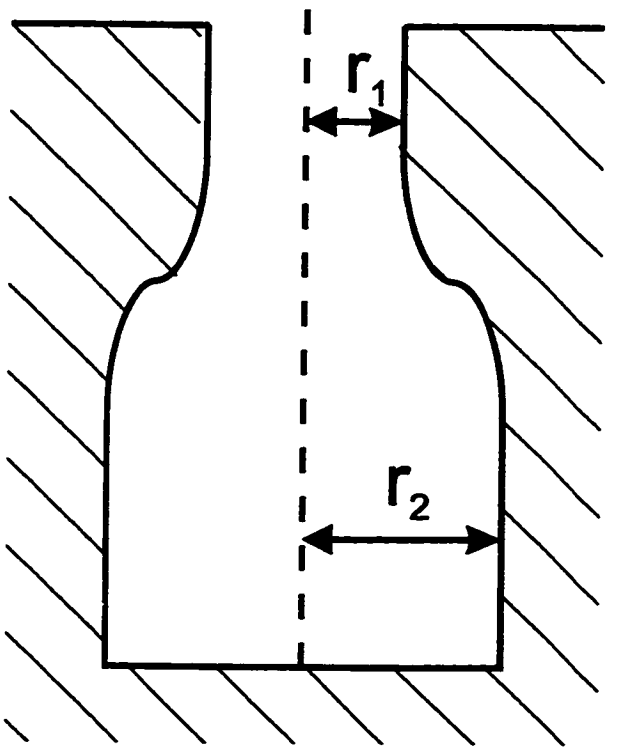

Figure 7.13: An artistic depiction of an "ink-bottle" shaped micropore having only one opening.

adsorption for samples comprised of primarily type 1 or type 3 micropores because both have relatively open surfaces for adsorption when compared to a type 2 micropore. The total amount of adsorption is, of course, dramatically different between these two samples because in one case the micropores are open and in the other the micropores are closed.

This simple model of micropore closure explains the gas adsorption results quite well on a qualitative bases. As the samples are heated to higher HTTs, the micropores close and form what we call "embedded fullerenes." Since lithium cannot penetrate the fullerene, the sites accessible for lithium insertion are reduced. The gas adsorption results show that micropore closure is occurring at the same HTT where we begin to see capacity loss and hence we believe that this is at least partially responsible for the observed reduction in capacity.

7.5.1 Model of Micropore Closure

In this section, a model for micropore closure is described that allows the number of open micropores to be calculated as a function of the heat treatment temperature and exposure time. The measured gas adsorption isotherms show that the micropores in the sample are closing as the HTT is increased. The simplest model would feature the open micropores as a metastable state that must overcome an activation energy to form a closed micropore with a lower energy state. This activation energy can be thought of as the energy needed to break carbon-carbon bonds so that the carbon atoms can rearrange in the material to form embedded fullerenes. This model is depicted graphically in figure 7.15.

In the simplest model, the rate of micropore closure is equal to the number of open micropores (N) times the rate constant κ

$$\frac{dN}{dt} = -\kappa N. \tag{7.5}$$

The solution to equation 7.5 is straight forward

$$N(t) = N_0 e^{-\kappa t}, \tag{7.6}$$

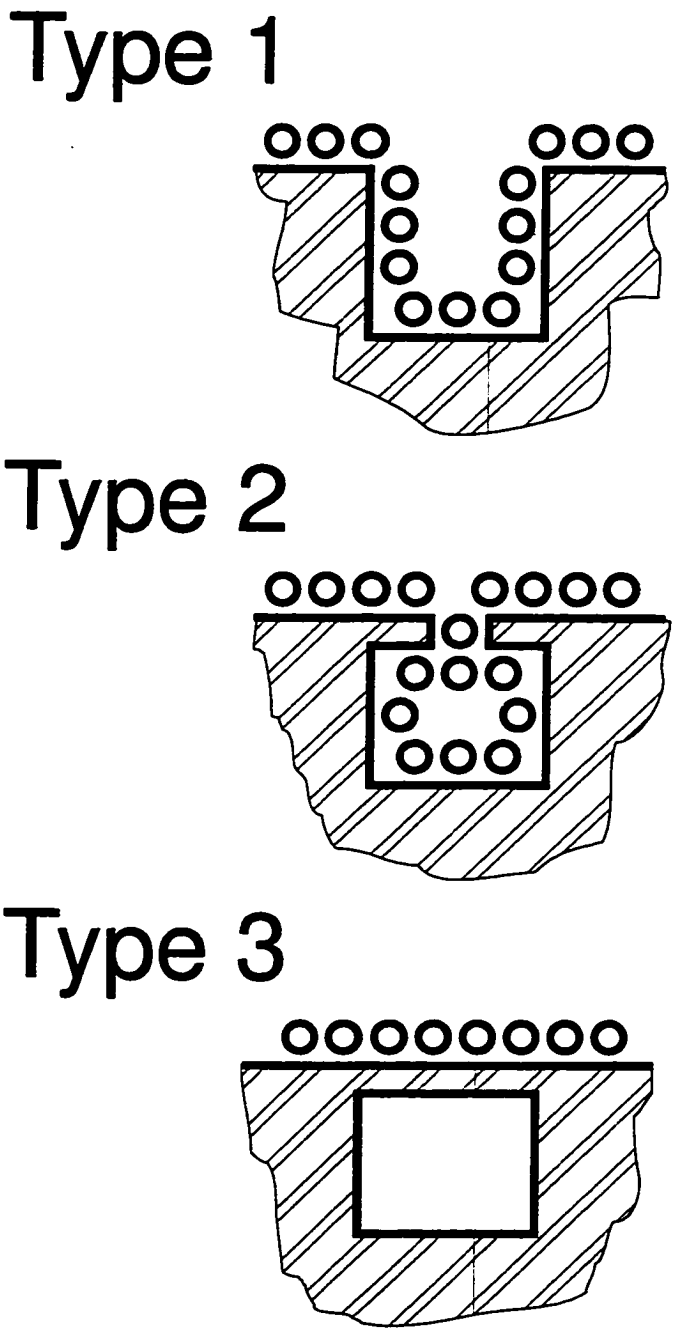

Figure 7.14: Model of micropore closure depicting open micropores (Type 1), partially closed micropores (Type 2) and fully closed micropores (Type 3).

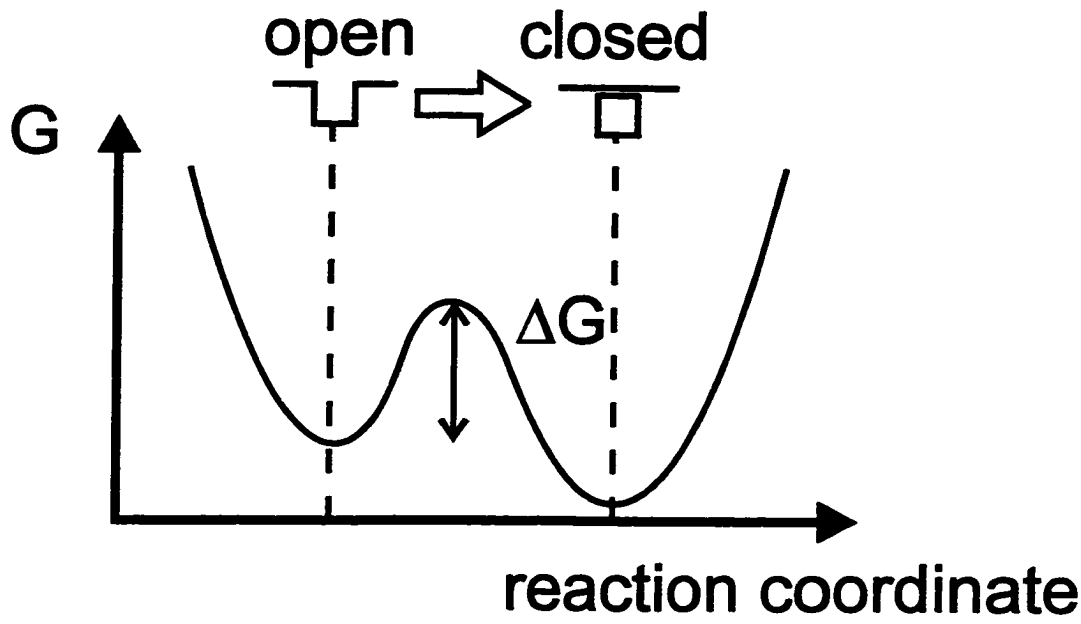

Figure 7.15: Gibb's free energy diagram of the simplistic model of micropore closure.

where N_0 is the number of open pores at low heat treatment temperatures (say 900°C). There is an important relationship between the rate of reaction and the magnitude of the activation energy ΔG. Assuming Arrenhius behaviour, the relationship between the rate constant (κ) and ΔG is an exponential of the form:

$$\kappa = \kappa_0 e^{-\Delta G/k_B T}. \tag{7.7}$$

Here k_B is Boltzmann's constant and κ_0 is an attempt frequency having units of $1/time$. For all intents and purposes it is easier to think of ΔG as a temperature i.e. $\Delta G = k_B T_\Delta$. Substituting equation 7.7 into 7.6 we arrive at an equation that describes the number of open micropores as a function of time and heat treatment temperature.

$$N(T,t) = N_0 e^{-\kappa_0 t e^{-T_\Delta/T}} \tag{7.8}$$

The number of micropores that remain open is determined by the volume of CO_2 that is adsorbed by the sample. Equation 7.8 is modified to reflect the measured

adsorption volume $V(T,t)$

$$V(T,t) = V_0 e^{-\kappa_0 t e^{-T_\Delta/T}} + V_{SA} \tag{7.9}$$

where V_0 is the parameter that characterizes the number of open micropores (however the specific choice of V_0 has not yet been discussed) and V_{SA} is a correction for surface adsorption that is essential for fitting samples with predominantly closed micropores. The choice of V_0 is somewhat arbitrary because one cannot be sure whether the adsorption or desorption branches of the adsorption curve truly represent the number of open micropores. The volume of open pores can be determined by fitting the adsorption isotherm to the Langmuir, Dubinin-Rudushkevich or Dubinin-Astakhov equations and extrapolating the pore volume. Since both the adsorption and desorption branches will give differing results depending on the amount of hysteresis, each fit is performed for both sections of the isotherm and averaged to give the best estimate of the pore volume.

Langmuir Model

The Langmuir equation is rearranged in a linearized form so that the parameter V_0 (volume adsorbed at $p/p_0 = 1$) can be extracted.

$$\frac{(p/p_o)}{V} = \frac{1}{V_0}(p/p_o) + \frac{1}{V_0 C}. \tag{7.10}$$

This equation now has the form $y = mx + b$ if $y = \frac{(p/p_o)}{V}$, $x = (p/p_o)$, $m = \frac{1}{V_0}$ and $b = \frac{1}{V_0 C}$. In figure 7.16 the adsorption isotherms are plotted in the linearized form and V_0 is extracted from the slope of these lines. The results of this process are shown in table 7.2.

V_0 is plotted vs. HTT and exposure time on figure 7.17 and fitted to equation 7.9 which is shown as the solid line on the graph. The fitting procedure is done using the solver feature of Microsoft Excel 5.0 and all parameters were varied to obtain the best fit. As one can see, the fit to the data is surprisingly good given the simplicity of

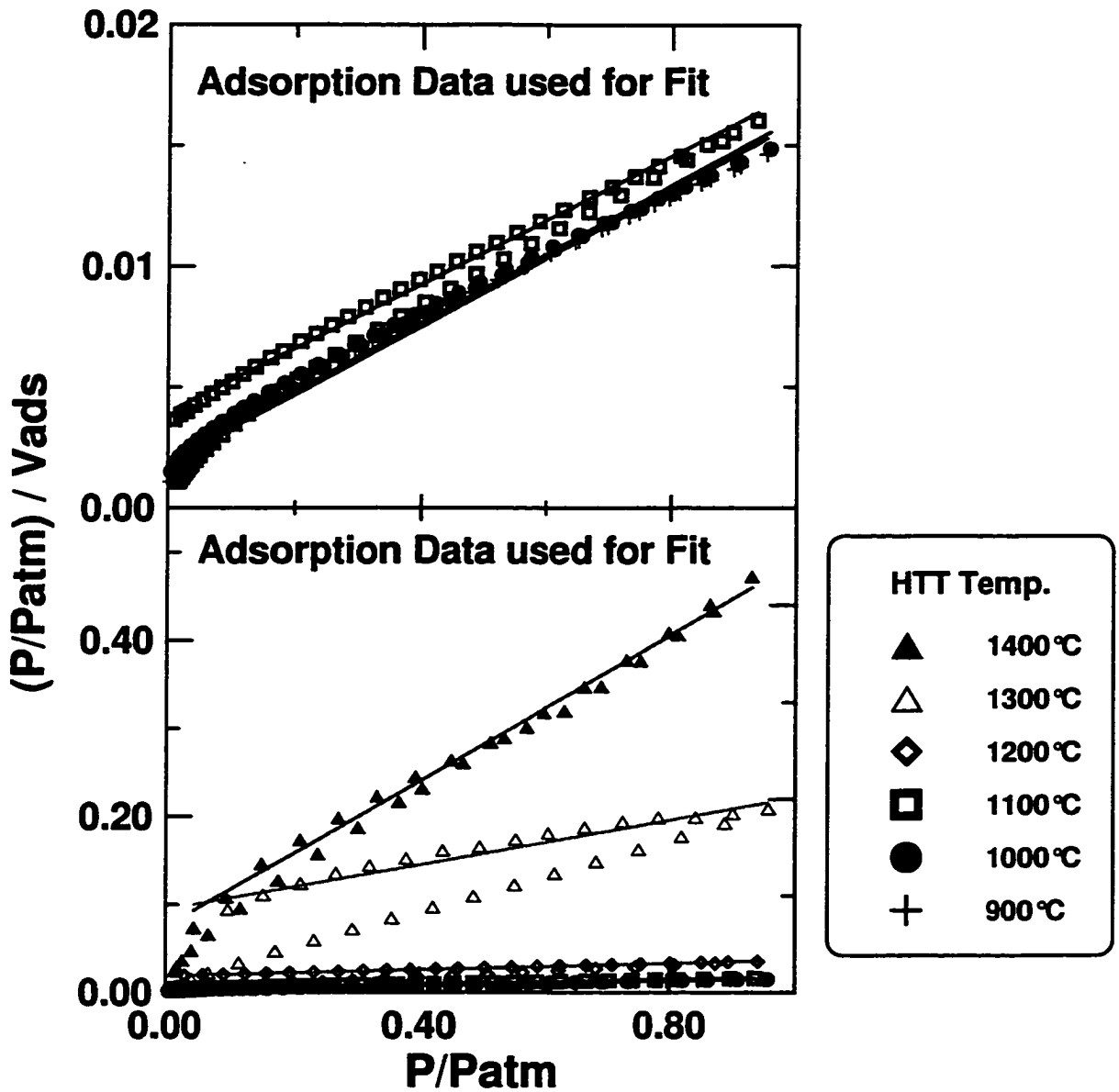

Figure 7.16: Adsorption isotherm plotted in the linearized Langmuir form.

HTT (°C)	Adsorption Pore Vol. (cm^3)	Desorption Pore Vol. (cm^3)	Average Pore Vol. (cm^3)
900	71.94	69.9	70.9
1000	73.53	69.0	71.3
1100	75.76	60.2	68.0
1200	54.95	27.0	41.0
1300	7.30	4.76	6.03
1400	1.80	1.41	1.61

Exposure Time (hr.)	Adsorption Pore Vol. (cm^3)	Desorption Pore Vol. (cm^3)	Average Pore Vol. (cm^3)
0	72.8	69.0	70.9
1	75.8	60.2	68.0
2	70.1	62.0	66.1
4	70.2	51.9	63.9
8	70.9	49.0	60.0
16	66.7	37.6	52.1

Table 7.2: Results of the extrapolated pore volume, V_0, from the Langmuir equation for samples pyrolysed to different HTTs for 1 hour (top) and to different exposure times at 1100°C (bottom).

V_0	V_{SA}	κ_0	T_Δ	ΔG
69.2 cm^3	2.79 cm^3	$1.71 \times 10^8 s^{-1}$	4.27×10^4K	3.68 eV

Table 7.3: Results of fitting the extrapolated micropore volume from the Langmuir model to theory.

the model. The parameters obtained from the fitting program are tabulated in table 7.3.

Dubinin-Radushkevich Model

The pore volume was also determined using the linearized Dubinin-Radushkevich equation as explained in chapter 5. The results are tabulated in table 7.4.

The average pore volumes were then fit to equation 7.9 in exactly the same manner as was done for the Langmuir model. The results are shown in figure 7.18 and tabulated in table 7.5.

The measured pore volume calculated by the Dubinin-Radushkevich equation is unrealistically high. The fit to the exposure time data is also very poor. The use of this model does not add to the understanding of the lithium insertion properties and leads to very nearly the same result for the activation energy needed to close micropores.

Dubinin-Astahkov Model

The Dubinin-Astahkov model includes an additional parameter, the Astahkov exponent, to the fitting algorithm. This further complicates the analysis and the presence of the additional parameter makes the result for the total pore volume somewhat arbitrary. The extrapolated pore volumes are shown in table 7.6.

The resulting pore volumes are only poorly correlated to the HTT and exposure time when compared to the results of the Langmuir and Dubinin-Radushkevich models. For this reason, this method of determining the total pore volume was not

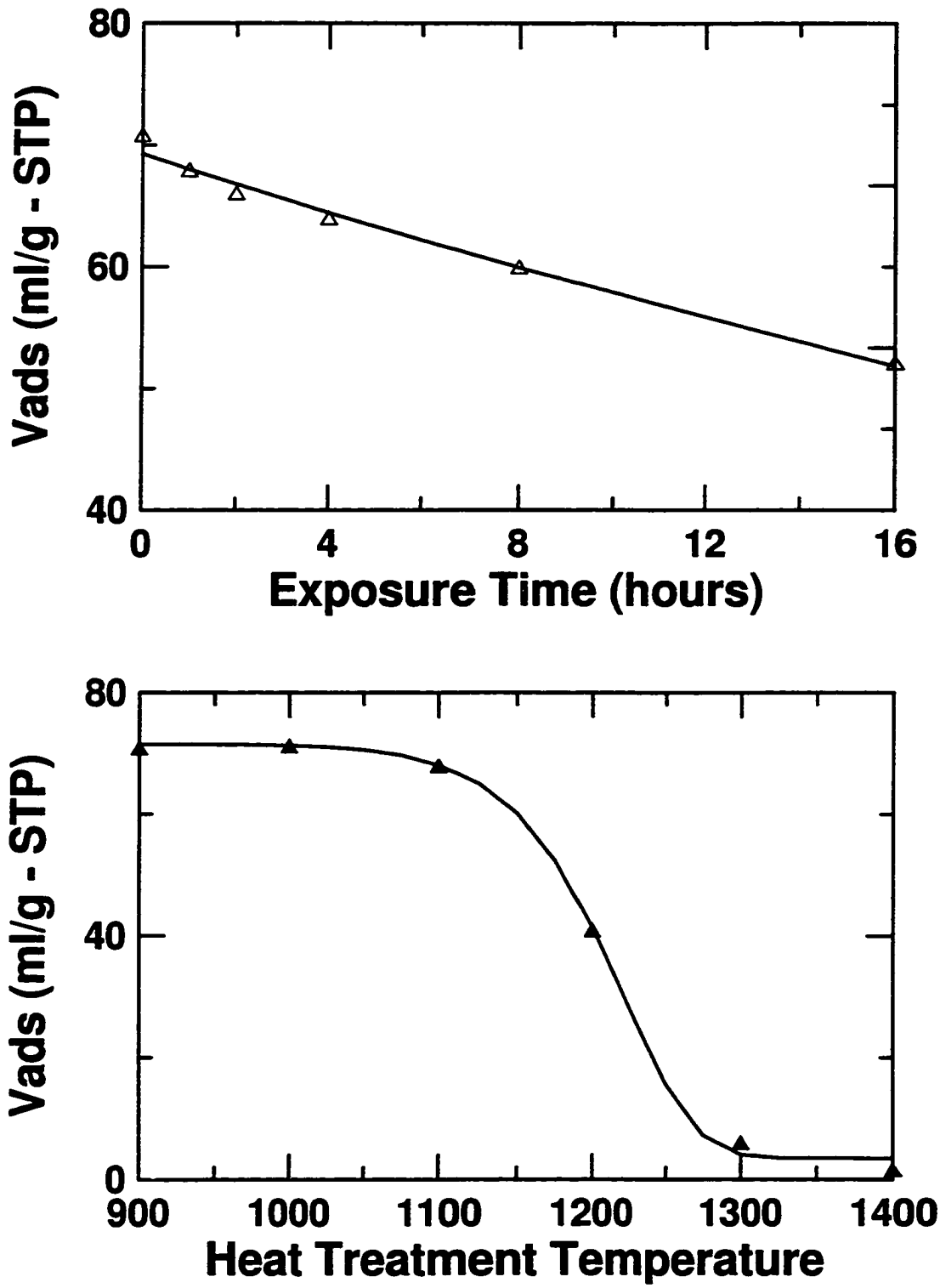

Figure 7.17: Extrapolated maximum volume adsorbed based on Langmuir model of gas adsorption vs. HTT. (bottom) and exposure time (top). The solid line represents the fit to the data points.

HTT (°C)	Adsorption Pore Vol. (cm^3)	Desorption Pore Vol. (cm^3)	Average Pore Vol. (cm^3)
900	109.3	110.29	109.8
1000	113.5	106.9	110.2
1100	118.6	87.3	102.7
1200	74.7	32.6	53.6
1300	11.5	5.71	8.60
1400	2.64	1.87	2.26

Exposure Time (hr.)	Adsorption Pore Vol. (cm^3)	Desorption Pore Vol. (cm^3)	Average Pore Vol. (cm^3)
0	113.7	107.7	110.7
1	118.6	87.3	103.0
2	110.4	84.9	97.7
4	111.2	70.9	91.1
8	110.7	66.7	88.7
16	102.0	57.2	79.6

Table 7.4: Results of the extrapolated pore volume, V_0, from the Dubinin-Radushkevich equation for samples pyrolysed to different HTTs for 1 hour (top) and to different exposure times at 1100°C (bottom).

V_0	V_{SA}	κ_0	T_Δ	ΔG
105.4 cm^3	5.20 cm^3	$1.57 \times 10^9 s^{-1}$	4.57×10^4K	3.94 eV

Table 7.5: Results of fitting the extrapolated micropore volume from the Dubinin-Radushkevich model to theory.

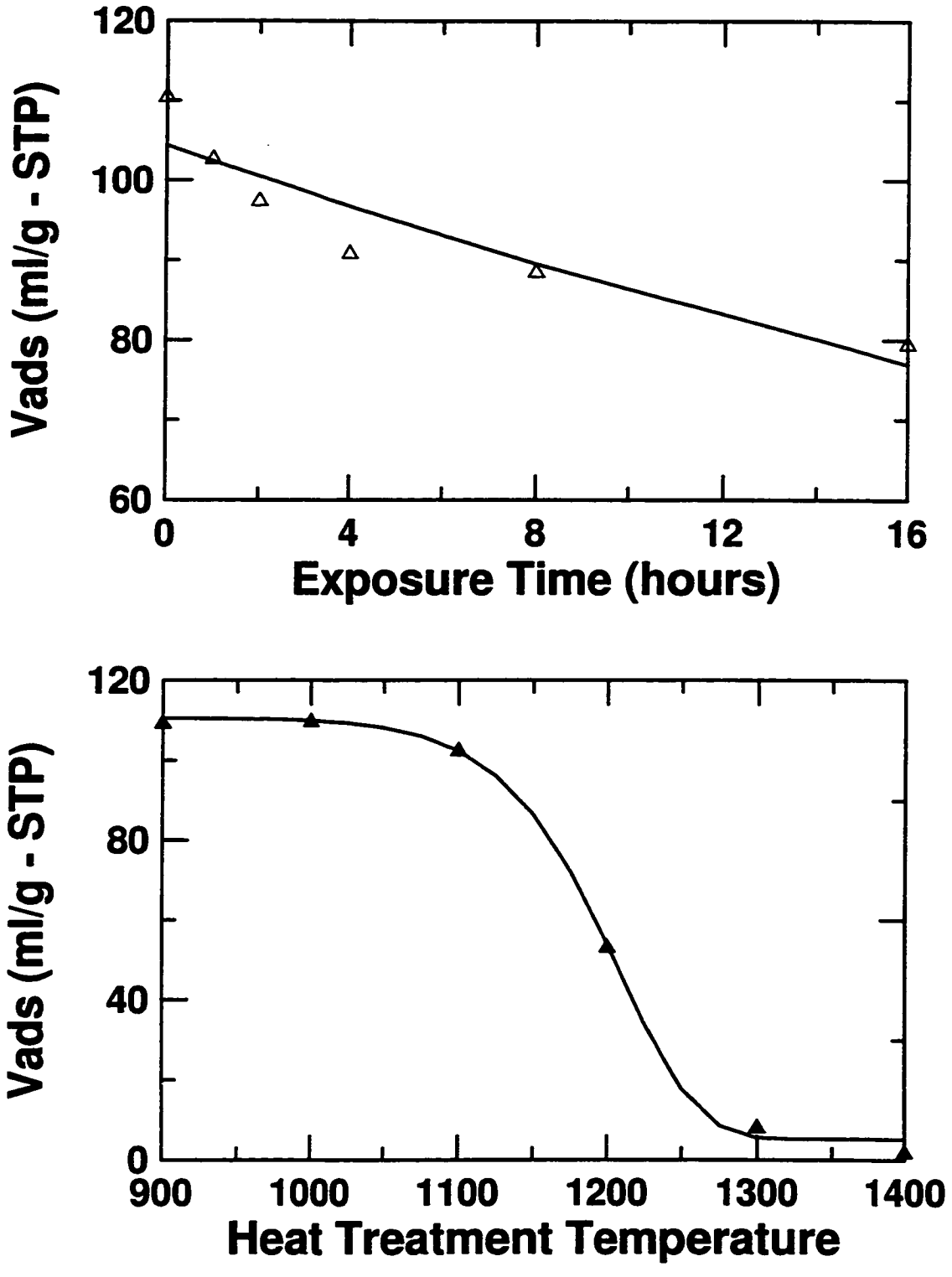

Figure 7.18: Extrapolated maximum volume adsorbed based on Dubinin-Radushkevich model of gas adsorption vs. HTT. (bottom) and exposure time (top). The solid line represents the fit to the data points.

HTT (°C)	Adsorption Pore Vol. (cm^3)	Desorption Pore Vol. (cm^3)	Average Pore Vol. (cm^3)
900	94.2	93.4	93.8
1000	97.2	94.2	95.7
1100	93.2	99.8	96.5
1200	67.1	54.3	60.7
1300	67.2	5.46	36.3
1400	2.34	1.59	1.97

Exposure Time (hr.)	Adsorption Pore Vol. (cm^3)	Desorption Pore Vol. (cm^3)	Average Pore Vol. (cm^3)
0	96.9	97.9	97.4
1	93.2	99.8	96.5
2	88.2	86.1	87.2
4	89.8	95.4	92.6
8	87.5	94.2	90.9
16	83.9	75.3	79.6

Table 7.6: Results of the extrapolated pore volume V_0 from the Dubinin-Astahkov equation for samples pyrolysed to different HTTs for 1 hour (top) and to different exposure times at 1100°C (bottom).

explored any further.

7.6 Conclusion

Reducing the hysteresis in the voltage profile by heating the sample to higher HTTs results in the loss of capacity above a critical temperature of about 1100°C. X-ray diffraction analysis has shown that a type of restructuring, similar to graphitization but on a very small scale, occurs in hard carbon at HTTs above about 1000°C. Measurements of differential capacity versus cell potential show that there is a shift in the lithium insertion potential towards the chemical potential for plating of lithium metal on the surface. At temperatures greater that 1200°C it appears that a significant proportion of the lithium insertion binding energies are lower than this threshold. At this same temperature, gas adsorption results show that the micropores in the sample begin to close and form what we call "embedded fullerenes." Based on the results of lithium intercalation in C_{60} [83, 84], this reduces the lithium insertion capacity because Li-ions cannot penetrate into the interior of the fullerene and the surface area for lithium adsorption is decreased. At present, is is unclear whether the shift in lithium insertion potential and micropore closure are related. One possible alternative explanation for the shift in chemical potential is the increased micropore size determined by SAXS measurements. Micropores with smaller radii naturally lead to increased binding energies because the bound lithium atoms are closer to more carbon atoms. In this way, the observed shift in chemical potential may result from the larger pore size and be independent of micropore closure.

A model of micropore closure has also been presented with good agreement to the data. It is very likely that the free energy of activation is the energy required to break carbon-carbon bonds so that they can realign and form the embedded fullerene structures that are responsible for the loss in capacity of the sample. Although it is difficult to estimate the carbon-carbon bond energy in the disorder hard carbon structure, the calculated value of ~3.6-4.0 eV is certainly a reasonable one considering

the carbon-carbon bond strength in graphite is approximately 4 eV (calculated from the enthalpy of formation of graphite from carbon gas).

Chapter 8

Conclusion

In the fall of 1994, when this thesis began, hard carbon was one of the most promising anode materials for Li-ion batteries. In particular, sucrose showed large reversible capacity (600 mAh/g) and good cycle life and looked very promising for the Li-ion battery industry. As a result, understanding the properties of hard carbon prepared from sucrose became the aim of this thesis.

Hard carbon typically suffers from two problems; a large irreversible capacity and hysteresis in the voltage profile between charge and discharge. Developing an understanding of each of these two problems would hopefully lead to the synthesis of superior materials which was the goal of this thesis.

In studying the irreversible capacity, two methods were found to reduce the large irreversible capacity in hard carbon that results from air exposure. These techniques are instrumental in producing commercially viable electrode materials that can be synthesized in air environments. Experimental results have shown that the irreversible capacity is not correlated to the results of any of the conventional characterization techniques such as BET surface area, wide-angle X-ray scattering (WAXS), small-angle X-ray scattering or CO_2 gas adsorption measurements. In lieu of these results, TGA analysis has shown a corelation between the samples mass loss, when heated up to 500°C, and irreversible capacity. This strongly suggests that the irreversible capacity in hard carbon is the result of the adsorption of air in the micropores of the

sample that reacts irreversibly with Li atoms during the first discharge to cause the large irreversible capacity.

The hysteresis in the voltage profile leads to the need to heat treat hard carbons to higher temperatures to reduce hydrogen content. This leads to a loss in reversible capacity above a certain critical temperature. In particular, a loss in capacity confined to the low voltage region of the voltage profile is observed. In this thesis this loss in capacity is correlated to the micropore structure of hard carbon. More specifically, to the formation of closed micropores that we have named "embedded fullerenes." In order to make this corelation, a CO_2 gas adsorption analyser was specifically designed and built to measure the adsorption isotherm of hard carbon.

This thesis has lead to a better understanding of the large capacity in hard carbon and has correlated this capacity to the micropore structure. Methods of reducing the irreversible capacity have been developed and the source of this irreversible capacity has been determined.

Bibliography

[1] J.R. Dahn, Tao Zheng, J.S. Xue, and Yinghu Liu. *Science*, 270:590–593, 1995.

[2] R.E. Franklin. In *Proc. Roy. Soc. A*, volume 209, page 196, 1951.

[3] M.J. Buerger et. al. *International Table for X-Ray Crystallography*, volume 3. The Keynoch Press, 1969.

[4] Weibing Xing and J.R. Dahn. *J. Electrochem. Soc.*, 144(4):1195–1201, 1997.

[5] D.P. Wilkinson, J.R. Dahn, U. Von Sacken, and D.T. Fouchard. In *The Electrochemical Society Extended Abstracts*, volume 90-2, pages 85,87, Seattle, WA, October 14-19 1990.

[6] W. Ebner, D. Fouchard, and L. Xie. *Solid State Ionics*, 69:238–256, 1994.

[7] A.C. Makrides, K.M. Abraham, G.L. Holleck, T.H. Nguyen, and R.J. Hurd. In *Proc. 34th Power Sources Symp.*, page 167, NJ, 1990. Cherry Hill.

[8] W.B. Ebner, J.A. Simmons, and D.L. Chua. In *Proc. 33rd Power Sources Symp.*, page 11, NJ, 1988. Cherry Hill.

[9] Tao Zheng, Yinghu Liu, E.W. Fuller, Sheilla Tseng, U. Von Sacken, and J.R. Dahn. *J. Electrochem. Soc.*, 142(8):2581–2590, 1995.

[10] P. Zhou, P. Papanek, C. Bindra, R. Lee, and J.E. Fischer. *J. Power Sources*, 68:296–300, 1997.

[11] P. Papanek, M. Radosavljevic, and J. E. Fischer. *Chemistry of Materials*, 8(7):1519–26, 1996.

[12] Yuan Gao and K. Myrtle, Meijie Zhang, J.N. Reimers, and J.R. Dahn. *Phys. Rev. B*, 54(23), 1996.

[13] Keijiro Sawai, Yasunobu Iwakoshi, and Tsutomu Ohzuku. *Solid State Ionics*, 69:273–283, 1994.

[14] Kazunori Ozawa. *Solid State Ionics*, 69:212–221, 1994.

[15] K.M. Abraham. *Electrochim. Acta*, 38:1233, 1993.

[16] E. Peled. *J. Electrochem. Soc*, 126:2047, 1979.

[17] Y. Matsuda. *Nihon Kagaku Kaishi*, 1, 1989.

[18] R. Yazami and P.Touzain. *J. Power Sources*, 9:365, 1983.

[19] S. Wang, Y. Matsumura, and T. Maeda. *Synthetic Metals*, 71:1759–60, 1995.

[20] Z.X. Shu et al. *J. Electrochem. Soc.*, 140:922, 1993.

[21] Rosamarie Fong, U. Von Sacken, and J.R. Dahn. *J. Electrochem. Soc.*, 137:2009–13, 1990.

[22] M. Sato et al. In *Proceedings of the Symposium on Primary and Secondary Lithium Batteries*, page 407.

[23] K. Tatsumi et al. In *Proceedings 183rd Meeting of the Electrochemical Society*, page 224, 1993.

[24] J.M. Tarascon et al. *J. Electochem. Soc.*, 138:2864, 1991.

[25] M. Mohri, N. Yanagisawa, Y. Tajima, H. Tanaka, T. Mitaie, S. Nakajima, Y. Yoshimoto, T. Suzuki, and H. Wada. *J. Power Sources*, 26:545, 1989.

[26] Tao Zheng and J.R. Dahn. *Synthetic Metals*, 73:1–7, 1995.

[27] Norio Takami, Asako Satoh, Michikazu Hara, and Takahisa Ohsaki. *J. Electrochem. Soc.*, 142:371–378, 1995.

[28] E. Peled. *J. Electrochem. Soc.*, 126:2047, 1981.

[29] V. V. Avdeev, V.A. Nalimova, and K.N. Semenenko. *High Pressure Research*, 6:11, 1990.

[30] G H Taylor and L F Cross. *J. Mat. Sci.*, 28(23):6503–10, 1993.

[31] H. Imoto, H. Azuma, A. Omaru, and Y. Nishi. In *58th Meeting Electrochem. Soc.*, Japan, Noda, April 5-7 1991. Ext. Abstr., 158.

[32] H Azuma, A. Omaru, and Y. Nishi. In *Fall Meeting Electrochem. Soc.*, Japan, Nagoya, Oct. 12-13 1991. Ext. Abstr. 132.

[33] A. Omaru, H. Azuma, M. Aoki, and Y. Nishi. In *Fall Meeting Electrochem. Soc.*, Japan, Nagoya, Oct. 12-13 1991. Ext. Abst. 132.

[34] H. Imoto, A. Omaru, H. Azuma, and Y. Nishi. In *Proc. Symp. On Lithium Batteries*, page 9. PV 93-24, 1992.

[35] A. Omaru, H. Azuma, M. Akoi, A. Kita, and Y. Nishi. In *Proc. Symp. On Lithium Batteries*, page 21. PV 93-24, 1992.

[36] S. Yata, H. Kinoshita, M. Komori, N. Ando, T. Kashiwamura, T. Harada, K.Tanaka, and T. Yamabe. *Synth. Met.*, 62:153, 1994.

[37] M. Hara, A. Satoh, N. Takami, and T. Ohsaki. *J. Phys. Chem.*, 99:16338, 1995.

[38] A. Mabuchi, K. Tokumitsu, H. Fujimoto, and T. Kasuh. *J. Electrochem. Soc.*, 142:1041, 1995.

[39] K. Tatsumi, T. Akai, T. Imamura, K. Zaghib, N. Iwashita, S. Higuchi, and Y. Sawada. *J. Electrochem. Soc.*, 143:1923, 1996.

[40] M. Ishikawa, N. Sonobe, H. Chuman, and T. Iwasaki. In *Ext. Abstr., 35th Battery Symp.*, page 47, Nagoya, Japan, 1994. Paper No. 2B09.

[41] T. Zheng, Q. Zhong, and J.R. Dahn. *J. Electrochem. Soc.*, 142(11):L211–L214, 1995.

[42] J.S. Xue and J.R. Dahn. *J. Electrochem. Soc.*, 142(11):3668–3677, 1995.

[43] Yinghu Liu, J.S. Xue, Tao Zheng, and J.R. Dahn. *Carbon*, 34(2):193–200, 1996.

[44] S. Wang, Y.Matsumura, and T. Maeda. *Sythetic Metals*, 71(1):1759–60, 1995.

[45] P.B. Hirsch. *Proc. Roy. Soc.*, A226:143, 1954.

[46] H. Imoto, M. Nagamine, and Y. Nishi. In *Proceedings 186rd Meeting of the Electrochemical Society*, Miami, FL., October 9-14 1994.

[47] H.P. Klug and L.E. Alexander. *X-Ray Diffraction Procedures.* Wiley & Sons Inc., 1954. Chap. 11.

[48] Norio Takami, Asako Satoh, Masayuki Oguchi, Hideyuki Sasaki, and Takahisa Ohsaki. *J. Power Sources*, 68:283–286, 1997.

[49] N. Sonobe, A. Hoshi, and T. Iwasaki. *Japanese Unexamined Patent Application #07-124302*, April 25, 1996.

[50] W. Xing, J.S. Xue, and J.R. Dahn. *J. Electrochem. Soc.*, 143(10):3046–3052, 1996.

[51] Neil W. Ashcroft and N. David Mermin. *Solid State Physics.* Harcourt Brace College Publishers, New York, 1976.

[52] Charles Kittel. *Introduction to Solid State Physics.* John Wiley & Sons, New York, 1986.

[53] Hang Shi. *Disordered Carbons and Battery Applications.* PhD thesis, Simon Fraser University, 1993.

[54] B.E. Warren. *X-Ray Diffraction.* Addison-Wesley, New York, 1969.

[55] L. Rayleigh. *Proc. Roy. Soc.*, A-84:25, 1911.

[56] A. Guinier and G. Fournet. *Small-Angle Scattering of X-Rays.* John Wiley & Sons, New York, 1955.

[57] G. Porod. *Killoid Zeitschrift*, 124:83, 1951.

[58] P. Debye, H.R. Anderson, and H. Brumberger. *J. Appl. Phys.*, 28:659, 1957.

[59] A. Gibaud, J.S. Xue, and J.R. Dahn. *Carbon*, 34(4):499–503, 1996.

[60] Tao Zheng, W. Xing, and J.R. Dahn. *Carbon*, 34(12):1501–1507, 1996.

[61] S. Brunaur, P.H. Emmet, and E. Teller. *J. Amer. Chem. Soc.*, 60:309, 1938.

[62] A.L. McCellan and H.F. Harnsberger. *J. Coll. Interface Sci.*, 23:577, 1967.

[63] I. Langmuir. *J. Amer. Chem. Soc.*, 38:2221, 1916.

[64] S.J. Gregg. *Adsorption, Surface Area and Porosity.* Academic Press, 1967.

[65] Michael Plischke and Birger Bergersen. *Equilibrium Statistical Physics.* World Scientific, 1994.

[66] M. M. Dubinin. *Russ. J. Phy. Chem.*, page 697, 1965. (English Trans.).

[67] H.F. Stoeckli and J.Ph. Houriet. *Carbon*, 14:253–256, 1976.

[68] Ueli Huber. *J. Colloid Interface Sci.*, 67(2):195–203, 1978.

[69] M. Polanyi. *Verh. dtsh. physik. Ges.*, 16:1012, 1914.

[70] M. Smizek and S. Cerny. *Active Carbon.* Elsevier, Amsterdam, 1970.

[71] M. Dubinin and V. Astakhov. *Adv. Chem. Ser.*, 102:69, 1971.

[72] E.P. Barrett, L.S. Joyner, and P.P. Halenda. *J. Am. Chem. Soc.*, 73:373–80, 1951.

[73] J. Kelvin (published under the name of Sir William Thomson). *Phil. Mag.*, 42:448–52, 1871.

[74] G. Halsey. *J. Chem. Phys.*, 16:931–37, 1948.

[75] Micromeritics Instrument Corporation. *ASAP 2010 Instructions Manuel*, 1996.

[76] Weibing Xing, J.S. Xue, Tao Zheng, A. Gibaud, and J.R. Dahn. *J. Electrochem. Soc.*, 143(11):3482–3491, 1996.

[77] Tao Zheng, W.R. McKinnon, and J.R. Dahn. *J. Electrochem. Soc.*, 143(7):2137–2145, 1996.

[78] W. T. Thomson. *Phil. Mag.*, 42:448, 1871.

[79] E. O. Kraemer in H.S. Taylor's. *A Treatise on Physical Chemistry.* Macmillan, New York, 1931.

[80] J. W. McBain. *J. Amer. Chem. Soc.*, 57:669, 1935.

[81] K. S. Rao. *J. phys. Chem. Soc.*, 45:506, 517, 1941.

[82] S. M. Katz. *J. phys. Chem. Soc.*, 53:1166, 1949.

[83] N. Liu, H. Touhara, F. Okino, S. Kawasaki, and Y. Nakacho. *J. Elec. Chem. Soc.*, 143:2267–2272, 1996.

[84] G B M Vaughan, M Barral, T Pagnier, and Y Chabre. *Synthetic Metals*, 77(1):7–12, 1996.

IMAGE EVALUATION TEST TARGET (QA-3)

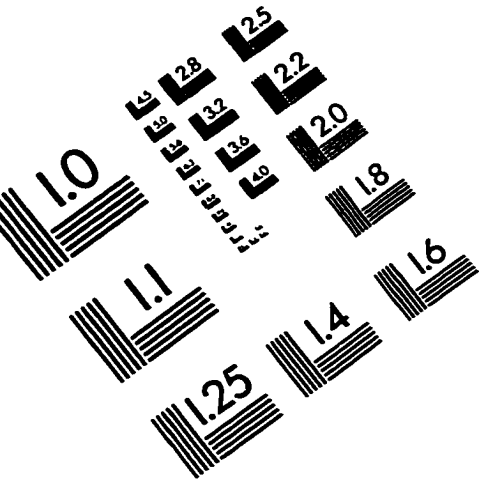

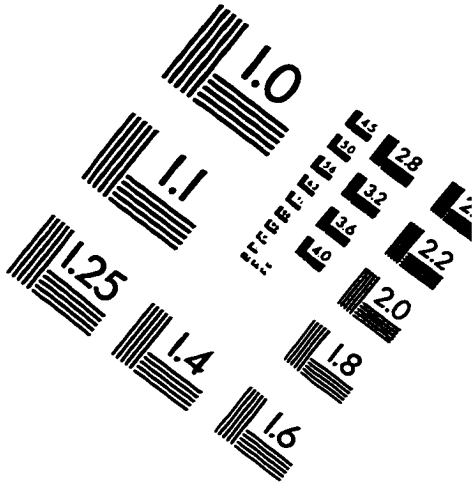

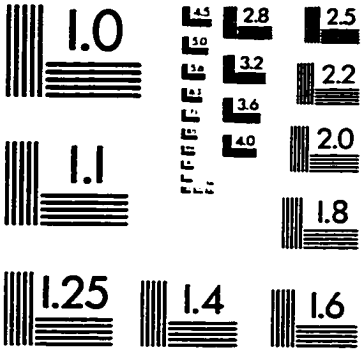

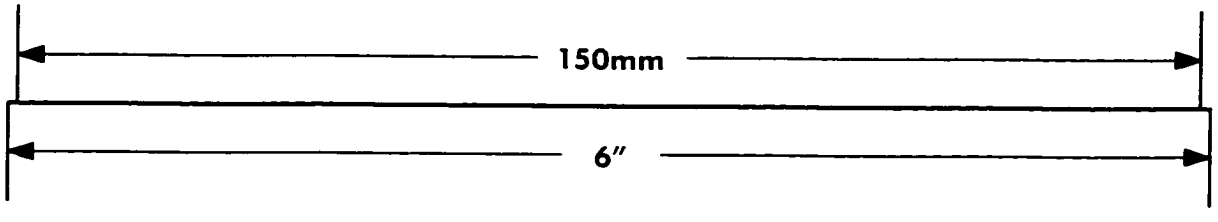

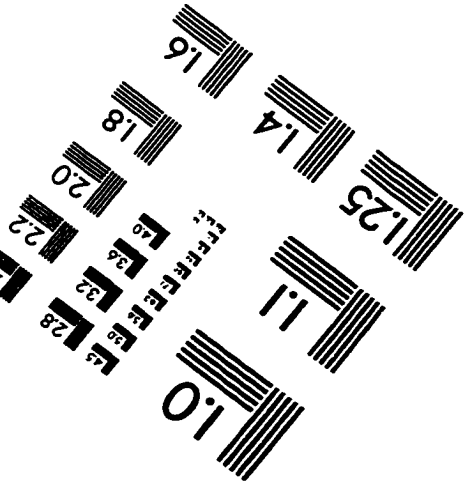

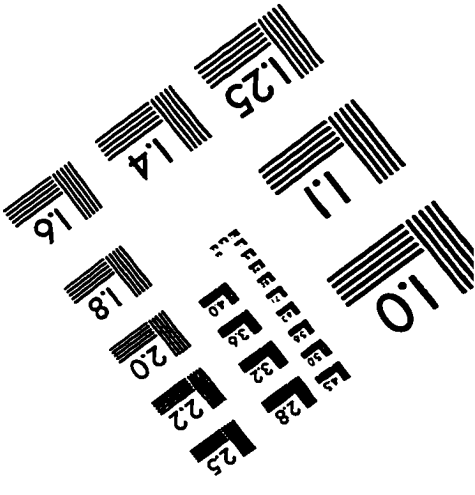

APPLIED IMAGE, Inc
1653 East Main Street
Rochester, NY 14609 USA
Phone: 716/482-0300
Fax: 716/288-5989

© 1993, Applied Image, Inc., All Rights Reserved